

AN ABSTRACT OF THE DISSERTATION OF

Michael Jason Paul for the degree of Doctor of Philosophy in Physics presented on September 25, 2014.

Title: Nonlinear Terahertz Spectroscopy of Carbon Nanomaterials and Semiconductor Nanostructures

Abstract approved: _____

Yun-Shik Lee

This thesis will cover my work relating to the developing field of terahertz (THz) science and technology. It will present experimental and theoretical studies investigating the optical and electrical properties of various material systems using novel THz imaging and spectroscopy techniques. Due to its low photon energy, THz imaging and spectroscopy are useful tools for non-contact, non-destructive probing of materials. Broadband, single-cycle THz pulses are prepared using modern THz generation technology. Using the THz detection techniques of THz raster imaging and THz time-domain spectroscopy (THz-TDS), the local carrier dynamics of nanomaterials such as graphene and carbon nanotubes were determined. THz measurements on single-layer graphene grown with different recipes and on various substrates exhibit sub-millimeter spatial inhomogeneity of sheet conductivity. THz transmission data reveals that a thin plastic, polymethyl methacrylate (PMMA),

layer in contact with single-layer graphene induces a small yet noticeable reduction in conductivity. Ulterior THz measurements performed on vertically-aligned multi-walled carbon nanotubes (V-MWCNT) employ time-resolved THz transmission ellipsometry. The angle- and polarization-resolved transmission measurements reveal anisotropic characteristics of the THz electrodynamics in V-MWCNT. The anisotropy is, however, unexpectedly weak: the ratio of the tube-axis conductivity to the transverse conductivity, $\sigma_z/\sigma_{xy} \cong 2.3$, is nearly constant over the broad spectral range of 0.4-1.6 THz. The relatively weak anisotropy and the strong transverse electrical conduction indicate that THz fields readily induce electron transport between adjacent shells within the multi-walled carbon nanotubes.

In-depth coverage of the development of a high-field THz generation system based on a lithium niobate prism will be presented. The evolution of techniques in the realm of high power THz generation is ongoing. The resolved issues throughout implementation include: magnesium doping, phase matching, and wave front distortion. The high power, broadband THz emitter (maximum THz field, $E_{\max} > 1$ MV/cm) allows for nonlinear THz spectroscopy of various material systems including single-layer graphene and high-resistivity, bulk GaAs. THz-induced transparency is observed in two types of single-layer graphene samples: (i) suspended graphene-PMMA layer and (ii) graphene embedded in dielectrics. THz-induced transparency is shown to be significantly higher in suspended graphene than in graphene on a Si substrate. The experimental observation leads to a universal nonlinear THz property of graphene that the sheet conductivity undergoes two-fold reduction when THz fields reach 0.8 MV/cm. We confirm the generality of

this result by measuring different graphene samples on different substrates. Time-resolved THz transmission measurements show that the THz-induced transparency in graphene is dynamic; the transient conductivity gradually decreases throughout the pulse duration. The large THz fields induce sub-picosecond electron thermalization and subsequent carrier-carrier scattering, transiently modulating the electrical and optical properties, in effect reducing the electrical conductivity of graphene by an order of magnitude. Nonlinear THz spectroscopy methods are also applied to the investigation of a nano-antenna patterned, high-resistivity, intrinsic GaAs wafer. The antenna near-field reaches 20 MV/cm due to a huge field enhancement in the plasmonic nanostructure. Thus, the nonlinear THz interactions take place in the confined nanometer-scale region adjacent to the antenna. As a result of the huge THz fields, nano-antenna patterned GaAs demonstrates remarkably strong nonlinear THz effects. The fields are strong enough to generate high density free carriers ($N_e > 10^{17} \text{ cm}^{-3}$) via high-energy interband excitations associated with a series of impact ionizations ($n_I \approx 33\text{-}37$); thus inducing large absorption of THz radiation ($> 35\%$).

©Copyright by Michael Jason Paul
September 25, 2014
All Rights Reserved

Nonlinear Terahertz Spectroscopy of Carbon Nanomaterials and
Semiconductor Nanostructures

by

Michael Jason Paul

A DISSERTATION

submitted to

Oregon State University

in partial fulfillment of
the requirements for the
degree of

Doctor of Philosophy

Presented September 25, 2014
Commencement June 2015

Doctor of Philosophy dissertation of Michael Jason Paul presented on
September 25, 2014.

APPROVED:

Major Professor, representing Physics

Chair of the Department of Physics

Dean of the Graduate School

I understand that my dissertation will become part of the permanent collection of Oregon State University libraries. My signature below authorizes release of my dissertation to any reader upon request.

Michael Jason Paul, Author

ACKNOWLEDGEMENTS

Written and Dedicated to the untouchable past, persistently present, unconditional, and never ending love and support of my mother, Sylvia Waack, and my father, Mark Paul.

TABLE OF CONTENTS

	<u>Page</u>
1 Overview	1
2 Theory	5
2.1 Wave Equation	5
2.2 Harmonic Oscillator	13
2.3 Second-Order Nonlinear Wave Equation	18
2.4 Velocity Matching	34
2.5 Pockels Effect	43
2.6 The Drude Model	47
2.7 Fresnel Equations	51
2.8 Fresnel Equations for Anisotropic Materials	57
2.9 Thin Film Fresnel Formula	68
2.10 From Fresnel to Fraunhofer Optics	77
2.11 Paraxial Approximation	79
2.12 Ultrafast Pulse Propagation	83
2.13 Determining Beam Shape	92
2.14 Picosecond Pulse Detection with a Millisecond THz Detector	96
2.15 THz Field Strength	101
3 High Power THz Generation via Lithium Niobate	106
3.1 Overview	106
3.2 Velocity Matching	107
3.3 Diffraction Grating	110
3.4 Single Lens	115
3.5 Wave Front Distortion	119
3.6 Two Lens System	120
3.7 THz Output	124
4 Terahertz Imaging of Single-Layer Graphene Embedded in Dielectrics	127
4.1 Introduction	127

TABLE OF CONTENTS (Continued)

	<u>Page</u>
4.2 Experiment	129
4.3 Power Transmission: Graphene Local Sheet Conductivity	131
4.4 PMMA-Graphene Interface: Power Transmission	133
4.5 PMMA-Graphene Interface: THz-TDS	135
4.6 Conclusion	137
5 High-Field Terahertz Response of Single-Layer Graphene	138
5.1 Introduction	138
5.2 Experiment	141
5.3 Intrinsic Local Carrier Dynamics	145
5.4 THz-Induced Transparency and Normalized Conductivity	146
5.5 Transient Non-Equilibrium Electron Distributions	151
5.6 Conclusion	152
6 THz Transmission Ellipsometry of Vertically-Aligned CNTs	155
6.1 Introduction	155
6.2 Experiment	156
6.3 THz Power Transmission Ellipsometry	159
6.4 Time-Resolved THz Transmission Ellipsometry	160
6.5 V-MWCNT Analysis	162
6.6 Results	164
6.7 Conclusion	167
7 Large THz Absorption in Intrinsic GaAs	169
7.1 Introduction	169
7.2 Experiment	170
7.3 Field-Dependent THz Transmission: Bare GaAs	174
7.4 Field-Dependent THz Transmission: Antenna-on-GaAs	176
7.5 Analysis	177
7.6 Conclusion	179

TABLE OF CONTENTS (Continued)

	<u>Page</u>
8 Summary	180
Bibliography	183

LIST OF FIGURES

<u>Figure</u>		<u>Page</u>
2.1	Linear harmonic oscillator	14
2.2	Dielectric dispersion near resonance	17
2.3	Second-order perturbative potential energy	20
2.4	Second-order nonlinear processing	28
2.5	Optically rectified material polarization	31
2.6	Generated THz power vs. incidence angle in ZnTe	33
2.7	Second-order coherence length	38
2.8	THz generation over propagation length	39
2.9	Index of refraction of ZnTe	41
2.10	Index of refraction of LN	42
2.11	THz time-domain spectroscopy and electro-optic sampling	45
2.12	Electromagnetic boundary conditions for isotropic media	52
2.13	Reflectance and transmittance across a boundary	55
2.14	Uniaxial index of refraction visualization	58
2.15	Anisotropic sample structure	60
2.16	Electromagnetic boundary conditions for anisotropic media	62
2.17	Transmission ray trace through a thin film on a substrate	69
2.18	Transmission ray trace through a suspended thin film	71
2.19	Quadratic chirped optical pulse	84
2.20	THz power meter responsivity, pulsed	97
2.21	THz power meter responsivity, continuous wave	100
2.22	Spectral response of pyroelectric THz detector	102

LIST OF FIGURES (Continued)

<u>Figure</u>	<u>Page</u>
3.1 Optical and THz index of refraction of LN	107
3.2 Velocity mismatch between optical and THz pulse fronts	108
3.3 Velocity match utilizing Cherenkov radiation	108
3.4 Pulse front tilt: Air vs. LN	110
3.5 Diffraction grating: white light	111
3.6 Diffraction grating: tilting the pulse front	113
3.7 Diffraction grating: on the LN input surface	114
3.8 Single lens system	115
3.9 Single lens: graph of optimized parameters for THz generation	117
3.10 Two lens system	121
3.11 Two lens: graph of optimized parameters for THz generation	122
3.12 THz output parabolic mirror arrangement	125
4.1 Graphene sample structure and experimental set-up	131
4.2 THz transmission images of graphene	133
4.3 Sheet conductivity images of graphene	135
4.4 Transmitted THz waveforms through graphene	136
5.1 Theoretical odd-harmonic generation in graphene	140
5.2 Graphene sample structure and experimental set-up	143
5.3 Graphene sample structure and intrinsic sheet conductivity	145
5.4 THz-induced transparency in graphene	147
5.5 Normalized conductivity for various locations in graphene	149
5.6 Dynamic THz-induced transparency through graphene	152

LIST OF FIGURES (Continued)

<u>Figure</u>		<u>Page</u>
6.1	CNT sample structure and experimental set-up	157
6.2	Transmission ellipsometry: THz power	159
6.3	Transmission ellipsometry: THz waveform, p-polarization	161
6.4	Transmission ellipsometry: THz waveform, s-polarization	162
6.5	CNT uniaxial dielectric function	166
7.1	GaAs sample structure and experimental set-up	172
7.2	THz-induced absorption: Bare GaAs	174
7.3	THz-induced absorption: nano-antenna-on-GaAs	176

LIST OF TABLES

<u>Table</u>		<u>Page</u>
2.1	The contracted susceptibility notation	28
2.2	The contracted susceptibility values for ZnTe and LN	29
2.3	Optically rectified field polarization in ZnTe	34
2.4	Second-order velocity matching conditions	36
2.5	Drude model for susceptibility, permittivity, and conductivity . . .	48
2.6	Power transmission through optical obstructions	95
6.1	CNT uniaxial dielectric function parameters	164

Nonlinear Terahertz Spectroscopy of Carbon Nanomaterials and Semiconductor Nanostructures

1 Overview

Terahertz (THz) radiation lies in the electromagnetic (EM) spectrum between the microwave (GHz) and infrared (IR) regimes, both of which are very well explored through electronics and laser science, respectively. The THz regime is commonly referred to as the “THz Gap” that bridges electronics and laser science. The THz gap falls partially in both electronics and optics due to its capacity to satisfy both technological capabilities. As such, the THz spectral region is an open-road with many paths to travel. This leads to a primary motivation: exploration of the THz regime. The utilization of THz frequencies in modern computing would be a technological quantum leap. Transitioning from GHz electronics to THz signal processing would be an extraordinary development of high-speed processing and communication. Smaller and faster computer circuits comprise higher frequencies (THz) and stronger electric fields (> 100 kV/cm) within the integrated circuits. Due to this key factor, it becomes increasingly important to characterize the electronic and optical THz properties of semiconductors and nanostructures in the high-field regime.

To further explain the matter of why the three regimes (GHz, THz, and IR) are independent is a matter of atomic, molecular, and optical physics; the GHz regime interacts with molecular rotational energies, the THz regime interacts with

molecular vibrational energies, and the IR regime interacts on the energy level of atomic transitions. One major set-back to the exploration and utilization of THz radiation is that vibrational modes provide highly absorptive optical properties to commonplace dielectrics. Due to lattice vibrations in dielectrics, development of THz sources and detectors are limited, which in turn limits materials, time, money, and, ultimately, the accessibility of exploring THz material properties. On the other hand, the THz regime has a long period of oscillation in comparison to the electron response time of a typical metal. Simply put, THz waves are highly conducted in metals and, thus, satisfy the Drude model.

We utilize Broadband, single-cycle THz pulses in THz raster imaging and THz time-domain spectroscopy (THz-TDS) on single-layer graphene and vertically-aligned multi-walled carbon nanotubes (V-MWCNTs) to determine THz material properties. Due to strong THz absorption ($> 15\%$) and a flat spectral response in graphene, the Drude model can be applied. This allows THz transmission to correspond to the local sheet conductivity of graphene on a sub-millimeter scale. We measured the THz properties of single-layer graphene of different growth recipes embedded in dielectrics. Our THz data shows that a thin plastic, polymethyl methacrylate (PMMA), layer in contact with graphene induces a small yet noticeable reduction in conductivity. Time-resolved THz transmission ellipsometry was performed on V-MWCNTs to reveal anisotropic THz electrodynamics. The THz measurements show an unexpectedly weak anisotropy: the ratio of the tube-axis conductivity to the transverse conductivity, $\sigma_z/\sigma_{xy} \cong 2.3$, is nearly constant over the broad THz spectral range. The transverse electrical conduction indicates

that THz fields induce electron transport through shallow potential wells between adjacent shells within the multi-walled CNT structure.

Generally speaking, the drawbacks of lattice vibrations in dielectrics and the ideals of non-dispersive substrates and Drude metals quickly break down in the presence of strong THz electric fields. Typical optical responses are thwarted once the THz electric field strength is remarkably high. Enter the nonlinear regime. Nonlinear interactions play a strong chord on the EM spectrum, allowing material properties to evolve into a breadth of spectral responses. Strong fields can induce transparency or absorption through a variety of band structure effects such as intervalley scattering, coherent ballistic transport, effective mass anisotropy, or impact ionization. However, nonlinear effects in some materials have yet to be defined. Our objective is to utilize strong THz fields to optically modulate the electronic properties of various materials in the hopes of procuring new theoretical models.

The development of a high-field THz generation system based on a lithium niobate (LN) prism will be covered. In the process of optimizing THz generation through power conversion efficiency, optical input alignment is extremely sensitive. An in-depth coverage on alignment techniques, the evolution of the development process, and resolved alignment issues will be presented. Once developed, we used the high power, broadband THz emitter ($E_{\text{max}} > 1 \text{ MV/cm}$) for nonlinear THz spectroscopy. THz-induced transparency is observed in two types of CVD grown single-layer graphene. Experimental observations lead to a universal nonlinear THz property of graphene that the sheet conductivity undergoes two-fold reduc-

tion when THz fields reach 0.8 MV/cm. This observation is witnessed at various locations across two large-area graphene samples. Through THz-TDS, the THz-induced transparency is shown to be dynamic; the transient conductivity gradually decreasing throughout the pulse duration (90% reduction in conductivity at trailing peak of a THz pulse with field amplitude of 1.3 MV/cm). THz fields induce sub-picosecond electron thermalization through a thermal redistribution of occupied states, subsequent carrier-carrier scattering; dynamically inducing a transient, quasi-equilibrium modulation of the optical and electronic properties of single-layer graphene.

THz nonlinear measurements are further pursued in high-resistivity, intrinsic GaAs wafers. High-resistivity GaAs is a fairly dispersionless material that undergoes little nonlinear effects under strong THz radiation. In order to extract nonlinearities, the field strength is amplified by patterning bulk GaAs with a plasmonic nano-antenna array. The antenna near-field reaches 20 MV/cm due to the huge field enhancement in the plasmonic nanostructure. Due to the emitted dipole radiation from the nanostructures, the nonlinear THz interactions take place in a confined nanometer-scale region adjacent to the antennas. Outside the confined region, the bulk GaAs behaves linearly as the THz field rapidly diminishes. Large THz-induced absorption occurs ($> 35\%$) due to the generation of high density free carriers ($N_e > 10^{17} \text{ cm}^{-3}$) in the semiconductor band structure via interband excitations associated with a series of impact ionizations ($n_I \approx 33\text{-}37$). In the presence of huge THz fields, an extreme nonlinear response is induced as the high-resistivity bulk GaAs wafer evolves into a strong absorber of THz radiation.

2 Theory

2.1 Wave Equation

To begin to describe electromagnetic (EM) wave propagation in an arbitrary medium, we must introduce the macroscopic Maxwell's equations (read more in Refs: [1–5]). These equations together with the Lorentz force law create the fundamental theoretical basis of classical electrodynamics and hold the functional form

$$\nabla \cdot \mathbf{D} = \rho_f \tag{2.1}$$

$$\nabla \cdot \mathbf{B} = 0 \tag{2.2}$$

$$\nabla \times \mathbf{E} = -\frac{\partial \mathbf{B}}{\partial t} \tag{2.3}$$

$$\nabla \times \mathbf{H} = \mathbf{J}_f + \frac{\partial \mathbf{D}}{\partial t} \tag{2.4}$$

$$\mathbf{F} = q(\mathbf{E} + v \times \mathbf{B}) \tag{2.5}$$

where q and v represent charge and velocity and ρ_f and \mathbf{J}_f represent free charge density and free current density, respectively. The displacement field and auxiliary field, \mathbf{D} and \mathbf{H} , represent the macroscopic behavior of electromagnetic fields in matter. They are related to the fundamental fields, \mathbf{E} and \mathbf{B} by fundamental

constants: ϵ_0 and μ_0 , the permittivity and permeability of free space.

$$\mathbf{D} = \epsilon_0 \mathbf{E} + \mathbf{P} = \epsilon \mathbf{E} \quad (2.6)$$

$$\mathbf{H} = \frac{1}{\mu_0} \mathbf{B} - \mathbf{M} = \frac{1}{\mu} \mathbf{B} \quad (2.7)$$

ϵ and μ are infinite-order tensors marking the electric permittivity and magnetic permeability of matter and ϵ_0 and μ_0 are the permittivity and permeability of free space. \mathbf{P} and \mathbf{M} are the electric polarization and magnetization. Typically, matter has a weak magnetic response. To retain generality the variable, μ , will be preserved which entails that our arbitrary medium has a magnetic response.

By taking the curl of the macroscopic Maxwell's equations, Eq. 2.3 and Eq. 2.4, then substituting the fundamental fields equations, Eq. 2.6 and Eq. 2.7, we obtain the generalized electromagnetic wave equations:

$$\nabla \times (\nabla \times \mathbf{E}) + \epsilon_0 \mu_0 \frac{\partial^2 \mathbf{E}}{\partial t^2} = -\mu_0 \frac{\partial}{\partial t} \left(\mathbf{J}_f + \frac{\partial \mathbf{P}}{\partial t} + \nabla \times \mathbf{M} \right) \quad (2.8)$$

$$\nabla \times (\nabla \times \mathbf{H}) + \epsilon_0 \mu_0 \frac{\partial^2 \mathbf{H}}{\partial t^2} = \nabla \times \mathbf{J}_f + \nabla \times \frac{\partial \mathbf{P}}{\partial t} - \epsilon_0 \mu_0 \frac{\partial^2 \mathbf{M}}{\partial t^2} \quad (2.9)$$

Together, these wave equations represent the intertwined fields that compose an electromagnetic wave. If we incorporate the Curl of the Curl identity,

$$\nabla \times (\nabla \times \mathbf{A}) = \nabla (\nabla \cdot \mathbf{A}) - \nabla^2 \mathbf{A} \quad (2.10)$$

along with Maxwell's equations, we arrive at wave equations representative of

charge and current:

$$\nabla^2 \mathbf{E} - \epsilon_0 \mu_0 \frac{\partial^2 \mathbf{E}}{\partial t^2} = \frac{1}{\mu_0} \nabla \rho_f + \mu_0 \frac{\partial}{\partial t} \left(\mathbf{J}_f + \frac{\partial \mathbf{P}}{\partial t} + \nabla \times \mathbf{M} \right) \quad (2.11)$$

$$\nabla^2 \mathbf{H} - \epsilon_0 \mu_0 \frac{\partial^2 \mathbf{H}}{\partial t^2} = -\nabla \times \mathbf{J}_f - \nabla \times \frac{\partial \mathbf{P}}{\partial t} + \epsilon_0 \mu_0 \frac{\partial^2 \mathbf{M}}{\partial t^2} \quad (2.12)$$

We can begin simplifying by neglecting charge fluctuations, $\nabla \rho_f = 0$, and assuming a linear relationship between \mathbf{J}_f and \mathbf{E} known as Ohm's Law,

$$\mathbf{J}_f = \sigma \mathbf{E} \quad (2.13)$$

where σ is the electric conductivity of the medium. Combining these approximations, we can describe electromagnetic wave propagation in a homogeneous medium,

$$\nabla^2 \mathbf{E} = \sigma \mu_0 \frac{\partial \mathbf{E}}{\partial t} + \epsilon_0 \mu_0 \frac{\partial^2 \mathbf{E}}{\partial t^2} + \mu_0 \frac{\partial^2 \mathbf{P}}{\partial t^2} + \mu_0 \nabla \times \frac{\partial \mathbf{M}}{\partial t} \quad (2.14)$$

$$\nabla^2 \mathbf{H} = \sigma \mu_0 \frac{\partial \mathbf{H}}{\partial t} + \epsilon_0 \mu_0 \frac{\partial^2 \mathbf{H}}{\partial t^2} - \nabla \times \frac{\partial \mathbf{P}}{\partial t} + \epsilon_0 \mu_0 \frac{\partial^2 \mathbf{M}}{\partial t^2} \quad (2.15)$$

At this moment, the non-magnetic approximation ($\mu = \mu_0$) is useful to describe materials studied in this thesis. Typically, materials are considered non-magnetic when $\frac{\epsilon}{\epsilon_0} \gg \frac{\mu}{\mu_0}$, or, when the electric interaction is much stronger than the magnetic interaction and, thus, dominates the material response. This leads to drastic simplification ($\mathbf{M} = 0$ and $\nabla \times \mathbf{M} = 0$) and allows us to represent the intertwined

fields in the generalized, non-magnetic wave equations,

$$\nabla^2 \mathbf{E} = \sigma \mu_0 \frac{\partial \mathbf{E}}{\partial t} + \epsilon_0 \mu_0 \frac{\partial^2 \mathbf{E}}{\partial t^2} + \mu_0 \frac{\partial^2 \mathbf{P}}{\partial t^2} \quad (2.16)$$

$$\nabla^2 \mathbf{H} = \sigma \mu_0 \frac{\partial \mathbf{H}}{\partial t} + \epsilon_0 \mu_0 \frac{\partial^2 \mathbf{H}}{\partial t^2} - \nabla \times \frac{\partial \mathbf{P}}{\partial t} \quad (2.17)$$

The auxillary field form (Eq. 2.17) is beautiful, however the electric field form is of our particular interest and representative of the work done in this thesis. As such, Eq. 2.16 becomes our grand wave equation. In the sections to come, the grand wave equation will be used in several ways.

It is important to address the unique features of σ and \mathbf{P} . The dielectric response can be generally described as nonlinear. Material polarization depends on the nonlinear dielectric response of a material to an electromagnetic wave. The nonlinear process can be expressed as a Taylor expansion,

$$\mathbf{P} = \epsilon_0 (\chi_e^{(1)} \otimes \mathbf{E} + \chi_e^{(2)} \otimes \mathbf{E} \otimes \mathbf{E} + \chi_e^{(3)} \otimes \mathbf{E} \otimes \mathbf{E} \otimes \mathbf{E} + \dots) \quad (2.18)$$

Nonlinear optics will be discussed in Section 2.3. In electromagnetism, the electric susceptibility tensor, χ_e , describes the polarization response to an applied electric field. In the presence of an electromagnetic wave, the tensor is frequency dependent and nonlinear with infinite order. Higher order terms of χ_e are contracted with numerous electric fields to generate higher orders of nonlinear material polarization. In the special case of weak nonlinear material response ($\chi_e^{(1)} \gg \chi_e^{(2)} \gg \chi_e^{(3)} \gg \dots$) or weak electric field strength ($E^n \ll \chi_e^{(n)}$), the higher

order susceptibility tensor terms vanish and the nonlinear material polarization collapses into a linear material polarization:

$$\mathbf{P} = \epsilon_0 \chi_e^{(1)} \mathbf{E} = (\epsilon - \epsilon_0) \mathbf{E} \quad (2.19)$$

Now, χ_e simplifies ($\chi_e = \frac{\epsilon}{\epsilon_0} - 1$). It is important to note that in a highly nonlinear dielectric or highly responsive medium such as a metal, the Taylor expansion breaks down and more complex theoretical models must be explored. For practical applications, however, the nonlinear susceptibility tensor has accelerated the development of the optics community.

In many dielectric materials such as gallium arsenide (see Ch. 7), the higher order terms are small enough to ignore unless the \mathbf{E} field is strong enough. Also, in many materials, higher order tensor elements in $\chi_e^{(n)}$ can be simplified based on the symmetry of the material. The complexities of nonlinear material response are of exorbitant importance in modern optics and will be a broad discussion in Section 2.3. For now, in all matter of linearity, we can obtain the generalized linear wave equation for all materials, conductors and dielectrics alike, by incorporating the linear \mathbf{P} field from Eq. 2.19 into the grand wave equation, Eq. 2.16:

$$\nabla^2 \mathbf{E} = \sigma \mu_0 \frac{\partial \mathbf{E}}{\partial t} + \epsilon \mu_0 \frac{\partial^2 \mathbf{E}}{\partial t^2} \quad (2.20)$$

Lastly, in the special scenario where the material under investigation is a dielectric and not a metal ($\sigma \ll \omega \epsilon$), we can simplify the above into the wave equation

we all know and love, and hold dearly to our hearts,

$$\nabla^2 \mathbf{E} = \epsilon \mu_0 \frac{\partial^2 \mathbf{E}}{\partial t^2} = \frac{n^2}{c^2} \frac{\partial^2 \mathbf{E}}{\partial t^2} \quad (2.21)$$

where $n = \sqrt{\frac{\epsilon}{\epsilon_0}}$ and $c = \sqrt{\frac{1}{\epsilon_0 \mu_0}}$, are the index of refraction and the speed of light in free space, respectively. \mathbf{H} can be substituted for \mathbf{E} to symmetrically describe the dielectric coupling of the two fields into an electromagnetic wave. The general solution to the dielectric wave equation,

$$\mathbf{E}(\mathbf{r}, t) = \mathbf{E}_0 e^{i(\mathbf{k} \cdot \mathbf{r} - \omega t)} \quad (2.22)$$

$$\mathbf{H}(\mathbf{r}, t) = \mathbf{H}_0 e^{i(\mathbf{k} \cdot \mathbf{r} - \omega t)} \quad (2.23)$$

describes the propagation of linearly polarized, monochromatic plane waves with wave vector, \mathbf{k} , and angular frequency, ω . The dielectric wave equation solutions are also valid to the wave equation for a conductor, Eq. 2.20. The wave vector ($\mathbf{k} = \frac{2\pi n}{\lambda_0}$, where λ_0 describes the free space wavelength) and angular frequency ($\omega = 2\pi f$, where f is the field oscillation frequency in all space) lead to very interesting optical phenomena including boundary conditions (Section 2.7) and Gaussian wave propagation (Section 2.12).

If we recall zero net free charge and substitute the wave equation solutions (Eqs. 2.22 and 2.23) into Maxwell's equations (Eqs. 2.1, 2.2, and 2.3) we find that

the fields \mathbf{E} and \mathbf{H} are transverse and that \mathbf{E} , \mathbf{H} , and \mathbf{k} are orthogonal:

$$\mathbf{k} \cdot \mathbf{E} = \mathbf{k} \cdot \mathbf{H} = 0 \quad (2.24)$$

$$\mathbf{k} \times \mathbf{E} = \omega\mu_0\mathbf{H} \quad (2.25)$$

If we insert the wave equation solutions (Eqs. 2.22 and 2.23) into the dielectric wave equation (Eq. 2.21) we arrive at Helmholtz equation,

$$(\nabla^2 + k^2) \begin{Bmatrix} \mathbf{E}(\mathbf{r}) \\ \mathbf{H}(\mathbf{r}) \end{Bmatrix} = 0 \quad (2.26)$$

where k represents the dielectric dispersion relation,

$$k^2 = \epsilon\mu_0\omega^2 \quad (2.27)$$

The dispersion relation describes how a material spectrally disperses electromagnetic radiation. Section 2.2 explains this physical phenomena in more detail. If we insert the wave equation solutions (Eqs. 2.22 and 2.23) into the conductor wave equation (Eq. 2.20) we obtain the conductive dispersion relation,

$$k^2 \approx i\sigma\mu_0\omega \quad (2.28)$$

The dispersion relation for a conductor, as well as the conductor wave equation, is specific to a highly conductive material, such that $\sigma \gg \omega\epsilon$. In this particular

scenario, k^2 is purely imaginary which makes the real and imaginary components of \mathbf{k} equivalent,

$$\text{Re } |\mathbf{k}| = \text{Im } |\mathbf{k}| = \sqrt{\frac{\sigma\mu_0\omega}{2}} \quad (2.29)$$

When the dispersion relation for a conductor is substituted into the wave equation solutions (Eqs. 2.22 and 2.23), the imaginary component of \mathbf{k} gives rise to an exponential decay term

$$\mathbf{E}(z) \propto e^{-z/\delta} \quad (2.30)$$

The decay length,

$$\delta = \sqrt{\frac{2}{\omega\mu_0\sigma}} \quad (2.31)$$

is also known as the skin depth, penetration depth, or attenuation length. It describes how deeply electromagnetic radiation penetrates a material (in this specific case, a highly conducting metal) before the field amplitude decays to $\frac{1}{e}$, or $\approx 36.8\%$, times the incident field strength. In some cases, it is appropriate to discuss the absorption coefficient which can be deduced by the imaginary component of the complex index of refraction ($\tilde{n} = n + i\kappa$),

$$\alpha(\omega) = 2\kappa\frac{\omega}{c} = \frac{2}{\delta} = \sqrt{2\sigma\mu_0\omega} \quad (2.32)$$

Consequentially, in a typical bulk conductor, the transmitted \mathbf{E} field decays rapidly in an over-damped manner ($\sigma \gg \omega\epsilon \Rightarrow \delta \ll \frac{\lambda_0}{n}$) while the majority of the \mathbf{E} field is reflected due to the large index mismatch ($\sigma \gg \omega\epsilon \Rightarrow n \gg 1$). This will be covered in much more detail when describing the Fresnel equations for thin

conductors in Section 2.9.

The energy flux of an electromagnetic wave is the time-averaged Poynting vector,

$$\mathbf{S} = \mathbf{E} \times \mathbf{H} \quad (2.33)$$

The time-averaged energy flux is called the radiation intensity, or, irradiance,

$$I = \langle \mathbf{S} \rangle \quad (2.34)$$

For a monochromatic, plane wave, the irradiance simplifies,

$$I = \frac{1}{2}cn\epsilon_0|E_0|^2 = \frac{1}{2}v\epsilon|E_0|^2 \quad (2.35)$$

where $v = \frac{c}{n}$ is the speed of light in the respective medium. This formula is useful for calculating the electric field amplitude, E_0 , through intensity measurements, experimentally via a power meter. This type of calculation is described fully in Section 2.15.

2.2 Harmonic Oscillator

Dispersion and absorption are fundamental physical phenomena that characterize how a medium responds to electromagnetic radiation. Under non-magnetic pretenses, electromagnetic material properties are dominated by electric dipoles. In order to address the interaction between charged particles and external \mathbf{E} fields

on the macroscopic scale, we turn to microscopic interactions of electric dipoles in the linear optical regime. The harmonic oscillator is an excellent tool to describe light-matter interactions. It is common to use the damped driven harmonic oscillator, or the classical Drude-Lorentz model, to describe the interaction of electric dipoles and electromagnetic radiation. Figure 2.1 shows an elemental example of an external \mathbf{E} field driving a harmonic oscillator composed of a fixed positive charge and an oscillating negative charge. Phenomenologically, the harmonic oscillator model is used to describe a material constituted by a stationary positive ion lattice surrounded by bound, loosely bound, or unbound electrons.

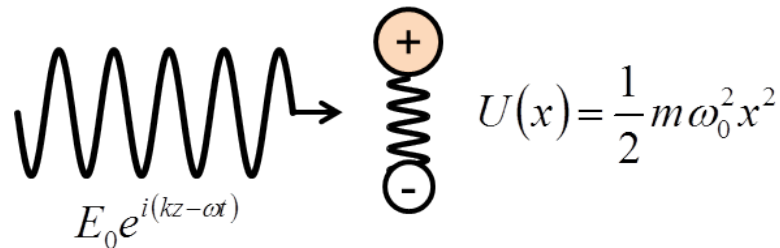


Figure 2.1: A monochromatic plane wave is incident on a spring-like binding force between a stationary positive charge and a loosely bound electron.

The underlying natural physical phenomena for the damped driven harmonic oscillator are: a driving force (in this case an external \mathbf{E} field) which provides work done onto the oscillator, a restoring force led by the natural potential well of the oscillator, and a damping force governed by frictional forces (or, material scattering mechanisms). When a monochromatic, plane wave of angular frequency, ω , irradiates the phenomenological system with polarization oriented parallel to

the charge interaction path, the electron follows the equation of motion,

$$\ddot{\mathbf{x}} + \gamma\dot{\mathbf{x}} + \omega_0^2\mathbf{x} = \frac{q}{m^*}\mathbf{E}(t) \quad (2.36)$$

where γ and ω_0 are the damping constant and resonant frequency and q and m are the charge and effective mass of the oscillator, respectively. This is the generalized equation of motion for an electron in a homogenous, linear material. The damping constant is commonly called the scattering rate in this electron-lattice system, which can also be represented by the scattering time, $\tau = 1/\gamma$, the average time between electron-lattice scattering events. The solution to the equation of motion (Eq. 2.36) is a sinusoidal displacement with resonant and damping behavior,

$$\mathbf{x}(t) = x_0(\omega)e^{-i\omega t}\hat{\mathbf{x}} \quad (2.37)$$

$$x_0(\omega) = E_0 \frac{q}{m^*} \frac{1}{\omega_0^2 - \omega^2 - i\omega\gamma} \quad (2.38)$$

The solution has resonant behavior when $\omega = \omega_0$ and damping behavior: as γ increases, $x_0(\omega)$ becomes more imaginary and the linewidth of the resonance broadens. We can make a correlation between the displacement, \mathbf{x} , and the dipole moment, \mathbf{p} , of the charge pair,

$$\mathbf{p}(t) = q\mathbf{x}(t) \quad (2.39)$$

The polarization, \mathbf{P} , of a medium with N oscillators per unit volume can be

expressed as a function of the dipole moment,

$$\mathbf{P}(t) = Nq\mathbf{x}(t) = \epsilon_0\chi_e(\omega)E_0e^{-i\omega t}\hat{x} \quad (2.40)$$

Using this formula, we can correlate the relative permittivity, ϵ_r , to the dipole moment,

$$\epsilon_r(\omega) = 1 + \chi_e(\omega) = 1 + \frac{Nq^2}{m^*\epsilon_0} \frac{1}{\omega_0^2 - \omega^2 - i\omega\gamma} \quad (2.41)$$

It is common for the investigated material to contain multiple oscillators, such as,

$$\epsilon_r(\omega) - 1 = \frac{Nq^2}{m^*\epsilon_0} \sum_i \frac{f_i}{\omega_{0i}^2 - \omega^2 - i\omega\gamma_i} \quad (2.42)$$

where the terms f_i are called the oscillator strength ($\sum_i f_i = 1$). Experimentally, when investigating a frequency region, the application of multiple oscillators is only necessary if the resonances are near the frequency region under inspection. Otherwise, a simplified model of a single oscillator is a common approach, this will be discussed in Ch. 6.

The real and imaginary components of the relative permittivity, when incorporated into the dielectric dispersion relation, Eq. 2.27,

$$k(\omega) = \sqrt{\epsilon_r(\omega)} \frac{\omega}{c} \quad (2.43)$$

governs the resonant and absorptive behavior of a propagating electromagnetic wave via the wave equation.

Material properties are defined by this frequency dependent response (e.g.,

$\epsilon_r(\omega)$, $n(\omega)$, & $k(\omega)$). Figure 2.2 shows dielectric dispersion near the resonant frequency, ω_0 .

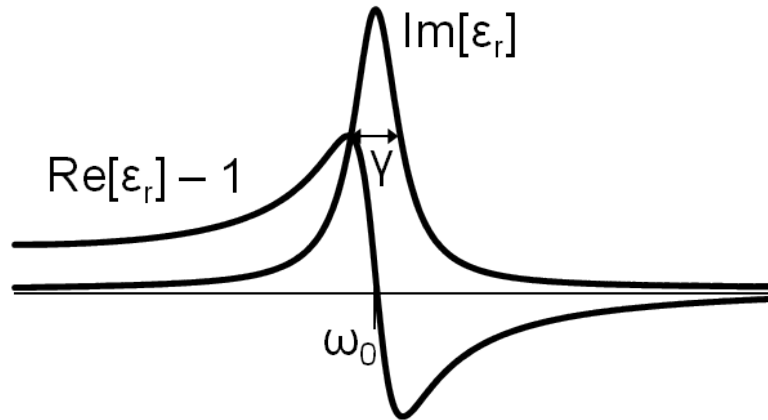


Figure 2.2: The dielectric material response to an electromagnetic wave is dependent upon the frequency and, thus, is considered a dispersive medium. ω_0 is the resonance frequency and γ is the scattering rate from Eq. 2.42.

A medium is considered frequency dispersive when electromagnetic waves of different frequencies propagate with different speeds. In the figure above, there are three regions to consider: (1) The region far from resonance can be approximated as dispersionless where there is negligible absorption and the index of refraction is approximately constant. (2) The region near resonance is called normal dispersion where the relative permittivity increases with frequency. (3) The region at resonance is called anomalous dispersion, this is the small region where the relative permittivity decreases with frequency. This causes an extreme velocity mismatch between the phase velocity,

$$v_{ph} = \frac{\omega}{k} \quad (2.44)$$

and group velocity,

$$v_{gr} = \frac{\partial \omega}{\partial k} \quad (2.45)$$

We can re-write the phase velocity and group velocity in terms of the index of refraction,

$$v_{ph} = \frac{c}{n(\omega)} \quad (2.46)$$

$$v_{gr} = \frac{c}{n(\omega) + \omega \frac{\partial n}{\partial \omega}} \quad (2.47)$$

In the region of anomalous dispersion, the slope of the index of refraction is negative. In this scenario it is possible for the group velocity to exceed the speed of light. It is common to express the v_{gr} in terms of a group index of refraction, n_{gr} ,

$$v_{gr} = \frac{c}{n_{gr}(\omega)} \quad (2.48)$$

$$n_{gr} = n(\omega) + \omega \frac{\partial n}{\partial \omega} \quad (2.49)$$

2.3 Second-Order Nonlinear Wave Equation

In Section 2.1, the linear wave equation was derived. In the derivation there was a point in which approximations negated nonlinear optical processes. This section is dedicated to that approximation, or lack thereof. When nonlinear conditions are imposed, the functional form of the wave equation results in slightly more complexity. Recall the generalized, non-magnetic wave equation, Eq. 2.16. If we make a substitution for the nonlinear polarization (from Eq. 2.18), the resulting

wave equation would look something like this:

$$\nabla^2 \mathbf{E} = \epsilon_0 \mu_0 \frac{\partial^2 \mathbf{E}}{\partial t^2} + \mu_0 \frac{\partial^2 \mathbf{P}^{(1)}}{\partial t^2} + \mu_0 \frac{\partial^2 \mathbf{P}^{\text{NL}}}{\partial t^2} \quad (2.50)$$

where $\mathbf{P}^{(1)}$ refers to the material polarization resulting from linear (1st order) optical processes and \mathbf{P}^{NL} refers to the nonlinear material polarization resulting from nonlinear (2nd, 3rd, etc. order) optical processes. Notice that the term containing σ in our grand wave equation for all materials (Eq. 2.16) was negated. This is because Taylor expansion of \mathbf{P} (Eq. 2.18) is invalid for metals ($\sigma \ll \omega\epsilon$). We can simplify this into the nonlinear wave equation for dielectrics:

$$\nabla^2 \mathbf{E} = \epsilon \mu_0 \frac{\partial^2 \mathbf{E}}{\partial t^2} + \mu_0 \frac{\partial^2 \mathbf{P}^{\text{NL}}}{\partial t^2} \quad (2.51)$$

The nonlinear wave equation (Eq. 2.51) looks similar to the linear wave equation (Eq. 2.21) except for the additive nonlinear term, \mathbf{P}^{NL} . It is this component that drives nonlinear optics in a nonlinear medium. In this section, we will discuss some consequences of our new nonlinear wave equation.

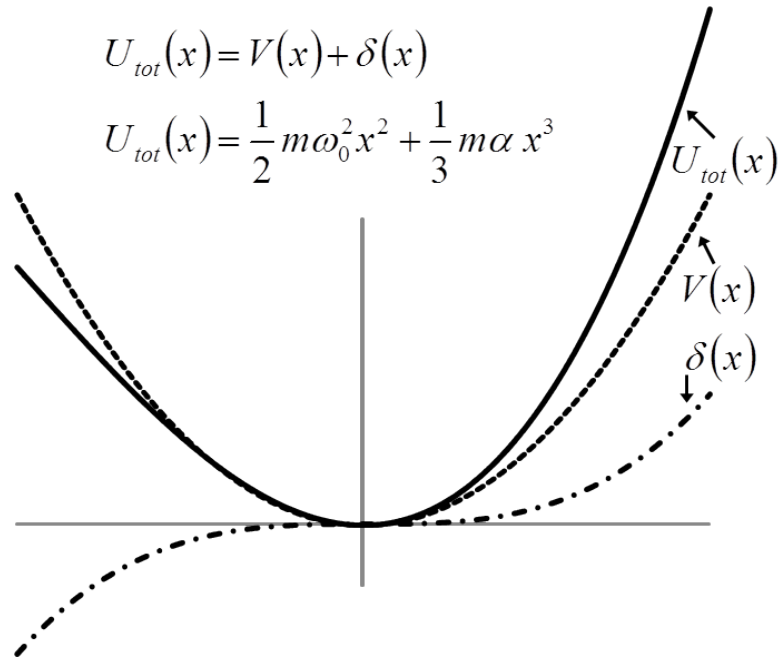


Figure 2.3: Potential energy of a noncentrosymmetric medium broken into two components: $V(x)$, potential energy from a first-order, linear dielectric response; $\delta(x)$, small ($\alpha \ll \omega_0$) anharmonic oscillator term for a second-order, nonlinear dielectric response.

When the applied electric field is sufficiently strong, large electron displacements from equilibrium yield nonlinear optical phenomena that can be addressed through the use of the harmonic oscillator model. To begin, we will look at a noncentrosymmetric medium, meaning that the medium contains no inversion symmetry. Asymmetry in such a lattice gives rise to an asymmetric potential energy (See Figure 2.3). Generally in a noncentrosymmetric medium, second-order processes will dominate nonlinear effects. This includes second harmonic generation (SHG), sum frequency generation (SFG), difference frequency generation (DFG), optical rectification (OR), and the electro-optic effect (EO). From a harmonic oscillator

model approach, the addition of a small asymmetric potential energy term can be addressed with perturbation theory:

$$U_{tot}(x) = V(x) + \delta(x) \quad (2.52)$$

$$U_{tot}(x) = \frac{1}{2}m^*\omega_0^2x^2 + \frac{1}{3}m^*\alpha x^3 \quad (2.53)$$

where the perturbative parameter, α , is sufficiently small ($\alpha \ll \omega_0^2$) and $\delta(x)$ is not the Dirac delta function. Perturbation holds when the displacement (or, in this case the field) is sufficiently weak ($\alpha x^3 \ll \omega_0^2 x^2$). However, nonlinear effects will not arise until the nonlinear potential energy term(s) become comparable to the first-order potential energy term. These terms remain incomparable until either the perturbative parameter, α , or the displacement parameter, x , are large enough.

In a perturbative formulation, we would like to derive the anharmonic response of a nonlinear material. To begin, let's write the equation of motion,

$$\ddot{x} + \gamma\dot{x} + \omega_0^2x + \alpha x^2 = \frac{q}{m^*}E(t) \quad (2.54)$$

which is similar to the linear harmonic oscillator equation of motion except for the anharmonic term, αx^2 . The anharmonic term represents the forcing of the perturbative asymmetric potential energy.

So long as the asymmetric potential energy term is sufficiently small, we can utilize perturbation theory to solve the nonlinear equation of motion. The introduction of an expansion parameter, η , allows for us to categorize the perturbative

expansion and analyze with the perturbation procedure more easily ($\eta = 1$),

$$\ddot{x} + \gamma\dot{x} + \omega_0^2 x + \alpha x^2 = \eta \frac{q}{m^*} E(t) \quad (2.55)$$

We will assume two incident frequencies because the second-order nonlinear optical process requires two photons to satisfy the nonlinear equation of motion (Eq. 2.54).

$$E(t) = E_1 e^{-i\omega_1 t} + E_2 e^{-i\omega_2 t} + c.c. \quad (2.56)$$

The perturbation procedure suggests we express the position as a Taylor expansion of nonlinear terms such that displacements are small and within the perturbative regime,

$$x = \eta x^{(1)} + \eta^2 x^{(2)} + \eta^3 x^{(3)} + \dots \quad (2.57)$$

Convergence is assumed:

$$x^{(1)} \gg x^{(2)} \gg x^{(3)} \dots \quad (2.58)$$

From these assumptions, we can substitute x (Eq. 2.57) into the equation of motion (Eq. 2.54) and begin organizing in terms of η^n . This leaves us with a

nonlinear system of equations:

$$\eta \rightarrow \ddot{x}^{(1)} + \gamma \dot{x}^{(1)} + \omega_0^2 x^{(1)} = \frac{q}{m^*} E(t) \quad (2.59)$$

$$\eta^2 \rightarrow \ddot{x}^{(2)} + \gamma \dot{x}^{(2)} + \omega_0^2 x^{(2)} + \alpha [x^{(1)}]^2 = 0 \quad (2.60)$$

$$\eta^3 \rightarrow \ddot{x}^{(3)} + \gamma \dot{x}^{(3)} + \omega_0^2 x^{(3)} + 2\alpha x^{(1)} x^{(2)} = 0 \quad (2.61)$$

The 1st order (linear) response corresponds directly to the Harmonic Oscillator model discussed in Section 2.2. All solutions therein can be inferred. For simplification, we will represent the denominator of Eq. 2.38 in the following way:

$$D(\omega) = \omega_0^2 - \omega^2 - i\omega\gamma \quad (2.62)$$

so that the equation of motion, bulk polarization, and linear susceptibility can be written as follows:

$$x^{(1)}(t) = x^{(1)}(\omega_1) e^{-i\omega_1 t} + x^{(1)}(\omega_2) e^{-i\omega_2 t} + c.c. \quad (2.63)$$

$$x^{(1)}(\omega_i) = \frac{q}{m^*} \frac{E(\omega_i)}{D(\omega_i)} \quad (2.64)$$

$$P^{(1)}(\omega_i) = Nq x^{(1)}(\omega_i) = \epsilon_0 \chi^{(1)}(\omega_i) E(\omega_i) \quad (2.65)$$

$$\chi^{(1)}(\omega_i) = \frac{Nq^2}{m^* \epsilon_0} \frac{1}{D(\omega_i)} \quad (2.66)$$

where the subscript, $i = \{1, 2\}$, represents the single frequency contributors. In

higher order processes, the number of frequency contributors, i , is typically equal to the order of the process. In the linear response of a second-order nonlinear optical process, there are two photons going in to the nonlinear medium and two photons coming out.

In the 2nd order response, η^2 (Eq. 2.60), we expect a two photon process:

$$\ddot{x}^{(2)} + \gamma \dot{x}^{(2)} + \omega_0^2 x^{(2)} = -\alpha [x^{(1)}]^2 \quad (2.67)$$

Before we substitute our solutions from the 1st order response (Eq. 2.63), we must first find the possible combinations of frequencies for our 2nd order response solutions:

$$[x^{(1)}]^2 = [x^{(1)}(\omega_1) e^{-i\omega_1 t} + x^{(1)}(\omega_2) e^{-i\omega_2 t} + c.c.]^2 \quad (2.68)$$

$$\text{(SHG of } \omega_1) \rightarrow = [x^{(1)}(\omega_1)]^2 e^{-i2\omega_1 t} + c.c. + \dots \quad (2.69)$$

$$\text{(SHG of } \omega_2) \rightarrow + [x^{(1)}(\omega_2)]^2 e^{-i2\omega_2 t} + c.c. + \dots \quad (2.70)$$

$$\text{(SFG)} \rightarrow + 2x^{(1)}(\omega_1) x^{(1)}(\omega_2) e^{-i(\omega_1+\omega_2)t} + c.c. + \dots \quad (2.71)$$

$$\text{(DFG)} \rightarrow + 2x^{(1)}(\omega_1) x^{*(1)}(\omega_2) e^{-i(\omega_1-\omega_2)t} + c.c. + \dots \quad (2.72)$$

$$\text{(OR)} \rightarrow + 2|x^{(1)}(\omega_1)|^2 + 2|x^{(1)}(\omega_2)|^2 \quad (2.73)$$

Each second-order nonlinear optical process contains a different frequency. This means that only one general solution per process is allowed. We can implement

$[x^{(1)}]^2$ into the 2nd order equation of motion (Eq. 2.67) depending on which process is chosen. Below is a general representation of $[x^{(1)}]^2$, independent of the second-order process:

$$[x^{(1)}]^2 = \beta x^{(1)}(\omega_j) x^{(1)\xi}(\omega_k) e^{-i(\omega_j \pm \omega_k)t} + \text{c.c.} \quad (2.74)$$

where $\beta = 1$ for SHG and $\beta = 2$ for SFG, DFG, OR, and EO and $\xi = *$ for DFG, OR, and EO ($*$ represents the complex conjugate). With our generalized expression for $[x^{(1)}]^2$, we can re-write the 2nd order equation of motion in terms of arbitrary input frequencies, ω_j and ω_k , and arbitrary second-order process.

$$\ddot{x}^{(2)} + \gamma \dot{x}^{(2)} + \omega_0^2 x^{(2)} = -\beta \alpha x^{(1)}(\omega_j) x^{(1)\xi}(\omega_k) e^{-i(\omega_j \pm \omega_k)t} \quad (2.75)$$

Based on the exponential on the right-hand side of the equation, the solution for $x^{(2)}$ depends on the second-order process and will be labeled with ω_i , where $\omega_i = \omega_j \pm \omega_k$. The solutions to the second-order equation of motion, bulk polarization,

and linear susceptibility follow:

$$x^{(2)}(t) = x^{(2)}(\omega_i) e^{-i\omega_i t} + c.c. \quad (2.76)$$

$$x^{(2)}(\omega_i) = -\beta\alpha \left(\frac{q}{m^*}\right)^2 \frac{E(\omega_j) E^\xi(\omega_k)}{D(\omega_i) D(\omega_j) D^\xi(\omega_k)} \quad (2.77)$$

$$P^{(2)}(\omega_i) = Nq x^{(2)}(\omega_i) = \beta\epsilon_0 \chi^{(2)}(\omega_i, \omega_j, \omega_k) E(\omega_j) E^\xi(\omega_k) \quad (2.78)$$

$$\chi^{(2)}(\omega_i, \omega_j, \omega_k) = -\frac{Nq^3\alpha}{m^2\epsilon_0} \frac{1}{D(\omega_i) D(\omega_j) D^\xi(\omega_k)} \quad (2.79)$$

These solutions are all encompassing for each second order nonlinear optical process. For an example of each process, here is a list of the possible solutions for second-order polarization extracted from the resulting second-order susceptibility from the equation of motion (Eq. 2.75):

$$\text{SHG} \rightarrow P^{(2)}(2\omega_i) = \epsilon_0 \chi^{(2)}(2\omega_i, \omega_i, \omega_i) E(\omega_i) E(\omega_i) \quad (2.80)$$

$$\text{SFG} \rightarrow P^{(2)}(\omega_1 + \omega_2) = 2\epsilon_0 \chi^{(2)}(\omega_1 + \omega_2, \omega_1, \omega_2) E(\omega_1) E(\omega_2) \quad (2.81)$$

$$\text{DFG} \rightarrow P^{(2)}(\omega_1 - \omega_2) = 2\epsilon_0 \chi^{(2)}(\omega_1 - \omega_2, \omega_1, -\omega_2) E(\omega_1) E^*(\omega_2) \quad (2.82)$$

$$\text{OR} \rightarrow P^{(2)}(0) = 2\epsilon_0 \chi^{(2)}(0, \omega_i, -\omega_i) E(\omega_i) E^*(\omega_i) \quad (2.83)$$

$$\text{EO} \rightarrow P^{(2)}(\omega_i) = 2\epsilon_0 \chi^{(2)}(\omega_i, \omega_i, 0) E(\omega_i) E^*(0) \quad (2.84)$$

You'll notice that $\omega_i = 0$ in OR. We use OR for THz generation where the THz frequencies are approximately 1-THz. How OR can be used for generating THz

frequencies will be discussed in Section 2.4. The indices (i.e., $\{i, j, k\}$) so far in this section have corresponded to a photon counter. In the following discussion, it will be used as a Cartesian coordinate counter (i.e., $\{i, j, k\} = \{x, y, z\}$). The nonlinear material polarization is frequency and orientation dependent. In a general representation of all second-order processes, this is how the indices combine: You'll notice that $\omega_i = 0$ in OR. We use OR for THz generation where the THz frequencies are approximately 1-THz. How OR can be used for generating THz frequencies will be discussed in Section 2.4. The indices (i.e., $\{i, j, k\}$) so far in this section have corresponded to a photon counter. In the following discussion, it will be used as a Cartesian coordinate counter (i.e., $\{i, j, k\} = \{x, y, z\}$). The nonlinear material polarization is frequency and orientation dependent. In a general representation of all second-order processes, this is how the indices combine:

$$P_i^{(2)}(\omega_3) = \sum_{j,k} \left[\beta \epsilon_0 \chi_{ijk}^{(2)}(\omega_3, \omega_2, \omega_1) E_j(\omega_2) E_k^\xi(\omega_1) \right] \quad (2.85)$$

From this equation, we see that by mixing Cartesian coordinates, $\{i, j, k\}$, it is possible to take two electromagnetic waves in arbitrary direction and arbitrary frequency and generate a dielectric polarization with arbitrary direction and a frequency that satisfies the selection rule: $\omega_3 = \pm\omega_1 \pm \omega_2$. Figure 2.4 shows a typical diagram for second-order nonlinear optical processes.

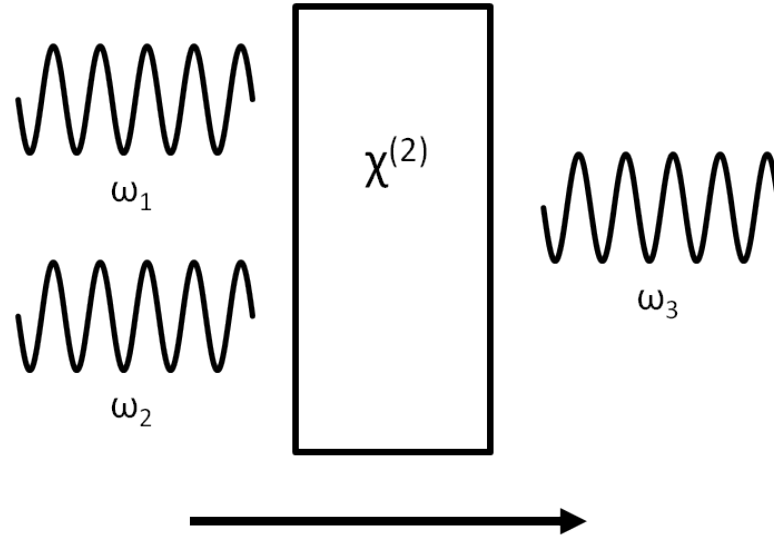


Figure 2.4: A second-order nonlinear crystal is capable of wave-mixing three photons of different frequency: ω_1 , ω_2 , and ω_3 . Wave-mixing processes include: sum frequency generation ($\omega_1 + \omega_2 = \omega_3$), difference frequency generation ($\omega_1 - \omega_2 = \omega_3$), optical rectification ($\omega_3 = 0$), and electro-optic sampling (ω_1 or $\omega_2 = 0$).

In common materials, indices $\{j, k\}$ are permutable, so we can use contracted notation (Refer to [4]):

$$d_{il} = \frac{1}{2} \chi_{ijk}^{(2)} \quad (2.86)$$

See Table 2.1 to correlate the contracted notation with the non-contracted notation

l =	1	2	3	4	5	6
jk =	11	22	33	23 , 32	31 , 13	12, 21

Table 2.1: The element correspondance between the contracted susceptibility matrix, d_{il} , and the second-order susceptibility tensor, $\chi_{ijk}^{(2)}$

Contracting χ_{ijk} (a tensor) into d_{il} (a matrix) allows for simpler matrix mul-

tiplication. By using the contracted notation, we can describe the second order dielectric polarization from Eq. 2.85 as a vector,

$$\begin{pmatrix} P_x \\ P_y \\ P_z \end{pmatrix} = 2\epsilon_0 d_{il} \begin{pmatrix} E_x^2 \\ E_y^2 \\ E_z^2 \\ 2E_y E_x \\ 2E_z E_x \\ 2E_y E_z \end{pmatrix} \quad (2.87)$$

Zinc Telluride (ZnTe) and Lithium Niobate (LiNbO₃) are two commonly used nonlinear crystals for THz generation and detection. Both crystals exhibit crystal structure symmetry. These symmetries shine through their contracted matrix elements and can be found in Table 2.2.

Material	Crystal Class	d_{il}
ZnTe	$\bar{4}3m$	$\begin{pmatrix} 0 & 0 & 0 & d_{14} & 0 & 0 \\ 0 & 0 & 0 & 0 & d_{14} & 0 \\ 0 & 0 & 0 & 0 & 0 & d_{14} \end{pmatrix}$
LiNbO ₃	3m	$\begin{pmatrix} 0 & 0 & 0 & 0 & d_{15} & -d_{22} \\ -d_{22} & d_{22} & 0 & d_{15} & 0 & 0 \\ d_{15} & d_{15} & d_{33} & 0 & 0 & 0 \end{pmatrix}$

Table 2.2: Contracted susceptibility, d_{ij} , for ZnTe and LN.

ZnTe contains a tetrahedral geometry and falls under the crystal class $\bar{4}3m$.

These symmetries make ZnTe an excellent candidate for both OR and EO sampling. It is a common solution for THz generation and detection. The $\bar{4}3m$ crystal class exudes symmetry in three non-vanishing contracted matrix elements ($d_{14} = d_{25} = d_{36}$). In ZnTe, the d_{14} element is responsible for THz generation and detection. In LiNbO₃, the d_{33} element is responsible for THz generation. Of course, the larger the second-order elements, the more efficient the energy conversion. Here are the well known values for these matrix elements, [6]

$$d_{14}^{\text{ZnTe}} = 4 \text{ pm/V} \quad (2.88)$$

$$d_{33}^{\text{LiNbO}_3} = 31 \text{ pm/V} \quad (2.89)$$

Consequently, the symmetry in ZnTe makes THz generation alignment simple while the lack of symmetry in LiNbO₃ makes alignment challenging. However, due to the large $d_{33}^{\text{LiNbO}_3}$ element, THz generation conversion efficiency is much greater in LiNbO₃ ($\eta_{\text{LN}} \sim 10^{-3}$) than ZnTe ($\eta_{\text{ZnTe}} \sim 10^{-5}$).

The THz polarization (i.e., the nonlinear material polarization) direction depends on the optical field direction relative to the crystal orientation, hence, the indices of Eq. 2.85. If we focus our attention onto ZnTe, we can utilize the symmetry of the d_{il} matrix to make a general formulation for THz generation and detection. As mentioned before, the OR material polarization is a DC field that follows the optical field amplitude “envelope”. In our laser system, the optical field amplitude envelope contains a Gaussian profile. As such, the nonlinear material polarization (THz polarization) will follow that envelope. See Figure 2.5 for

visualization. The THz field then follows the second-order derivative of the THz polarization Gaussian envelope, thus satisfying the nonlinear wave equation (Eq. 2.51).

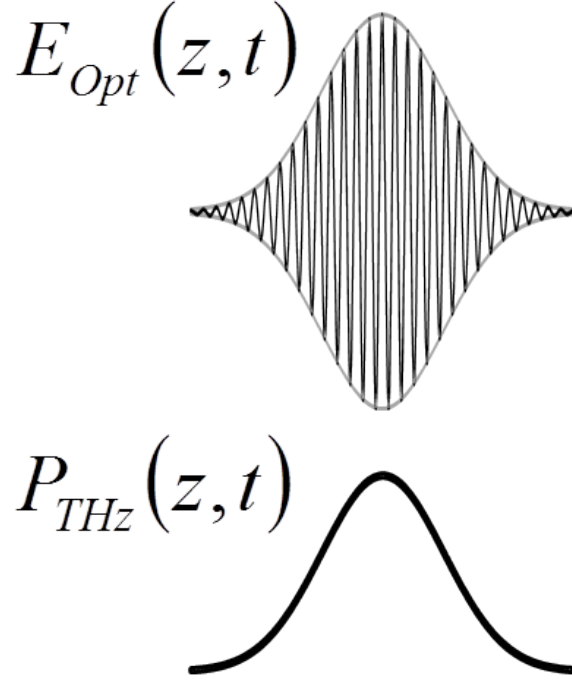


Figure 2.5: Optical electric field and Gaussian amplitude envelope (top) and non-linear material polarization (THz polarization) for OR process (bottom) in second-order nonlinear medium.

To begin, we can consider a CW optical field envelope to simplify our concept. If we express an arbitrary optical field in spherical coordinates,

$$\mathbf{E}_0 = E_0 \begin{pmatrix} \sin \theta \cos \phi \\ \sin \theta \sin \phi \\ \cos \theta \end{pmatrix} \quad (2.90)$$

with polar angle, θ , and azimuthal angle, ϕ , then the THz polarization from Eq. 2.87 simplifies to:

$$\begin{pmatrix} P_x \\ P_y \\ P_z \end{pmatrix} = 4\epsilon_0 d_{14} E_0^2 \sin \theta \begin{pmatrix} \cos \theta \sin \phi \\ \cos \theta \cos \phi \\ \sin \theta \sin \phi \cos \phi \end{pmatrix} \quad (2.91)$$

The THz field resulting from the THz polarization is parallel ($\mathbf{E}_{\text{THz}} \parallel \mathbf{P}^{(2)}$) and the intensity of the THz radiation follows:

$$I_{\text{THz}}(\theta, \phi) \propto |\mathbf{P}|^2 = 4\epsilon_0^2 d_{14}^2 E_0^4 \sin^2 \theta (4 \cos^2 \theta + \sin^2 \theta \sin^2 2\phi) \quad (2.92)$$

In ZnTe, an optical incidence angle parallel to the $[110]$ crystal axis would represent $\phi = 0$,

$$I_{\text{THz}}(\theta) = \frac{3}{4} I_{\text{THz}}^{\text{max}} \sin^2 \theta (4 - 3 \sin^2 \theta) \quad (2.93)$$

Maximum THz generation intensity occurs when the incident optical field is parallel to either the $[\bar{1}11]$ or $[1\bar{1}1]$ crystal axis. These crystal directions correspond to the chemical bonds between Zn and Te. Figure 2.6 below shows experimental data compared to the theoretical model of Eq. 2.93.

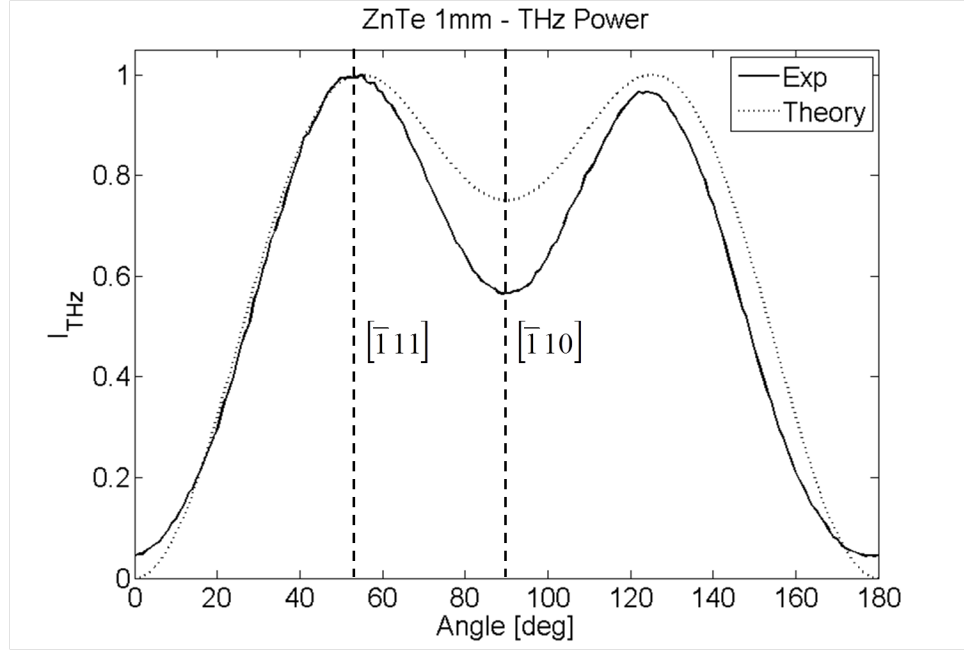


Figure 2.6: Theoretical (dashed) and experimental (solid) THz radiation generated depending on optical polarization angle with respect to the ZnTe crystal orientation about the $[110]$ incident axis.

If we rotate the ZnTe crystal such that the optical incident angle remains parallel to the $[110]$ crystal axis, we can determine the corresponding THz field strength:

$$\mathbf{E}_{\text{THz}}(\theta) = \frac{\sqrt{3}}{2} E_{\text{THz}}^{\max} \sin \theta \begin{pmatrix} \sqrt{2} \cos \theta \\ -\sqrt{2} \cos \theta \\ -\sin \theta \end{pmatrix} \quad (2.94)$$

In Eq. 2.94 there are three special polar angles in which the incident optical field directions manifests a special THz field direction. These angles can be found in Table 2.3.

\mathbf{E}_{Opt} -direction	\mathbf{E}_{THz} -direction
[011]	0
$[\bar{1}11]$	$\parallel -\mathbf{E}_{\text{Opt}}$
$[\bar{1}10]$	$\perp \mathbf{E}_{\text{Opt}}$

Table 2.3: THz polarization depends on the optical polarization relative to crystal orientation. Listed are three special directions of polarization.

These angles are important because experimentally, they allow you to control the output THz polarization direction by leaving the optical polarization untouched and simply rotating the ZnTe crystal orientation about the [110] crystal axis.

2.4 Velocity Matching

If we refer back to the nonlinear wave equation (Eq. 2.51), we can make the substitution for second-order processes,

$$\mathbf{P}^{\text{NL}} = \mathbf{P}_{\text{THz}}^{(2)}(z, t) = \epsilon_0 \chi^{(2)} |\mathbf{E}_{\text{Opt}}(z, t)|^2 \quad (2.95)$$

Assuming the wave propagates along the z-axis and the electromagnetic waves are monochromatic plane waves, the resulting THz wave equation for second-order processes follows:

$$\frac{\partial^2 \mathbf{E}(z, t)}{\partial z^2} - \frac{n^2}{c^2} \frac{\partial^2 \mathbf{E}(z, t)}{\partial t^2} = \frac{\chi^{(2)}}{c^2} \frac{\partial^2 \mathbf{P}^{(2)}(z, t)}{\partial t^2} \quad (2.96)$$

Refer back to Figure 2.4 where we observe two incident photons and one output photon. We can simplify the above equation (Eq. 2.96) if we utilize the following for the field equations:

$$\mathbf{E}_i(z, t) = A_i e^{i(k_i z - \omega_i t)} \quad (2.97)$$

where $k_i = n_i \frac{\omega_i}{c}$. Recalling Eq. 2.78, we can substitute the spatial field equation into the nonlinear material polarization,

$$\mathbf{P}_3(z, t) = \beta \epsilon_0 \chi^{(2)} E_1(z, t) E_2^\xi(z, t) \quad (2.98)$$

And the wave equation (Eq. 2.96) for a general second-order nonlinear optical process results,

$$\frac{\partial^2 \mathbf{E}_3(z, t)}{\partial z^2} - \frac{n_3^2}{c^2} \frac{\partial^2 \mathbf{E}_3(z, t)}{\partial t^2} = \frac{1}{\epsilon_0 c^2} \frac{\partial^2 \mathbf{P}_3(z, t)}{\partial t^2} \quad (2.99)$$

$$\frac{\partial^2 (A_3 e^{ik_3 z - i\omega_3 t})}{\partial z^2} - \frac{n_3^2}{c^2} \frac{\partial^2 (A_3 e^{ik_3 z - i\omega_3 t})}{\partial t^2} = \frac{\beta \chi^{(2)}}{c^2} \frac{\partial^2 (A_1 A_2 e^{i(k_1 + \xi k_2)z} e^{-i(\omega_1 \pm \omega_2)z})}{\partial t^2} \quad (2.100)$$

$$\left(\frac{\partial^2 A_3}{\partial z^2} + 2ik_3 \frac{\partial A_3}{\partial z} - k_3^2 A_3 + \frac{n_3^2 \omega_3^2}{c^2} A_3 \right) e^{ik_3 z} = -\frac{\beta \chi^{(2)} \omega_3^2}{c^2} A_1 A_2 e^{i(k_1 + \xi k_2)z} \quad (2.101)$$

$$\frac{\partial^2 A_3}{\partial z^2} + 2ik_3 \frac{\partial A_3}{\partial z} = -\frac{\beta \chi^{(2)} \omega_3^2}{c^2} A_1 A_2 e^{i(k_1 + \xi k_2 - k_3)z} \quad (2.102)$$

where $\xi = -1$ for DFG and OR, $\xi = 0$ for EO and $\xi = +1$ for SHG and SFG. If we assume that the wavelength, λ , is much smaller than the pulse length, ℓ ($\ell \gg \lambda$),

then we can make the Slowly Varying Envelope Approximation (SVEA),

$$\left| \frac{\partial^2 A_3}{\partial z^2} \right| \ll \left| k_3 \frac{\partial A_3}{\partial z} \right| \quad (2.103)$$

The SVEA breaks down when the number of cycles is minimized (i.e., single cycle pulses). The wave equation becomes,

$$\frac{\partial A_3}{\partial z} = \frac{i\beta\chi^{(2)}\omega_3^2}{2k_3c^2} A_1 A_2 e^{i\Delta kz} \quad (2.104)$$

where $\Delta k = k_1 + \xi k_2 - k_3$ is the wave vector (or momentum, velocity, or phase) mismatch. Velocity matching conditions require $\Delta k = 0$, a list of these conditions for each second-order process can be found in Table 2.4.

2nd-order process	$\Delta k = 0$
SHG for ω_1	$2k_1 = k_3$
SHG for ω_2	$2k_2 = k_3$
SFG	$k_1 + k_2 = k_3$
DFG	$k_1 - k_2 = k_3$
OR	$k_1 = k_2$
EO	$k_1 = k_3$

Table 2.4: Velocity matching conditions ($\Delta k = 0$) for each second-order nonlinear process.

If we assume that A_1 and A_2 are constant, then we can solve for the generation

of A_3 over the length of the nonlinear medium,

$$A_3(L) = \frac{i\beta\chi^{(2)}\omega_3^2 A_1 A_2}{2k_3 c^2} \left[\frac{e^{i\Delta k L} - 1}{i\Delta k} \right] \quad (2.105)$$

$$= \frac{i\beta\chi^{(2)}\omega_3^2 A_1 A_2}{2k_3 c^2} L \operatorname{sinc}(\Delta k L/2) \quad (2.106)$$

and intensity ($I_3 = \frac{1}{2}\epsilon_0 c n_3 |A_3|^2$),

$$I_3(L) = \frac{\beta\epsilon_0 n_3 \omega_3^4 |\chi^{(2)}|^2 |A_1|^2 |A_2|^2}{4k_3^2 c^3} L^2 \operatorname{sinc}^2(\Delta k L/2) \quad (2.107)$$

$$= \frac{\beta\omega_3^2 |\chi^{(2)}|^2}{\epsilon_0 n_1 n_2 n_3 c^3} I_1 I_2 L^2 \operatorname{sinc}^2(\Delta k L/2) \quad (2.108)$$

The THz generation intensity is proportional to L^2 so long as the velocity matching condition is satisfied ($\Delta k = 0$). So with velocity mismatch, $\Delta k z = \pi$, the coherence length of THz generation will occur at $L = 2/\Delta k$.

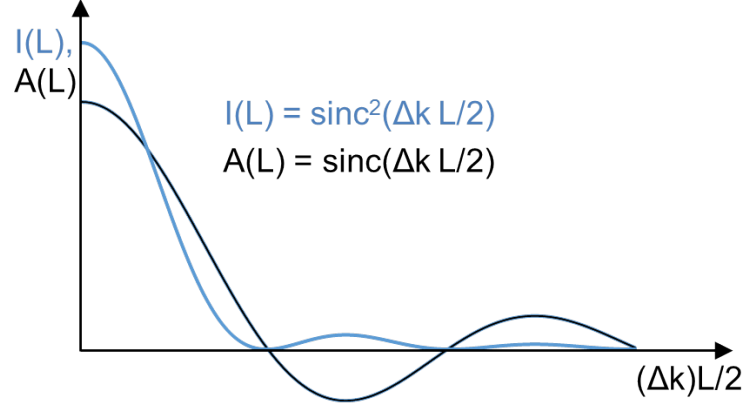


Figure 2.7: As an optical wave propagates through a nonlinear medium stimulating a second-order nonlinear process, interference occurs with velocity mismatch ($\Delta k \neq 0$) and length of propagation, L .

With perfect velocity matching, there is no risk of decoherence. However, with slight mismatch the nonlinear material polarization decoheres with increased length due to interference caused by the velocity mismatch.

Velocity mismatch is commonly found in most materials except for extremely special scenarios. When the optical pulse propagates faster than the THz pulse ($n_{\text{THz}} > n_{\text{Opt}}$), the optical pulse will temporally lead the THz pulse by the optical pulse duration, τ_p , after a longitudinal walk-off length, ℓ_w ,

$$\ell_w = \frac{c\tau_p}{n_{\text{THz}} - n_{\text{Opt}}} \quad (2.109)$$

This means that destructive interference of the generated THz fields will occur when $z = \ell_w$. Once the thickness of the nonlinear medium is much longer than the walk-off length ($\ell \gg \ell_w$), the total generated THz field vanishes, $E_{\text{THz}} = 0$.

In the wave equation, the velocity matching condition implies the matching velocities necessary for a nonlinear process to take place. However, in OR there is no real phase that occurs in DC radiation. If we consider a Gaussian pulsed laser, OR maps the optical pulse envelope which propagates at the optical group velocity. So, in the case of THz generation via OR, the optical group refractive index must be velocity matched with the THz phase refractive index ($n_{\text{Opt}}^{\text{gr}} = n_{\text{THz}}^{\text{ph}}$). This concept can be explained through a picture (Figure 2.8),

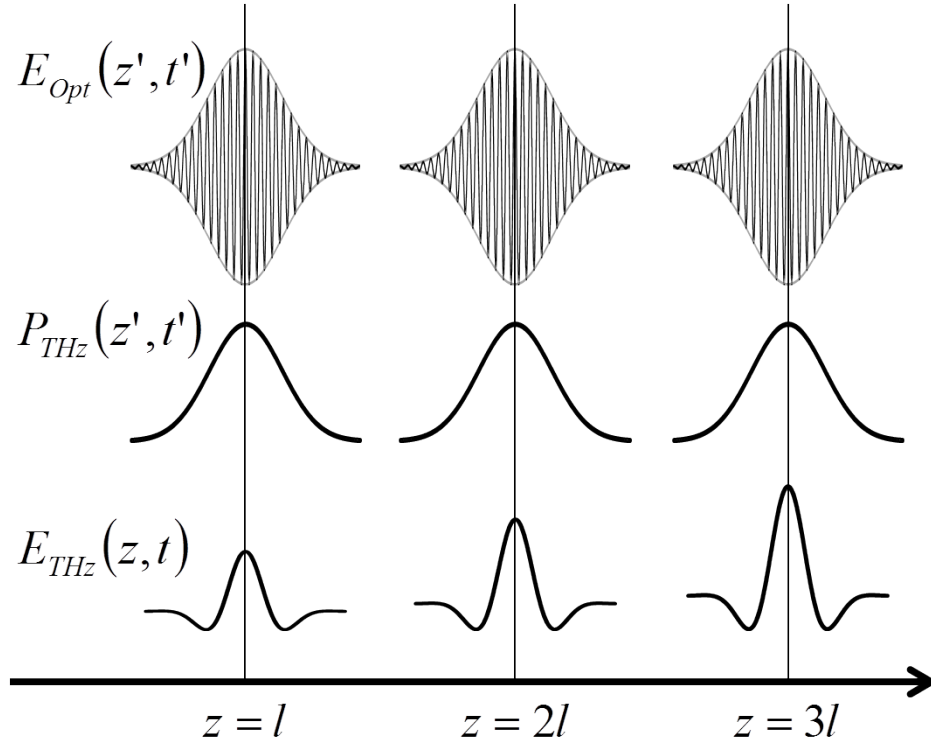


Figure 2.8: As the optical pulse propagates through the material, a nonlinear material (THz) polarization is generated via second-order nonlinear processes, and a THz field is generated through velocity matching of the optical group velocity, $v_{\text{Opt}}^{\text{gr}}$, of the optical pulse envelope, and the THz phase velocity, $v_{\text{THz}}^{\text{ph}}$, of said THz field.

The nonlinear material polarization follows the field envelope of the optical pulse. As the optical pulse envelope propagates through the crystal with group velocity, $v_{\text{Opt}}^{\text{gr}}$, it must coincide with the phase velocity of the THz field, $v_{\text{THz}}^{\text{ph}}$, generated through the material polarization. Otherwise, the THz fields will destructively interfere through the velocity mismatch of the optical envelope with the THz phase.

The index of refraction in IR and THz of ZnTe follow,

$$n_{\text{Opt-ph}}^{\text{ZnTe}}(\lambda_{\mu\text{m}}) = \sqrt{4.27 + \frac{3.01\lambda_{\mu\text{m}}^2}{\lambda_{\mu\text{m}}^2 - 0.142}} \quad (2.110)$$

$$n_{\text{THz-ph}}^{\text{ZnTe}}(\nu_{\text{THz}}) = \sqrt{\frac{289.27 - 6\nu_{\text{THz}}^2}{29.16 - \nu_{\text{THz}}^2}} \quad (2.111)$$

where $\lambda_{\mu\text{m}}$ is in units of μm and ν_{THz} is in THz. The beauty of ZnTe is that velocity matching occurs at $n_{\text{Opt-gr}}^{\text{ZnTe}}(0.812 \mu\text{m}) = n_{\text{THz-ph}}^{\text{ZnTe}}(1.69 \text{ THz}) = 3.216$ as shown in Figure 2.9 (Refer to [5]). However, the optical phase velocity is severely mismatched ($n_{\text{Opt-ph}}^{\text{ZnTe}}(0.812 \mu\text{m}) = 2.847$). This makes other second-order processes such as DFG walk-off fairly rapidly ($\ell_w = 81.3\text{-}\mu\text{m}$ for $\tau_p = 100\text{-fs}$, $\ell_w = 3.74\text{-mm}$ for $\tau_p = 4.6\text{-ps}$) [7].

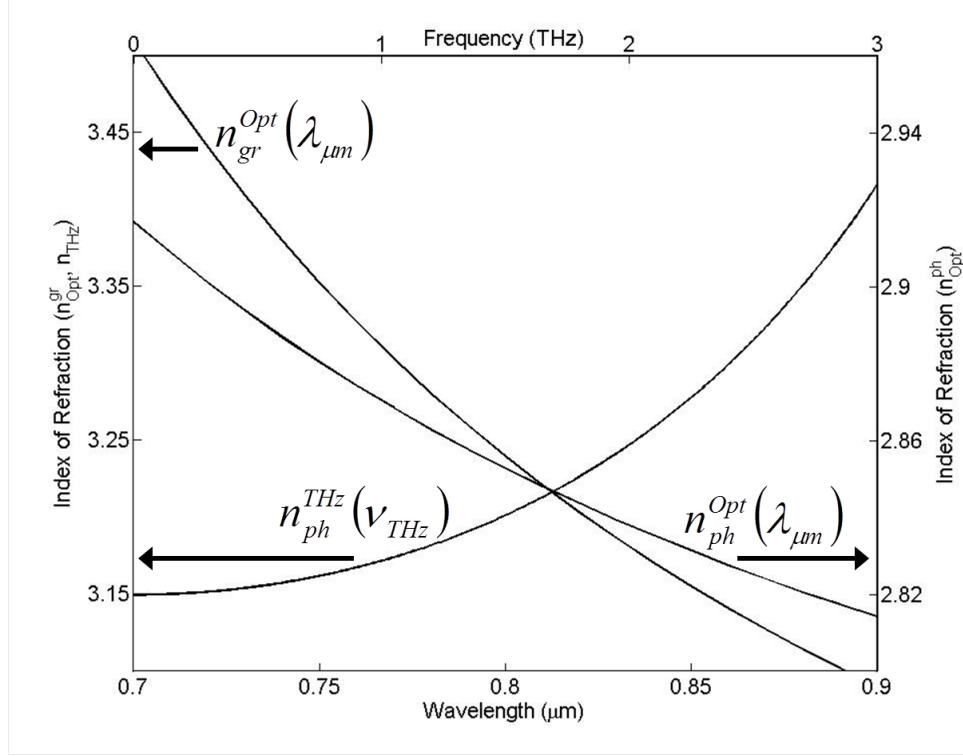


Figure 2.9: Optical group index of refraction, $n_{\text{Opt-gr}}^{\text{ZnTe}}(\lambda_{\mu\text{m}})$, and THz phase index of refraction, $n_{\text{THz-ph}}^{\text{ZnTe}}(\nu_{\text{THz}})$, for ZnTe.

To quantify the absorption coefficient in ZnTe at THz frequencies, we can look at the imaginary component of the relative permittivity,

$$\epsilon_{\text{THz-ph}}^{\text{ZnTe}}(\nu_{\text{THz}}) = \epsilon_{\text{el}} + \frac{\epsilon_{\text{st}}\nu_{\text{TO}}^2}{\nu_{\text{TO}}^2 - \nu^2 + 2i\gamma\nu} \quad (2.112)$$

where $\epsilon_{\text{el}} = 7.44$, $\epsilon_{\text{st}} = 2.58$, and $\gamma = 0.025$ THz. There is a strong TO-phonon resonance at $\nu_{\text{TO}} = 5.32$ THz at room temperature (Refer to [5]).

The optical phase index of refraction for 1% MgO-doped stoichiometric Lithium

Niobate follows,

$$n_{\text{Opt-ph}}^{\text{LN}}(\lambda_{\mu\text{m}}) = \sqrt{\frac{4.290 \times 10^{15}}{7.037 \times 10^{13} (\lambda_{\mu\text{m}}^2 - 111.3)} + \frac{6.937 \times 10^{15}}{7.206 \times 10^{16} (\lambda_{\mu\text{m}}^2 - 0.0427)} - 0.0159\lambda_{\mu\text{m}}^2 + 5.077} \quad (2.113)$$

$$n_{\text{Opt-gr}}^{\text{LN}}(\lambda_{\mu\text{m}}) = n_{\text{Opt-ph}}^{\text{LN}} - \lambda_{\mu\text{m}} \frac{dn_{\text{Opt-ph}}^{\text{LN}}}{d\lambda_{\mu\text{m}}} \quad (2.114)$$

The optical group and phase index of refraction are similar ($n_{\text{Opt-gr}}^{\text{LN}}(800\mu\text{m}) = 2.249$, $n_{\text{Opt-ph}}^{\text{LN}}(800\mu\text{m}) = 2.163$). Of course, we use the optical group index of refraction for velocity matching OR and the optical phase index of refraction for all other second-order processes. The THz phase index of refraction has been studied as a function of phonon resonances and can be seen in Figure 2.10 [8].

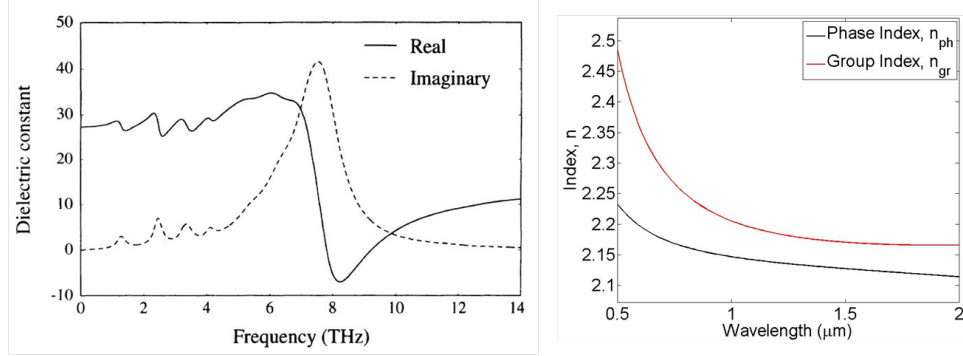


Figure 2.10: Optical group index of refraction, $n_{\text{Opt-gr}}^{\text{LN}}(\lambda_{\mu\text{m}})$, and THz phase index of refraction, $n_{\text{THz-ph}}^{\text{LN}}(\nu_{\text{THz}})$, for Lithium Niobate.

The THz index of refraction is assumed to simply be a constant, $n_{\text{THz}}^{\text{LN}} = 5.2$. The drastic difference in index for Lithium Niobate makes velocity matching impossible for co-propagating optical and THz beams. To make THz generation

possible, one must tilt the pulse-front. This will be discussed later in Sec. 3.2.

2.5 Pockels Effect

Free-space EO sampling measures a THz electric field waveform in the time-domain, determining both amplitude and phase with high precision ($< 10^{-2}$ rad). The Pockels effect is the underlying mechanism in EO sampling and has similarity with the second-order nonlinear polarization of OR as seen in Eqs. 2.83 and 2.84. In a lossless medium, the Pockels effect has the same nonlinear optical coefficients as OR ($\chi^{(2)}(0, \omega, -\omega) = \chi^{(2)}(\omega, \omega, 0)$).

The Pockels effect takes a static electric field and induces a birefringence in the EO crystal that is proportional to the applied electric field. Thus, the applied electric field can be measured by the polarization rotation of a transmitted optical beam. For THz purposes, the static electric field takes form of a THz waveform. Still, the Pockels effect is fast enough in the EO crystal such that the THz waveform can be mapped out in the time-domain by varying the time-delay between the optical pulse and THz pulse. This process is called THz Time-Domain Spectroscopy (THz-TDS). The resolution of the mapped THz waveform is limited by the pulse duration of the optical pulse. Figure 2.11 shows an experimental schematic for THz-TDS used in our lab. After the optical-probe pulse passes through the THz-induced birefringent EO detection crystal with (without) the presence of a THz field, the optical polarization becomes slightly elliptical (remains linear). The optical pulse then propagates through a $\lambda/4$ -waveplate which rotates the polar-

ization to nearly circular (circular) and is then split into two isolated paths of orthogonal polarization by a Wollaston prism. The two polarizations are measured independently with a balanced photodiode which measures the difference of the two intensities. In the presence of (without) an incident THz field, the balanced photo-diode signal will be non-zero (zero). By the use of a chopping wheel which blocks every other THz pulse, a comparison of the ultrafast optical-probe pulse polarization is made with versus without a nearly instantaneous point in the THz waveform. The resolution of the temporal measurement is limited by the optical-probe pulse duration. To perform TDS, we then scan the ultrafast optical-probe pulse across the THz waveform to map out the electric field THz waveform in the time-domain.

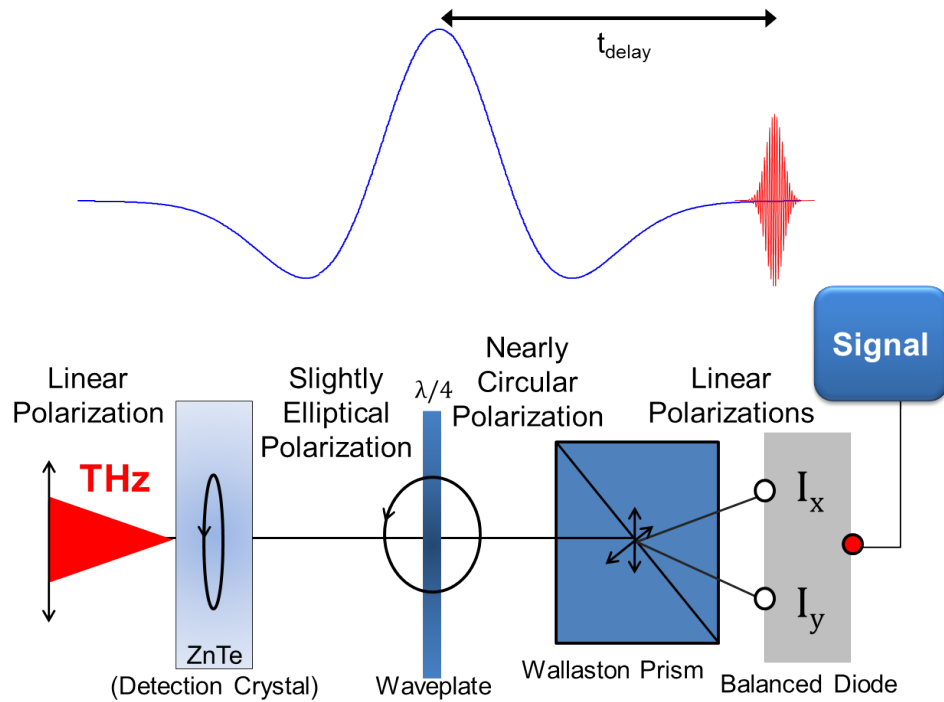


Figure 2.11: The optical pulse is temporally scanned over the THz waveform. The “instantaneous” Electric-field bias of the THz waveform at the moment of t_{delay} induces a birefringence via the Pockels Effect inside the ZnTe detection crystal. The birefringence rotates the polarization of the optical probe pulse which is then measured through a Wollaston prism and balanced photodiode.

The field induced birefringence maximum is when both the THz field and optical polarization are parallel to the $[1\bar{1}0]$ axis. The nonlinear polarization at the optical frequency is orthogonal to the incident optical field. This implies that the linearly polarized optical-probe pulse evolves into an elliptical polarization under the influence of an external field (e.g., THz field). Due to the Pockels effect, by propagating a distance, L , through the birefringent crystal, the optical-probe pulse

picks up a differential phase retardation, $\Delta\phi$,

$$\Delta\phi = (n_y - n_x) \frac{\omega L}{c} = \frac{\omega L}{c} n_{\text{Opt}}^3 d_{14} E_{\text{THz}} \propto E_{\text{THz}} \quad (2.115)$$

The measurable quantity in THz-TDS is the balanced photodiode. The two orthogonal polarization intensities of the optical-probe pulse, I_x and I_y , and their difference, $\Delta I = I_y - I_x$, are

$$I_x = \frac{I_0}{2} (1 - \sin \Delta\phi) \approx \frac{I_0}{2} (1 - \Delta\phi) \quad (2.116)$$

$$I_y = \frac{I_0}{2} (1 + \sin \Delta\phi) \approx \frac{I_0}{2} (1 + \Delta\phi) \quad (2.117)$$

$$\Delta I = I_0 \sin \Delta\phi \approx I_0 \Delta\phi \quad (2.118)$$

It is important to note that the photodiode measures proportional to E_{THz} so long as the field strength is low enough. In terms of THz-TDS, we can scale the photodiode signal, ΔI , with the optical-probe intensity, I_0 . So long as the signal fraction, $\frac{\Delta I}{I_0}$, is small enough ($\Delta\phi < 10^{-1}$ rad), then the small angle approximation can be made (Eq. 2.118),

$$\frac{\omega L}{c} n_{\text{Opt}}^3 d_{14} E_{\text{THz}} < 10^{-1} \text{ rad} \quad (2.119)$$

$$(L = 0.15\text{-mm}) \Rightarrow E_{\text{THz}} < 2.4 \text{ MV/cm} \quad (2.120)$$

In our measurements, we find that the THz-TDS signal noticeably deforms at

field strengths in excess of 200 kV/cm.

2.6 Modeling: Drude-Lorentz for Lossy Dielectrics, Drude-Smith for Conductors, and Drude-Sommerfeld for Free Electrons

In Section 2.2, the harmonic oscillator was used to describe the material properties of a lossy-dielectric system, often called the Drude-Lorentz model. We can draw a relationship between conductivity and electric susceptibility from the dispersion relations of a dielectric (Eq. 2.27) and a conductor (Eq. 2.28). The definition results from the conductor assumption ($\sigma \gg \omega\epsilon$) and applies to all materials,

$$\epsilon_r(\omega) = \frac{i\tilde{\sigma}(\omega)}{\epsilon_0\omega} \quad (2.121)$$

$$\chi_e(\omega) = \frac{i\tilde{\sigma}(\omega)}{\epsilon_0\omega} + 1 \approx \frac{i\tilde{\sigma}(\omega)}{\epsilon_0\omega} \quad (2.122)$$

For purpose of explaining the derivation, it is important to note that $\tilde{n}^2(\omega)$, $\tilde{\epsilon}_r(\omega)$, and $\chi_e(\omega)$ come from the harmonic oscillator model (Section 2.2) while $\tilde{\sigma}(\omega)$ comes from the conductor assumption and Eq. 2.121. For conductors, approximations can be imposed onto the Drude-Lorentz model to form the Drude-Smith model ($\omega_0 = 0$), the Drude model ($\omega_0 = 0$, $\omega\tau \ll 1$), and the Drude-Sommerfeld free electron model ($\omega_0 = 0$, $\gamma = 0$). For a model dependent description of the electric susceptibility, $\chi_e(\omega)$, the conductivity, $\tilde{\sigma}(\omega)$, and the index of refraction, $\tilde{n}^2(\omega)$ refer to Table 2.5.

	$\chi_e(\omega)$	$\tilde{\sigma}(\omega)$	$\tilde{n}^2(\omega), \tilde{\epsilon}_r(\omega)$
Drude-Lorentz Model	$i \frac{Nq^2\tau}{m^*\epsilon_0\omega} \frac{1}{1-i\left(\omega-\frac{\omega_0^2}{\omega}\right)\tau}$	$\frac{Nq^2\tau}{m^*} \frac{1}{1-i\left(\omega-\frac{\omega_0^2}{\omega}\right)\tau}$	$1 + \frac{Nq^2}{m^*\epsilon_0} \frac{1}{\omega_0^2-\omega^2-i\omega\gamma}$
Drude-Smith Model ($\omega_0 = 0$)	$i \frac{Nq^2\tau}{m^*\epsilon_0\omega} \frac{1}{1-i\omega\tau}$	$\frac{Nq^2\tau}{m^*} \frac{1}{1-i\omega\tau}$	$1 - \frac{Nq^2}{m^*\epsilon_0} \frac{1}{\omega^2+i\omega\gamma}$
Drude Model ($\omega_0 = 0,$ $\omega\tau \ll 1$)	$i \frac{Nq^2\tau}{m^*\epsilon_0\omega}$	$\frac{Nq^2\tau}{m^*}$	$1 + i \frac{Nq^2\tau}{m^*\epsilon_0\omega}$
Drude- Sommerfeld Model ($\omega_0 = 0,$ $\gamma = 0$)	$-\frac{Nq^2}{m^*\epsilon_0\omega^2}$	$i \frac{Nq^2}{m^*\omega}$	$1 - \frac{Nq^2}{m^*\epsilon_0} \frac{1}{\omega^2}$

Table 2.5: Electric susceptibility, $\chi_e(\omega)$, conductivity, $\tilde{\sigma}(\omega)$, and index of refraction, $\tilde{n}^2(\omega)$ for modeled materials exhibiting dielectric, lossy dielectric, conductor, and free-electron behavior.

Depending on the model, it is common to choose either the conductivity or electric permittivity to describe the electronic properties of a material. In a metal or semi-metal, conductivity best describes electronic properties (e.g., Drude-Sommerfeld, Drude, Drude-Smith models). In a semiconductor or insulator where the carrier density, n , is low enough ($n < 10^{20}$ for THz measurements), electric permittivity best describes electronic properties (e.g., Drude-Lorentz model).

For a free-electron environment, the Drude-Sommerfeld free-electron model is an accurate descriptor. In this scenario, the relative permittivity simplifies to the

following,

$$\epsilon_r(\omega) = 1 - \frac{\omega_p^2}{\omega^2} \quad (2.123)$$

where $\omega_p = \frac{Nq^2}{m^*\epsilon_0}$ is the plasma frequency.

A more commonly used model for metals is the Drude model. Generally for most metals in the THz regime, electric field transmission is frequency independent and low in magnitude with exponential decay starting at the interface of incidence. The skin depth for common metals is on the order of thin film technology ($\delta \sim 10$ -nm for copper) which is much smaller than the wavelength of THz radiation.

When THz transmission through a metal film is frequency independent, the Drude model is permissible and can be used for determination of electrical conductivity in the DC limit. It is notable that in the Drude model, we calculate the DC conductivity via THz measurements. However, with the Drude-Smith model, we calculate AC THz conductivity. The Drude conductivity can be found in Table 2.5. Drude conductivity can also be represented as dependent on the electron mobility, μ_e , carrier concentration, n , and electron charge, q ,

$$\sigma_{\text{Drude}} = qn\mu_e \quad (2.124)$$

where the electron mobility relates to the scattering time, τ , and effective mass, m^* ,

$$\mu_e = \frac{q\tau}{m^*} \quad (2.125)$$

In the Drude approximation, an electron moves through a lattice with an av-

average drift velocity, v_d , in response to an electric field. The electron mobility describes the electron's ability to move under the influence of the external field,

$$v_d = \mu_e E \quad (2.126)$$

Similar to the relationship between volume current, \mathbf{J} , and electric field, \mathbf{E} , as described by Ohm's law (Eq. 2.13), thin film sheet conductivity (for quasi-two-dimensional structures), σ_s , describes how a surface current, \mathbf{K} , responds linearly to an external field,

$$\mathbf{K}_f = \sigma_s \mathbf{E} \quad (2.127)$$

The relationship between sheet conductivity, σ_s , and volume conductivity, σ , is

$$\sigma_s = \sigma d \quad (2.128)$$

where d is the thickness of the thin film.

The Drude approximation assumes that the electron scattering time is much shorter than the E field oscillation period. In the special case where the scattering time lengthens to be on the order of the oscillation period, we must turn to the Drude-Smith model (refer to Table 2.5), where the conductivity becomes frequency dependent,

$$\sigma_{\text{Drude-Smith}}(\omega) = \frac{\sigma_{\text{Drude}}}{1 - i\omega\tau} \quad (2.129)$$

Regardless of whether the Drude or Drude-Smith approximations are enacted, if the conductivity of the material is high enough ($\sigma \gg \epsilon_0\omega$), we can approximate

the index of refraction from Eq. 2.121:

$$\tilde{n}^2(\omega) = \frac{i\tilde{\sigma}(\omega)}{\epsilon_0\omega} \quad (2.130)$$

Under the condition that the material is lossy but non-metallic, the Drude-Lorentz Model is the broadest theoretical model for a material. In the far from resonant condition, it is possible to describe a material as a lossless dielectric. In this case the index of refraction becomes constant over the frequency range and the material is considered “dispersionless”. This is the case for the THz response of silicon, and this is why silicon is the most common substrate for THz science.

2.7 Fresnel Equations

The law of reflection, the law of refraction (Snell’s law), Huygens’ principle, and Fermat’s principle provide a preliminary understanding of the propagation of light through an interface of two media. This section addresses the interface of two linear, isotropic, homogeneous, non-magnetic, dielectric media. At an interface, electromagnetic waves must maintain phase continuity across the boundary. We utilize Maxwell’s equations to institute boundary conditions. It is important to keep in mind that frequency remains constant across the boundary due to energy conservation, or the time dependent continuity of phase. Spatial continuity must be constituted at the boundary by utilizing time minimization through Fermat’s principle.

Incident fields can be decomposed into two polarizations: perpendicular (s-polarization) and parallel (p-polarization) to the plane of incidence – OR – parallel (s-polarization) and non-parallel (p-polarization) to the interface surface (see Figure 2.12).

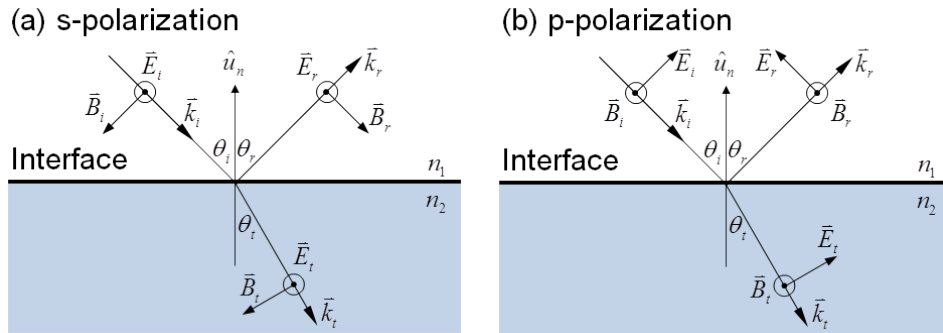


Figure 2.12: (a) s-polarization. (b) p-polarization. An electromagnetic wave incident on an isotropic medium whose \mathbf{E} -field is perpendicular (parallel) to the plane of incidence is considered s-polarized (p-polarized). i , r , and t are indices representing the incident, reflected, and transmitted media, respectively.

For an electromagnetic wave with arbitrary polarization, the following boundary conditions apply to the interface,

$$\mathbf{E}_{i\tau} + \mathbf{E}_{r\tau} = \mathbf{E}_{t\tau} \quad (2.131)$$

$$\mathbf{H}_{i\tau} + \mathbf{H}_{r\tau} = \mathbf{H}_{t\tau} \quad (2.132)$$

where τ represents the field component that is tangential to the interface. i , r , and t are index holders representing the incident, reflected, and transmitted media, respectively.

In the s-polarization scenario, imposing continuity of \mathbf{E}_τ and \mathbf{H}_τ results in the following boundary conditions,

$$E_i + E_r = E_t \quad (2.133)$$

$$-H_i \cos \theta_i + H_r \cos \theta_r = -H_t \cos \theta_t \quad (2.134)$$

where θ_i , θ_r , and θ_t represent the incident, reflected, and transmitted angles at the boundary as shown in Figure 2.12a. We can re-write Eq. 2.134 by using the law of reflection and substituting Eq. 2.25,

$$\frac{n_i}{\mu_i} (E_i - E_r) \cos \theta_i = \frac{n_t}{\mu_t} E_t \cos \theta_t \quad (2.135)$$

By assuming both materials are non-magnetic ($\mu_i, \mu_t \approx \mu_0$) and solving the system of equations: {Eq. 2.133 and Eq. 2.135}, we arrive at the Fresnel equations for s-polarization,

$$r_s = \left(\frac{E_r}{E_i} \right)_s = \frac{n_i \cos \theta_i - n_t \cos \theta_t}{n_i \cos \theta_i + n_t \cos \theta_t} \quad (2.136)$$

$$t_s = \left(\frac{E_t}{E_i} \right)_s = \frac{2n_i \cos \theta_i}{n_i \cos \theta_i + n_t \cos \theta_t} \quad (2.137)$$

Here, the index s denotes s-polarization and r and t represent the reflection and transmission coefficients. Again, the indices i and t represent corresponding media in which incidence and transmission occur.

A similar analysis can be performed for p-polarization (see Figure 2.12b). By

imposing continuity of \mathbf{E}_τ and \mathbf{H}_τ at the boundary,

$$H_i + H_r = H_t \quad (2.138)$$

$$E_i \cos \theta_i - E_r \cos \theta_r = E_t \cos \theta_t \quad (2.139)$$

applying the law of reflection, substituting Eq. 2.25, and solving the system of equations, we obtain the latter two Fresnel equations for p-polarization,

$$r_p = \left(\frac{E_r}{E_i} \right)_p = \frac{n_t \cos \theta_i - n_i \cos \theta_t}{n_t \cos \theta_i + n_i \cos \theta_t} \quad (2.140)$$

$$t_p = \left(\frac{E_t}{E_i} \right)_p = \frac{2n_i \cos \theta_i}{n_t \cos \theta_i + n_i \cos \theta_t} \quad (2.141)$$

These Fresnel equations, for both s- and p-polarization, apply to any arbitrary linear, isotropic, homogeneous, non-magnetic medium. r_p and t_p represent the field fraction or the relative field reflected and transmitted for p-polarization incident light, respectively.

Reflectance, R , is defined as the ratio of the reflected power to the incident power (recall Eq. 2.35),

$$R = \frac{I_r A \cos \theta_r}{I_i A \cos \theta_i} = \frac{cn_r \epsilon_0 E_{0r}^2 \cos \theta_r}{cn_i \epsilon_0 E_{0i}^2 \cos \theta_i} = r_{s,p}^2 \quad (2.142)$$

where the reflectance simplifies because each of the reflected parameters is equal to the incident parameters.

The transmittance, T , is the ratio of the transmitted to the incident irradiance,

$$T = \frac{I_t A \cos \theta_t}{I_i A \cos \theta_i} = \frac{cn_t \epsilon_0 E_{0t}^2 \cos \theta_t}{cn_i \epsilon_0 E_{0i}^2 \cos \theta_i} = \left(\frac{n_t \cos \theta_t}{n_i \cos \theta_i} \right)^2 t_{s,p}^2 \quad (2.143)$$

where the two media are different we see that the transmittance does not simplify. Figure 2.13 shows how the s-polarization and p-polarization reflectance and transmittance changes as a function of incidence angle.

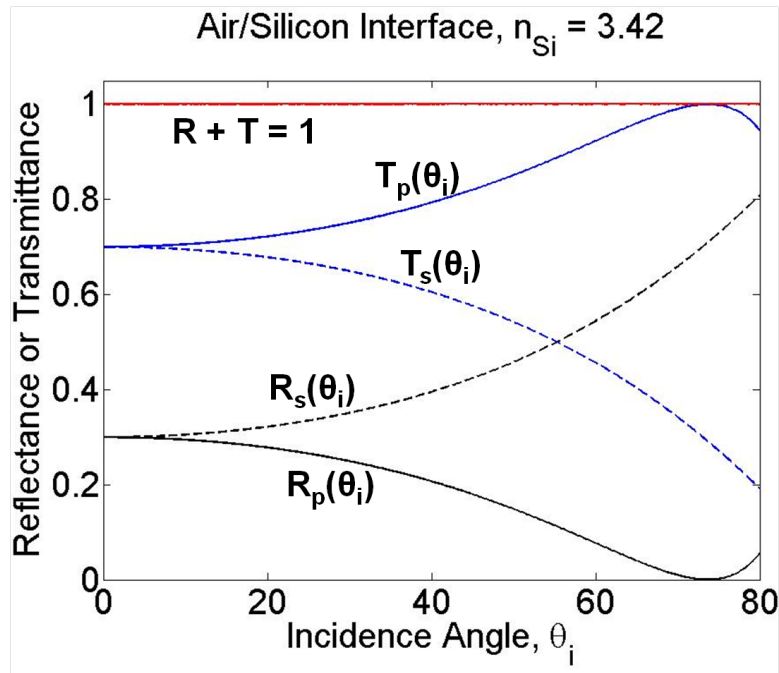


Figure 2.13: Reflectance (black), Transmittance (red), and the sum, $R + T = 1$ (red), for s-polarization (dashed) and p-polarization (solid). T maximizes and R minimizes at Brewster's angle, θ_B .

The total power remains constant,

$$R + T = 1 \quad (2.144)$$

In all power measurements, the following total power relation must hold,

$$R + T + A = 1 \quad (2.145)$$

where A represents the total power absorbed in the material. Absorption can be inferred through the use of Eq. 2.30 when the absorption coefficient, α , is non-negligible.

Within the Fresnel coefficients, there is a special angle of incidence in which only p-polarized light transmits through and s-polarized light reflects off of an interface. Brewster's angle,

$$\theta_B = \tan^{-1} (n_t/n_i) \quad (2.146)$$

has application in our lab to the intra-cavity transmission of the Verdi-Mira system and also in making a 100% efficient interferometer for type-II difference frequency generation in Zinc Telluride.

Another interesting angle of incidence is the critical angle for total internal reflection,

$$\theta_C = \sin^{-1} (n_t/n_i) \quad (2.147)$$

This is the angle for which transmission is zero and all light is reflected under the law of reflection. This process can only occur when $n_t < n_i$.

2.8 Fresnel Equations for Anisotropic Materials

Thus far, the derived Fresnel Equations have been for linear, isotropic, homogeneous, non-magnetic media. Suppose, however, that the material is anisotropic. In this scenario, we broaden the dielectric permittivity into a three-dimensional, first-order dielectric matrix:

$$\epsilon \Rightarrow \hat{\epsilon} = \begin{bmatrix} \epsilon_{xx} & \epsilon_{xy} & \epsilon_{xz} \\ \epsilon_{yx} & \epsilon_{yy} & \epsilon_{yz} \\ \epsilon_{zx} & \epsilon_{zy} & \epsilon_{zz} \end{bmatrix} \quad (2.148)$$

This is the generalized dielectric tensor for a linear anisotropic medium. ϵ_{ij} represents how the linear material polarization in the i -direction responds to an incident field polarization in the j -direction. For a single incident field angle with respect to an anisotropic material orientation, the anisotropic linear material polarization can have arbitrary direction. This means that the medium has a polarization response that is not the same in all directions. It is even possible to have a polarization response in an orthogonal direction to the applied electric field (off-diagonal matrix elements). For convenience, we will assume that the dielectric material can be rotated such that all off-diagonal matrix elements become zero, meaning that the material response is orthogonal,

$$\epsilon = \begin{bmatrix} \epsilon_x & 0 & 0 \\ 0 & \epsilon_y & 0 \\ 0 & 0 & \epsilon_z \end{bmatrix} \quad (2.149)$$

For all intents and purposes, we will use this as our general dielectric tensor.

Anisotropic materials can be classified into two types:

$$\epsilon_z \neq \epsilon_y \neq \epsilon_x \quad (\text{biaxial}) \quad (2.150)$$

$$\epsilon_z \neq \epsilon_y = \epsilon_x \quad (\text{uniaxial}) \quad (2.151)$$

In the special case where the permittivity in all three directions are equal, the material is considered “isotropic” and the permittivity tensor simplifies to the dielectric constant (See Sec. 2.7). For simplicity, in this section we will ignore biaxial properties since they do not apply to any of the projects in this thesis. A quality in depth review of anisotropic optical materials can be found in Fujiwara 2007.

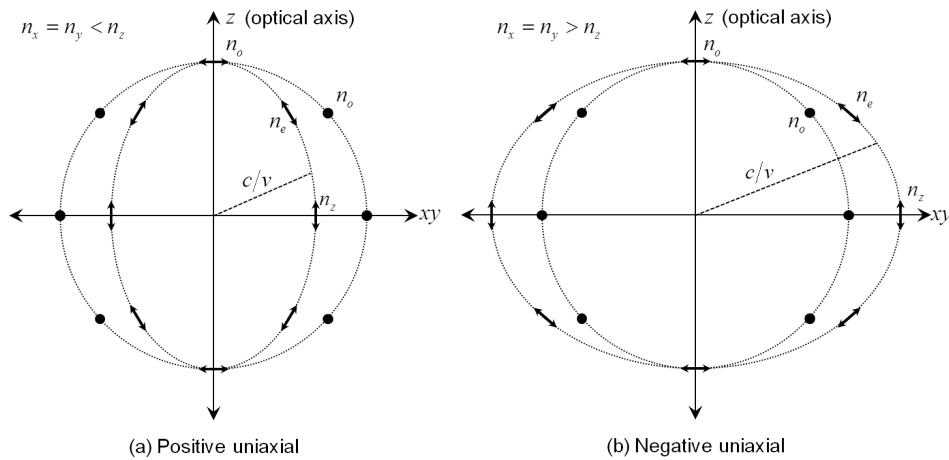


Figure 2.14: (a) Positive uniaxial ($n_x = n_y < n_z$). (b) Negative uniaxial ($n_x = n_y > n_z$). Index ellipsoids of anisotropic media show the speed of light depending on direction of propagation (z-axis versus xy-plane).

Figure 2.14 is a two-dimensional description of the speed of light propagating in a uniaxial medium. In three dimensions, the picture is rotationally symmetric about the z -axis. In uniaxial materials, the speed of light depends on \mathbf{E} field polarization direction. The z -axis defines the optical axis. When the z -index, n_z is greater (less) than the xy -index ($n_x = n_y$), the material is considered to be negative (positive) uniaxial as shown in Figure 2.14a (Figure 2.14b). At a polarization perpendicular to the optical axis, light propagates as an ordinary ray with index of refraction corresponding to the xy -plane, $n_o = n_x = n_y$. When the \mathbf{E} field polarization has any components parallel to the optical axis, light propagates as an extraordinary ray where its speed depends on the angle in which it propagates,

$$\frac{1}{n_e^2} = \frac{\cos^2 \theta_e}{n_o^2} + \frac{\sin^2 \theta_e}{n_z^2} \quad (2.152)$$

The extraordinary angle, θ_e , is measured with respect to the optical axis. The extraordinary index of refraction is not constant, unlike the ordinary index. It varies with θ_e , transitioning between being equivalent to n_o (n_e) when the polarization is along the xy -plane (z -axis). Within this transition, n_e follows an elliptical functional form from n_o to n_e .

There are many practical applications to uniaxial materials. Two common uses in our lab are waveplates and Wollaston prisms. This section is dedicated to deriving the uniaxial Fresnel equations, which is when light propagates across a boundary consisting to one isotropic medium and one uniaxial medium. For any incident polarization, the law of refraction through Fermat's principle applies to

any interface,

$$n_e \sin \theta_e = n_o \sin \theta_o = n_1 \sin \theta_1 \quad (2.153)$$

Our objective is to understand how light propagates through an anisotropic medium. Consider an experimental sample containing four layers of media. Media (1-air), (3-substrate), and (4-air) are isotropic and medium (2-sample) is uniaxial as shown in Figure 2.15.

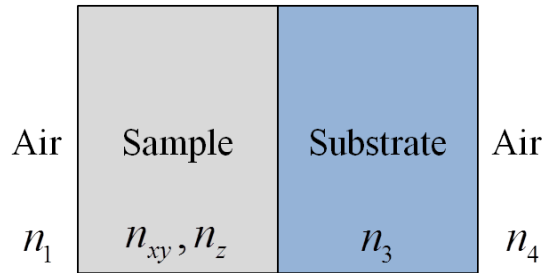


Figure 2.15: Sample structure for measuring transmission through an anisotropic sample-on-substrate.

To begin, let's consider light propagating from the isotropic medium (1-air) into the anisotropic medium (2-sample). We can re-write an expression for the extraordinary index of refraction to be solely dependent on the incidence angle using Snell's Law,

$$n_e^2 = n_o^2 + n_1^2 \sin^2 \theta_1 \left(1 - \frac{n_o^2}{n_z^2} \right) \quad (2.154)$$

Regardless of polarization, continuity across the boundary must satisfy the

following relations,

$$\mathbf{E}_{i\tau} + \mathbf{E}_{r\tau} = \mathbf{E}_{t\tau} \quad (2.155)$$

$$\mathbf{D}_{in} + \mathbf{D}_{rn} = \mathbf{D}_{tn} \quad (2.156)$$

$$\mathbf{H}_{i\tau} + \mathbf{H}_{r\tau} = \mathbf{H}_{t\tau} \quad (2.157)$$

$$\mathbf{B}_{in} + \mathbf{B}_{rn} = \mathbf{B}_{tn} \quad (2.158)$$

where τ and n represent the tangential and normal components of the fields relative to the interface plane and $\{i, r, t\}$ represent the incident, reflected, and transmitted waves.

We will decompose the two polarizations at the interface. In comparison to isotropic media, two drastic differences occur in the way light propagates. For starters, in the p-polarization scenario, the pointing vector ($\mathbf{S} = \mathbf{E} \times \mathbf{H}$) and the wave vector ($\mathbf{k} = \mathbf{D} \times \mathbf{H}$) drift from co-linearity as shown in Figure 2.16b. The displacement and auxillary field directions satisfy Maxwell's equations while the electric and magnetic field directions satisfy Poynting's relation. Another tantalizing effect is that the extraordinary material steers p-polarization based on a varying index of refraction. This effect may seem abnormal, but in the presence of an anisotropic material becomes quotidian and contains fundamental implications of phase retarding and spatial separation, and prescribe commonplace applications in our lab.

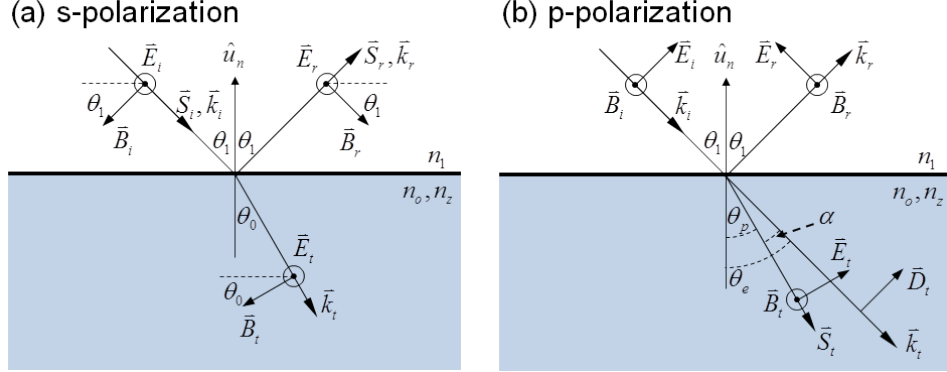


Figure 2.16: (a) S-polarization. (b) P-polarization. An electromagnetic wave incident on an anisotropic medium from an isotropic medium. When the \mathbf{E} -field is polarized parallel to the plane of incidence (s-pol), the \mathbf{S} - and \mathbf{k} -vectors propagate co-linearly. When the \mathbf{E} -field is polarized perpendicular to the plane of incidence (p-pol), the \mathbf{S} - and \mathbf{k} -vectors propagate in different directions satisfying Maxwell's equations (Eq. 2.24) and Poynting's relation (Eq. 2.33)

In the s-polarization scenario, we utilize the \mathbf{E}_τ , \mathbf{B}_n , and \mathbf{H}_τ boundary conditions,

$$E_i + E_r = E_t \quad (2.159)$$

$$(E_i + E_r) n_1 \sin \theta_1 = E_t n_{2x} \sin \theta_o \quad (2.160)$$

$$(E_i - E_r) n_1 \cos \theta_1 = E_t n_{2x} \cos \theta_o \quad (2.161)$$

where θ_1 is the incidence angle and θ_o is the ordinary transmission angle. Combining Eq. 2.159 and Eq. 2.160 gives a form of Snell's Law. Combining Eq. 2.159 and Eq. 2.161 gives the s-polarization reflection and transmission coefficients for

an \mathbf{E} field incident upon an anisotropic medium from an isotropic medium,

$$r_{12}^s = \frac{n_1 \cos \theta_1 - n_{2x} \cos \theta_o}{n_1 \cos \theta_1 + n_{2x} \cos \theta_o} \quad (2.162)$$

$$t_{12}^s = \frac{2n_1 \cos \theta_1}{n_1 \cos \theta_1 + n_{2x} \cos \theta_o} \quad (2.163)$$

If we reverse the direction of propagation so that the radiation is incident upon an isotropic medium from an anisotropic medium, we can simply reverse the parameters,

$$r_{23}^s = \frac{n_{2x} \cos \theta_o - n_3 \cos \theta_3}{n_{2x} \cos \theta_o + n_3 \cos \theta_3} \quad (2.164)$$

$$t_{23}^s = \frac{2n_{2x} \cos \theta_o}{n_{2x} \cos \theta_o + n_3 \cos \theta_3} \quad (2.165)$$

The p-polarization scenario is much more complex (shown in Figure 2.16b). We start by employing the \mathbf{E}_τ and \mathbf{H}_τ boundary conditions,

$$(E_i - E_r) \cos \theta_1 = E_t \cos \theta_p \quad (2.166)$$

$$H_i + H_r = H_t \quad (2.167)$$

where θ_p is the transmission angle of the \mathbf{D} field. Recall that θ_e is the transmission angle of the \mathbf{E} field. There is a splitting between propagation directions of \mathbf{D} and \mathbf{E} for p-polarization. In p-polarization, \mathbf{D} and \mathbf{E} split mathematically due to the non-equal diagonal elements of the dielectric matrix ($\epsilon_z \neq \epsilon_x = \epsilon_y$). Meanwhile,

in s-polarization, \mathbf{D} and \mathbf{E} remain co-linear due to the equal diagonal elements ($\epsilon_x = \epsilon_y$). Both θ_e and θ_p are not equal to the s-polarization propagation direction, θ_0 , by Snell's law. This effect is sometimes called birefringence and it can be used to separate orthogonal polarizations in the application of a Wollaston prism. In order to convert the \mathbf{H}_τ boundary condition into an \mathbf{E} representation, we must look at Eq. 2.25. There is a problem for anisotropic p-polarization that did not arise in the isotropic Fresnel derivations. In the anisotropic scenario, \mathbf{k} and \mathbf{E} are not orthogonal, there is an angle, $(90^\circ - \alpha)$, between them. This corresponds to an angle $(\alpha = \theta_e - \theta_p)$ between \mathbf{E} and \mathbf{D} . The relation between \mathbf{E} and \mathbf{H} is now,

$$kE \cos \alpha = \omega \mu_0 H \quad (2.168)$$

If we apply this relation to Eq. 2.167, we can simplify,

$$(E_i + E_r) n_1 = E_t n_e \cos \theta_e - \theta_p \quad (2.169)$$

If we combine Eqs. 2.166 and eq:anisotropic continuity ppol 3, we arrive at the p-polarization reflection and transmission coefficients for an \mathbf{E} field incident upon an anisotropic medium from an isotropic medium,

$$r_{12}^p = \frac{n_e \cos(\theta_e - \theta_p) \cos \theta_1 - n_1 \cos \theta_p}{n_e \cos(\theta_e - \theta_p) \cos \theta_1 + n_1 \cos \theta_p} \quad (2.170)$$

$$t_{12}^p = \frac{2n_1 \cos \theta_1}{n_e \cos(\theta_e - \theta_p) \cos \theta_1 - n_1 \cos \theta_p} \quad (2.171)$$

These representations of r and t are entangled with n_e , θ_e , and θ_p . We can dissociate these parameters and re-write the Fresnel equations in terms of intrinsic parameters ($\{n_1, n_3, n_0, n_z, \theta_1, \theta_3\}$) if we can find expressions for $n_e \cos(\theta_e - \theta_p)$ and $\cos \theta_p$. We can start by utilizing our understanding of \mathbf{D} and \mathbf{E} fields to create a system of equations,

$$D_z = \epsilon_z E_z \quad \Rightarrow \quad |\mathbf{D}| \sin \theta_e = \epsilon_z |\mathbf{E}| \sin \theta_p \quad (2.172)$$

$$D_x = \epsilon_x E_x \quad \Rightarrow \quad |\mathbf{D}| \cos \theta_e = \epsilon_x |\mathbf{E}| \cos \theta_p \quad (2.173)$$

and solve to draw a relationship between θ_e and θ_p ,

$$\tan \theta_e = \frac{n_z^2}{n_o^2} \tan \theta_p \quad (2.174)$$

One can create an expression for the incomplete term, $\cos \theta_p$, solely as a function of intrinsic parameters by using Eq. 2.174, Snell's law (Eq. 2.153), and the

extraordinary index of refraction (Eq. 2.152),

$$\cos^2 \theta_p = \cos^2 \left(\tan^{-1} \left(\frac{n_o^2}{n_z^2} \tan^{-1} \theta_e \right) \right) \quad (2.175)$$

$$= \left(\frac{n_o^4}{n_z^4} \tan^2 \theta_e + 1 \right)^{-1} \quad (2.176)$$

$$= \frac{n_z^4 (1 - \sin^2 \theta_e)}{n_z^4 (1 - \sin^2 \theta_e) + n_o^4 \sin^2 \theta_e} \quad (2.177)$$

$$= \frac{n_z^4 (n_e^2 - n_1^2 \sin^2 \theta_1)}{n_z^4 (n_e^2 - n_1^2 \sin^2 \theta_1) + n_o^4 n_1^2 \sin^2 \theta_1} \quad (2.178)$$

$$= \frac{n_z^2 (n_z^2 - n_1^2 \sin^2 \theta_1)}{n_z^4 + n_1^2 (n_o^2 - n_z^2) \sin^2 \theta_1} \quad (2.179)$$

$$\cos \theta_p = n_z \sqrt{\frac{n_z^2 - n_1^2 \sin^2 \theta_1}{n_z^4 + n_1^2 (n_o^2 - n_z^2) \sin^2 \theta_1}} \quad (2.180)$$

Next, one can create an expression for the incomplete term, $n_e \cos(\theta_e - \theta_p)$, solely as a function of intrinsic parameters by using Snell's law (Eq. 2.153), and

the extraordinary index of refraction (Eq. 2.152),

$$n_e^2 \cos^2 (\theta_e - \theta_p) = n_e^2 \cos^2 \theta_e \cos^2 \theta_e (1 + \tan \theta_e \tan \theta_p)^2 \quad (2.181)$$

$$= \frac{n_e^2}{n_z^4 (1 - \sin^2 \theta_e)} (n_z^2 \cos^2 \theta_e + n_o^2 \sin^2 \theta_e)^2 \cos^2 \theta_p \quad (2.182)$$

$$= \frac{[n_z^2 (n_e^2 - n_1^2 \sin^2 \theta_1) + n_o^2 n_1^2 \sin^2 \theta_1]^2}{n_z^4 (n_e^2 - n_1^2 \sin^2 \theta_1)} \cos^2 \theta_p \quad (2.183)$$

$$= \frac{n_z^2 n_o^2}{n_z^2 - n_1^2 \sin^2 \theta_1} \cos^2 \theta_p \quad (2.184)$$

$$(2.185)$$

and our new representation of $\cos \theta_p$, Eq. 2.180,

$$n_e \cos (\theta_e - \theta_p) = \frac{n_z^2 n_o}{\sqrt{n_z^4 + n_1^2 (n_o^2 - n_z^2) \sin^2 \theta_1}} \quad (2.186)$$

Combining our new representations of $\cos \theta_p$ (Eq. 2.180) and $n_e \cos (\theta_e - \theta_p)$ (Eq. 2.186) with the extrinsic Fresnel equations (Eqs. 2.170 and 2.171) gives us the p-polarization Fresnel equations for an anisotropic material:

$$r_{12}^p = \frac{n_z n_o \cos \theta_1 - n_1 \sqrt{n_z^2 - n_1^2 \sin^2 \theta_1}}{n_z n_o \cos \theta_1 + n_1 \sqrt{n_z^2 - n_1^2 \sin^2 \theta_1}} \quad (2.187)$$

$$t_{12}^p = \frac{2n_1 \cos \theta_1 \sqrt{n_z^4 + n_1^2 (n_o^2 - n_z^2) \sin^2 \theta_1}}{n_z [n_z n_o \cos \theta_1 + n_1 \sqrt{n_z^2 - n_1^2 \sin^2 \theta_1}]} \quad (2.188)$$

Similar to the s-polarization scenario, if the radiation propagates through the

anisotropic medium into an isotropic medium, we can simply reverse the parameters (from Eqs. 2.170 and 2.171):

$$r_{23}^p = \frac{n_3 \cos \theta_p - n_e \cos (\theta_e - \theta_p) \cos \theta_3}{n_3 \cos \theta_p + n_e \cos (\theta_e - \theta_p) \cos \theta_3} \quad (2.189)$$

$$t_{23}^p = \frac{2n_e \cos (\theta_e - \theta_p) \cos \theta_p}{n_3 \cos \theta_p + n_e \cos (\theta_e - \theta_p) \cos \theta_3} \quad (2.190)$$

These Fresnel equations can be re-written solely as a function of intrinsic parameters by substituting Eq. 2.180 and Eq. 2.186:

$$r_{23}^p = \frac{n_3 \sqrt{n_z^2 - n_1^2 \sin^2 \theta_1} - n_z n_o \cos \theta_3}{n_3 \sqrt{n_z^2 - n_1^2 \sin^2 \theta_1} + n_z n_o \cos \theta_3} \quad (2.191)$$

$$t_{23}^p = \frac{2n_z^2 n_o}{n_3 \sqrt{n_z^2 - n_1^2 \sin^2 \theta_1} + n_z n_o \cos \theta_3} \sqrt{\frac{n_z^2 - n_1^2 \sin^2 \theta_1}{n_z^4 + n_1^2 (n_o^2 - n_z^2) \sin^2 \theta_1}} \quad (2.192)$$

where $\cos \theta_3$ obeys Snell's law.

2.9 Thin Film Fresnel Formula

In a Drude conductivity approximation, we have the ability to transform our thin-film Fresnel formula into metal representation. We will assume the materials are isotropic and homogeneous and assume normal incidence. An example of a material system which will be thoroughly covered in this thesis is graphene-on-silicon. In our THz measurements, we use high-resistivity Si as a substrate for our samples due to its extremely non-dispersive ($\Delta n \cong 0.00003$) and non-absorptive

($0.005 \leq \alpha \leq 0.02 \text{ cm}^{-1}$) properties over our broad THz spectral range (0.4-1.6 THz). [9, 10] Graphene is a one-atom thick metal layer and silicon is a thick substrate ($\ell = 500\text{-}\mu\text{m}$). Figure 2.17 shows how radiation propagates and internally reflects off of a sample made of a metallic thin-film on a thick substrate.

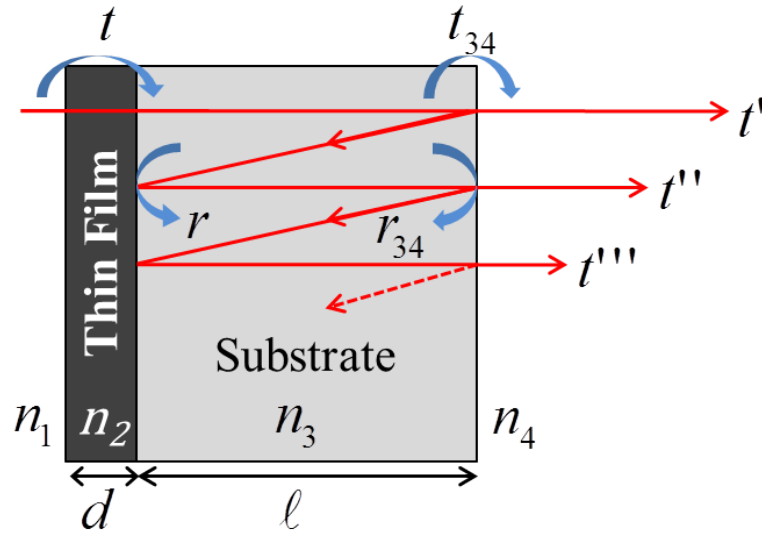


Figure 2.17: The red line depicts the propagation of an electromagnetic wave through metal-on-substrate. The thickness of the metal thin-film is much smaller than the wavelength of light ($d \ll \lambda$) such that we treat the entire transmission through and reflection off of the thin film as a non-interfering, wholistic waveform. Then, each internal reflection within the substrate compiles power fractions, t_{ij} and r_{ij} , based on index of refraction, n_i , and phase, ϕ_{sub} , acquired over the length of the sample, ℓ .

In this section, I will describe the propagation of light through a thin film. The thin film must be “optically-thin” which means that the thickness must be much smaller than the wavelength of light ($nd < \lambda/10 \approx 30\text{-}\mu\text{m}$) so that the internal reflections do not destructively interfere. Akin to an optically-thin sample, the

substrate must be “optically-thick” such that internal reflections are temporally separated into a “pulse train” to both avoid destructive interference and allow for a sufficient pulse tail for experimental and spectroscopic reasons ($nl > 3\lambda \approx 1\text{-}mm$). For these reasons, the radiation passing through the thin film in Figure 2.17 is treated as a whole ray passing through the thin film because the internal reflections collectively add without interference and negligible phase is accrued with each reflection. Then internal reflections in the substrate are treated separately and a substantial phase is accrued with each reflection. To begin with this analysis, we will start with the thin-film transmission and reflection coefficients by collectively adding internal reflections within the thin-film. Generally, normal incidence Fresnel equations and phase hold the relations:

$$r_{ij} = \frac{n_i - n_j}{n_i + n_j} \quad \phi_d = \frac{\omega dn_2}{c} = 2\pi \frac{dn_2}{\lambda} \quad (2.193)$$

$$t_{ij} = \frac{2n_i}{n_i + n_j} \quad \phi_s = \frac{\omega \ell n_3}{c} = 2\pi \frac{dn_3}{\lambda} \quad (2.194)$$

where $j = i + 1$ and ϕ represents the phase change over the propagation through a medium. To collectively add all of the rays through the thin film, take a look at Figure 2.18.

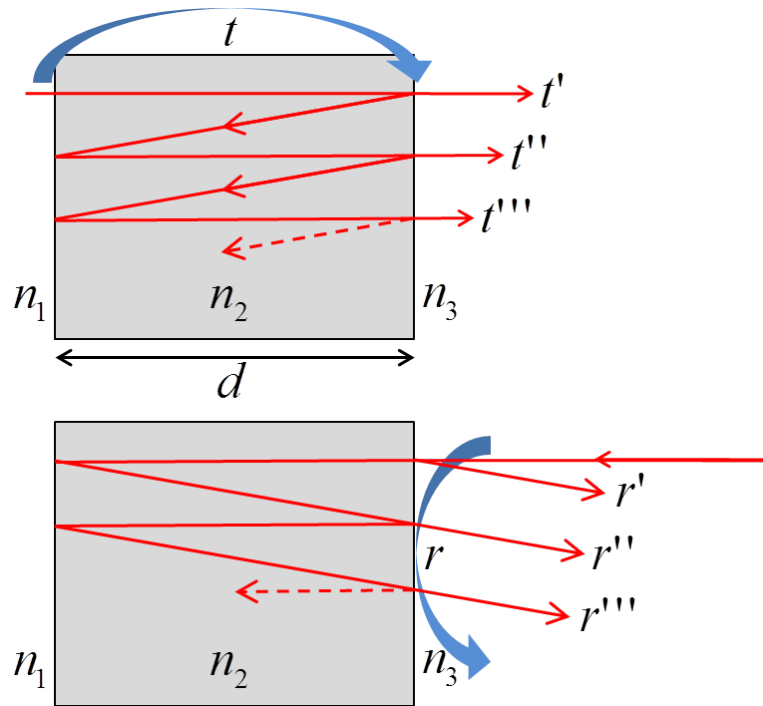


Figure 2.18: Thin film transmission and reflection ray traces. All waves add non-destructively due to thin-film thickness ($d < \frac{\lambda}{10}$)

A critical feature of thin film reflection and transmission is that each electromagnetic wave sums and diminishes through repetition well before the wavelength of the light such that no destructive interference takes place ($d \ll \lambda$). Usually, thicknesses on the order of $\lambda/10$ is sufficient to ensure that thin film treatment is maintained. By strictly looking at the thin film in Figure 2.18 we can see how the rays collectively add. A total transmission coefficient is formulated by summing

each transmission component, t^n ,

$$t = t' + t'' + t''' + \dots \quad (2.195)$$

$$= t_{12}t_{23}e^{i\phi_d} + t_{12}r_{23}r_{21}t_{23}e^{3i\phi_d} + t_{12}r_{23}r_{21}r_{23}r_{21}t_{23}e^{5i\phi_d} + \dots \quad (2.196)$$

$$= t_{12}t_{23}e^{i\phi_d} (1 + r_{23}r_{21}e^{2i\phi_d} + r_{23}^2r_{21}^2e^{4i\phi_d} + \dots) \quad (2.197)$$

$$= t_{12}t_{23}e^{i\phi_d} \sum_{n=0}^{\infty} (r_{23}r_{21}e^{2i\phi_d})^n \quad (2.198)$$

By applying a geometric series, for $|x| \leq 1$,

$$\sum_{n=0}^{\infty} x^n = \frac{1}{1-x} \quad (2.199)$$

we arrive at,

$$t = \frac{t_{12}t_{23}e^{i\phi_d}}{1 + r_{23}r_{12}e^{2i\phi_d}} \quad (2.200)$$

If we apply the thin film approximations,

$$d \ll \lambda \quad (2.201)$$

$$\phi_d \ll 1 \quad (2.202)$$

$$e^{i\phi_d} \approx 1 + i\phi_d \quad (2.203)$$

we can simplify further,

$$t = \frac{4n_1n_2}{(n_1 + n_2)(n_2 + n_3)e^{-i\phi_d} + (n_1 - n_2)(n_2 - n_3)e^{i\phi_d}} \quad (2.204)$$

$$= \frac{2n_1n_2}{(n_1n_2 + n_2n_3) - (n_1n_3 + n_2^2)i\phi_d} \quad (2.205)$$

$$= \frac{t_{13}(n_1 + n_3)}{n_1 + n_3 - n_2 \left(1 + \frac{n_1n_3}{n_2^2}\right) i\phi_d} \quad (2.206)$$

For a metal thin-film, we can make the following approximations,

$$\frac{n_1n_3}{n_2^2} \ll 1 \quad (2.207)$$

$$n_2 \gg (n_3 - n_1) \gg \frac{n_1n_3}{n_2} \quad (2.208)$$

This approximation along with the index of refraction-conductivity relation (Eq. 2.121) allows us to make the following simplification:

$$in_2\phi_d = 2\pi i \frac{d}{\lambda} n_2^2 = -Z_0\sigma d \quad (2.209)$$

where $Z_0 = \frac{1}{\epsilon_0} \approx 376.7 \Omega$ is the impedance of free space. When the relation $\frac{dn_2}{\lambda}$ is small enough such that the thin film is a dielectric ($\phi_d \approx 0$), transmission reaches unity ($t = 1$). However, for a metal thin-film, the metal thin-film approximation (Eq. 2.207) begins to dominate the denominator of the thin-film transmission coefficient (Eq. 2.206) while the small angle approximation ($\phi_d \ll 1$) continues to hold for thin enough films and the transmission coefficient simplifies to the

following:

$$t = \frac{t_{13}(n_1 + n_3)}{n_1 + n_3 + Z_0\sigma_s} \quad (2.210)$$

where σ_s represents the sheet conductivity of the metal thin-film ($\sigma_s = \sigma d$). In the event that the substrate is air (i.e., the thin film is suspended over air, $n_1 = n_3 = t_{13} = 1$), then the transmission coefficient simplifies:

$$t = \frac{2}{2 + Z_0\sigma_s} \quad (2.211)$$

A pulse that is transmitted through the thin film is then internally reflected within the substrate, this involves a collective thin-film reflection from the third medium as seen in Figure 2.18:

$$r = r' + r'' + r''' + \dots \quad (2.212)$$

$$= r_{32} + t_{32}r_{21}t_{23}e^{2i\phi_d} + t_{32}r_{21}r_{23}r_{21}t_{23}e^{4i\phi_d} + t_{32}r_{21}r_{23}r_{21}r_{23}r_{21}t_{23}e^{6i\phi_d} + \dots \quad (2.213)$$

$$= r_{32} + t_{32}r_{21}t_{23}e^{2i\phi_d} (1 + r_{23}r_{21}e^{2i\phi_d} + r_{23}^2r_{21}^2e^{4i\phi_d} + \dots) \quad (2.214)$$

$$= r_{32} + t_{32}r_{21}t_{23}e^{2i\phi_d} \sum_{n=0}^{\infty} (r_{23}r_{21}e^{2i\phi_d})^n \quad (2.215)$$

applying the geometric series (Eq. 2.199) we arrive at,

$$r = \frac{r_{32} + r_{21}e^{2i\phi_d}}{1 + r_{21}r_{32}e^{2i\phi_d}} \quad (2.216)$$

If we apply the thin film approximations, we can simplify further:

$$r = \frac{(n_3 - n_2)(n_2 + n_1) + (n_2 - n_1)(n_3 + n_2)(1 + 2i\phi_d)}{(n_3 + n_2)(n_2 + n_1) + (n_2 - n_1)(n_3 - n_2)(1 + 2i\phi_d)} \quad (2.217)$$

$$= \frac{n_3 - n_1 + (n_2 + (n_3 - n_1) - n_1 n_3 / n_2) i \phi_d}{n_3 + n_1 + (-n_2 + (n_3 - n_1) - n_1 n_3 / n_2) i \phi_d} \quad (2.218)$$

If we apply the same set of approximations for the thin-film reflection coefficient as we did for the thin-film transmission coefficient (Eqs. 2.121 and 2.208 lead to the substitution of Eq. 2.209), we can simplify,

$$r = \frac{n_3 - n_1 - Z_0 \sigma_s}{n_3 + n_1 + Z_0 \sigma_s} \quad (2.219)$$

In order to address the multiple internal reflections within the substrate, we must acknowledge that the substrate is thick enough to temporally separate the pulses to create a pulse train ($n\ell > 3\lambda$). The pulses will not interfere and we can therefore look at each pulse individually, where spectral magnitude and phase are the descriptors of the radiation. To begin, refer to Figure 2.17. There are two scenarios experimentally: (1) with the thin-film and (2) without the thin-film (i.e., bare-substrate). In both cases, since the pulses are temporally separated, the waveforms don't need to be summed. Experimentally, we individually observe the spectroscopic waveforms through THz-TDS. However, our experimental power meters only observe the total pulse train. Here is a relative field description of

each pulse in the pulse train for samples with the thin film,

$$t = t' + t'' + t''' + \dots \quad (2.220)$$

$$t_{\text{with}} = tt_{34} + tr_{34}rt_{34} + tr_{34}rr_{34}rt_{34} + \dots \quad (2.221)$$

$$t_{\text{without}} = t_{13}t_{34} + t_{13}r_{34}r_{31}t_{34} + t_{13}r_{34}r_{31}r_{34}r_{31}t_{34} + \dots \quad (2.222)$$

The difference is the thin-film interface ($t \Leftrightarrow t_{13}$) and ($r \Leftrightarrow r_{31}$) are interchangeable. Recall that t and r are the thin-film Fresnel equations and they contain the information of the thin-film properties. These equations represent the magnitude and phase of the transmitted \mathbf{E} fields. If we wanted to look at the intensity, I , via Eq. 2.35, we must norm-square each term,

$$T = |t'|^2 + |t''|^2 + |t'''|^2 + \dots \quad (2.223)$$

$$T_{\text{with}} = t^2t_{34}^2 + t^2r_{34}^2r_{31}^2t_{34}^2 + t^2r_{34}^2r_{31}^2r_{34}^2r_{31}^2t_{34}^2 + \dots \quad (2.224)$$

$$T_{\text{with}} = \frac{t^2t_{34}^2}{1 - r^2r_{34}^2} \quad (2.225)$$

$$T_{\text{without}} = t_{13}^2t_{34}^2 + t_{13}^2r_{34}^2r_{31}^2t_{34}^2 + t_{13}^2r_{34}^2r_{31}^2r_{34}^2r_{31}^2t_{34}^2 + \dots \quad (2.226)$$

$$T_{\text{without}} = \frac{t_{13}^2t_{34}^2}{1 - r_{31}^2r_{34}^2} \quad (2.227)$$

The T_{without} intensity formulae have no dependence on the thin film properties. We can look at the ratio of T_{with} and T_{without} to experimentally determine the thin

film properties:

$$R = \frac{T_{\text{with}}}{T_{\text{without}}} = \frac{t^2 (1 - r_{31}^2 r_{34}^2)}{t_{34}^2 (1 - r^2 r_{34}^2)} \quad (2.228)$$

R represents the relative power transmission. In terms of conductivity, σ_s , we can re-write this formula in two ways:

$$\sigma_s = -\frac{1}{2n_4 Z_0} \left[n_3^2 + 2n_1 n_4 + n_4^2 + \sqrt{\frac{R n_3^4 + 2n_3^2 n_4 (2n_1 + (2-R)n_4) + n_4^2 (4n_1^2 + 4n_1 n_4 + R n_4^2)}{R}} \right] \quad (2.229)$$

2.10 From Fresnel to Fraunhofer Optics

Monochromatic, plane waves, \mathbf{E} and \mathbf{H} , propagate based on the Helmholtz equation (Eq. 2.26). We can represent the electric field propagation in terms of position and momentum space based on Fourier optics,

$$\mathbf{E}(x, y, z) = \iint_{-\infty}^{+\infty} \hat{\mathbf{E}}(k_x, k_y; z) e^{i(k_x x + k_y y)} dk_x dk_y \quad (2.230)$$

$$\hat{\mathbf{E}}(k_x, k_y; z) = \frac{1}{4\pi^2} \iint_{-\infty}^{+\infty} \mathbf{E}(x, y, z) e^{-i(k_x x + k_y y)} dx dy \quad (2.231)$$

If we substitute $\mathbf{E}(x, y, z)$ into the Helmholtz equation (Eq. 2.26) we obtain,

$$\iint_{-\infty}^{+\infty} dk_x dk_y \left[\frac{\partial^2}{\partial z^2} \hat{\mathbf{E}} - (k_x^2 + k_y^2) \hat{\mathbf{E}} + k^2 \hat{\mathbf{E}} \right] e^{i(k_x x + k_y y)} = 0 \quad (2.232)$$

which implies the following relation,

$$\frac{\partial^2}{\partial z^2} \hat{\mathbf{E}} + k_z^2 \hat{\mathbf{E}} = 0 \quad (2.233)$$

The general solution for this differential equation is the wave propagation representation,

$$\hat{\mathbf{E}}(k_x, k_y; z) = \hat{\mathbf{E}}(k_x, k_y; 0) e^{ik_z z} \quad (2.234)$$

If we take the wave propagation representation and substitute back into the Fourier spatial representation, $\mathbf{E}(x, y, z)$ (Eq. 2.230), we obtain the angular spectrum representation, which describes the dispersion of an \mathbf{E} field as it propagates spatially,

$$\mathbf{E}(x, y, z) = \iint_{-\infty}^{+\infty} \hat{\mathbf{E}}(k_x, k_y; 0) e^{i(k_x x + k_y y \pm k_z z)} dk_x dk_y \quad (2.235)$$

where the wave vector components can be described by pythagorus,

$$k_z = \pm \sqrt{k^2 - k_x^2 - k_y^2} \quad (2.236)$$

and the k_z term can either symbolize a plane wave or an evanescent wave,

$$k^2 \geq k_x^2 + k_y^2 \quad (\text{plane waves}) \quad (2.237)$$

$$k^2 \leq k_x^2 + k_y^2 \quad (\text{evanescent waves}) \quad (2.238)$$

For large z , when the image plane is far from the object ($z \gg \lambda$), evanescent waves dissipate leaving plane waves and hence, higher frequency components. This is called the “far-field” or the Fraunhofer regime. Outside of the Fraunhofer regime is considered the Fresnel regime (as $z \sim \lambda$). For small z ($z \ll \lambda$), the image plane is considered to be in the “near-field”. In the near-field region, evanescent waves increase the bandwidth of spatial frequencies by retaining the low frequency components.

2.11 Paraxial Approximation

If we assume the propagation of light to be mostly in the z -direction (i.e., very small divergence), we can apply the paraxial approximation to the wave vector, k_z . The paraxial approximation follows a first-order Taylor series approximation,

$$k_z = \pm \sqrt{k^2 - k_x^2 - k_y^2} \approx k - \frac{k_x^2 + k_y^2}{2k} \quad (2.239)$$

We can apply this approximation to the propagation of a weakly focused Gaussian beam. First, start with a generalized expression for a Gaussian spatial distribution,

$$\mathbf{E}(x, y, 0) = \mathbf{E}_0 e^{-\frac{x^2 + y^2}{\omega_0^2}} \quad (2.240)$$

where ω_0 is the minimum beam waist of a focused Gaussian beam. The Fourier spectrum at the object can be calculated via the \mathbf{k} -space fourier representation

(Eq. 2.231),

$$\hat{\mathbf{E}}(k_x, k_y; 0) = \frac{1}{4\pi^2} \iint_{-\infty}^{+\infty} \mathbf{E}_0 e^{-\frac{x^2+y^2}{\omega_0^2}} e^{-i(k_x x + k_y y)} dx dy \quad (2.241)$$

$$\hat{\mathbf{E}}(k_x, k_y; 0) = \frac{\mathbf{E}_0}{4\pi^2} \left\{ \int_{-\infty}^{+\infty} e^{-x^2/\omega_0^2} e^{-ik_x x} dx \right\} \left\{ \int_{-\infty}^{+\infty} e^{-y^2/\omega_0^2} e^{-ik_y y} dy \right\} \quad (2.242)$$

$$\hat{\mathbf{E}}(k_x, k_y; 0) = \mathbf{E}_0 \frac{\omega_0^2}{4\pi} e^{-(k_x^2 + k_y^2) \frac{\omega_0^2}{4}} \quad (2.243)$$

If we substitute our Fourier spectrum into the angular spectrum representation (Eq. 2.235) we can determine how our Gaussian field disperses as it propagates spatially. Using the paraxial approximation (Eq. 2.239), we obtain an expression for the focusing of a Gaussian beam:

$$\mathbf{E}(x, y; z) = \mathbf{E}_0 \frac{\omega_0^2}{4\pi} e^{-ikz} \iint_{-\infty}^{+\infty} e^{-(k_x^2 + k_y^2)} e^{\left(\frac{\omega_0^2}{4} + \frac{iz}{2k}\right)} e^{i(k_x x + k_y y)} dk_x dk_y \quad (2.244)$$

$$\mathbf{E}(x, y; z) = \mathbf{E}_0 \frac{\omega_0^2}{4\pi} e^{-ikz} \left\{ \int_{-\infty}^{+\infty} e^{-\alpha k_x^2} e^{ik_x x} dk_x \right\} \left\{ \int_{-\infty}^{+\infty} e^{-\alpha k_y^2} e^{ik_y y} dk_y \right\} \quad (2.245)$$

$$\mathbf{E}(x, y; z) = \frac{\mathbf{E}_0 e^{-ikz}}{1 + \frac{2iz}{k\omega_0^2}} e^{-\left[\frac{x^2+y^2}{\omega_0^2} + \frac{2iz}{k\omega_0^2}\right]} \quad (2.246)$$

$$1 \left\{ \int_{-\infty}^{+\infty} e^{-x_i^2/\omega_0^2} e^{-ik_i x_i} dx_i \right\} = \left[e^{-k_i^2 \omega_0^2/4} \sqrt{\pi \omega_0^2} \right]$$

$$2 \left\{ \left[x^2 + ik_x x \omega_0^2 = \left(x + \frac{ik_x \omega_0^2}{2} \right)^2 + \frac{k_x^2 \omega_0^4}{4} \right]; \left[x' = x + \frac{ik_x \omega_0^2}{2} \right]; [dx' = dx] \right\}$$

Utilizing the following definitions, we can re-write the the Cartesian representation (Eq. 2.246) of our propagating Gaussian beam in cylindrical coordinates,

$$\mathbf{E}(\rho; z) = \mathbf{E}_0 \frac{\omega_0}{\omega(z)} e^{-\frac{\rho^2}{\omega^2(z)}} e^{-\left[kz - \eta(z) + \frac{k\rho^2}{2R(z)} \right]} \quad (2.247)$$

where ρ is the radial direction ($\rho^2 = x^2 + y^2$), $\omega(z)$ is the beam radius, $R(z)$ is the wavefront radius, $\eta(z)$ is the phase correction, z_0 is the Rayleigh length, and θ is the divergence angle. These functions express Gaussian beam propagation through a focus under the paraxial approximation and can be used for determining key

$$\begin{aligned} &^4 \alpha = \left(\frac{\omega_0^2}{4} + \frac{iz}{2k} \right) \\ &^5 \left\{ \int_{-\infty}^{+\infty} e^{-\alpha k_i^2} e^{ik_i x_i} dk_i \right\} = \left[e^{-x_i^2/4\alpha} \sqrt{\frac{\pi}{\alpha}} \right] \\ &^6 \left\{ \left[k_x^2 - \frac{ik_x x}{\alpha} = \left(k_x - \frac{ix}{2\alpha} \right)^2 + \frac{x^2}{4\alpha^2} \right]; \left[k'_x = k_x - \frac{ix}{2\alpha} \right]; \left[dk'_x = dk_x \right] \right\} \end{aligned}$$

features of \mathbf{E} field distribution:

$$z_0 = \frac{\pi n \omega_0^2}{\lambda_0} \quad (2.248)$$

$$\theta = \frac{\lambda_0}{\pi n \omega_0} \quad (2.249)$$

$$\omega(z) = \omega_0 \sqrt{1 + \left(\frac{z}{z_0}\right)^2} \quad (2.250)$$

$$R(z) = z \left(1 + \left(\frac{z}{z_0}\right)^2\right) \quad (2.251)$$

$$\eta(z) = \tan^{-1} \left(\frac{z}{z_0}\right) \quad (2.252)$$

It is an important feature of the paraxial approximation that the focus be gradual and not tight (i.e., with a small divergence angle), otherwise the paraxial approximation breaks down. An example of this breakdown is commonly observed in our lab. For our sample focus, we use a large initial beam radius and a short focal length parabolic mirror to obtain a tight, diffraction limited focus.

During Time-Domain Spectroscopy we map out the electric field waveform at the focus with a detection crystal. At this point the Gaussian shape of the waveform contains phase that corresponds to the phase correction, $\eta(z)$, in Eq. 2.247. The Gouy phase shift is the $-\pi$ to $+\pi$ phase shift that occurs as the Gaussian beam propagates from one end of the focus to the other. The Gouy phase shift can be observed by placing the detection crystal at different locations throughout the focus.

2.12 Ultrafast Pulse Propagation

Before getting into the consequences of ultrashort laser pulses, let's first make some definitions: a compressed pulse is one that is "diffraction-limited" which is defined by a pulse with zero chirp. A pulse with a chirp is described by a nonlinear temporal phase, or, frequency that changes throughout the temporal pulse duration. This section is dedicated to ultrafast Gaussian pulse propagation (chirped and unchirped) in dispersive media leading into a discussion on group velocity dispersion and dispersive pulse broadening. We must first consider a Gaussian pulse,

$$E(t) = |E(t)| e^{i\phi(t)} \quad (2.253)$$

where $|E(t)| = E_0 e^{-at^2}$ represents the Gaussian pulse envelope and $\phi(t)$ represents the temporal phase evolution. If the EM wave contains zero chirp, then the phase simplifies,

$$\phi(t) = \omega_0 t \quad (2.254)$$

There are many types of chirps (e.g., linear, quadratic, exponential, etc.) all of which contain the important relation of non-zero chirp ($\frac{d\phi}{dt} \neq 0$ or $\omega(t) \neq \text{Const.}$). In this lab, we utilize quadratic chirps for applications to DFG and pulse stretching. Chirps in our lab are achieved through pulse compression in our compression amplifier Legend system. By initiating a quadratic temporal phase,

$$\phi(t) = \omega_0 t + bt^2 \quad (2.255)$$

and consequentially a linear frequency chirp,

$$\omega = \frac{d\phi(t)}{dt} = \omega_0 + 2bt \quad (2.256)$$

then the electric field waveform changes temporal phase as follows,

$$E(t) = E_0 e^{-at^2} e^{i(\omega_0 t + bt^2)} = E_0 e^{-\Gamma t^2} e^{i\omega_0 t} \quad (2.257)$$

where $\Gamma = a - ib$ is the complex Gaussian parameter.

A linear chirp as described above contains a time-dependent frequency and can be shown in Figure 2.19.

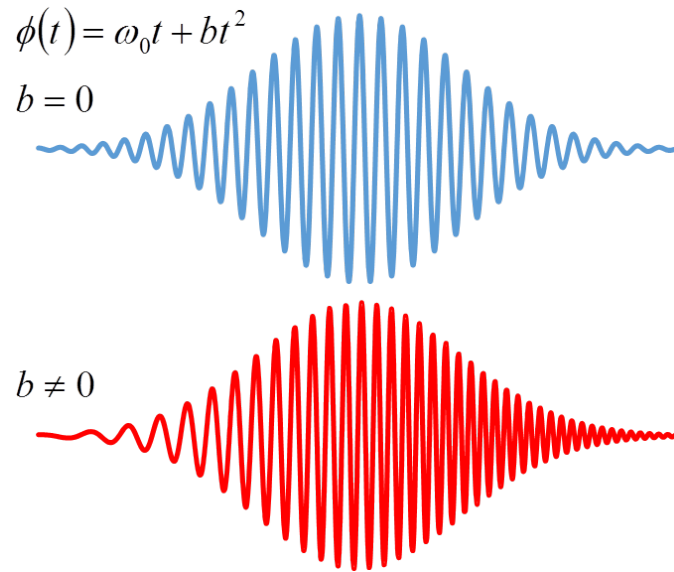


Figure 2.19: A quadratic temporal phase introduces the linear chirp parameter, b . At $b = 0$, the pulse shape is transform-limited. When $b > 0$, the pulse shape contains a positive chirp. When $b < 0$, the pulse shape contains a negative chirp.

The consequences of a linear chirp can be seen in the frequency spectrum:

$$E(\omega) = E_0 \int_{-\infty}^{\infty} e^{-\Gamma t^2 - i(\omega - \omega_0)t} dt \quad (2.258)$$

$$= E_0 \sqrt{\frac{\pi}{\Gamma}} e^{-\frac{(\omega - \omega_0)^2}{4\Gamma}} \quad (2.259)$$

$$= \frac{E_0 \sqrt{\pi}}{(a^2 + b^2)^{\frac{1}{4}}} e^{-\frac{a(\omega - \omega_0)^2}{4(a^2 + b^2)}} e^{i(b + \frac{1}{2} \tan^{-1}(\frac{b}{a}))} \quad (2.260)$$

The real component in the frequency domain is considered the “Gaussian envelope” and the imaginary component is considered the “Quadratic phase shift”. By looking at the power spectrum we can ignore the imaginary component of the field spectrum:

$$I(\omega) \propto e^{-\frac{a(\omega - \omega_0)^2}{2(a^2 + b^2)}} = e^{-(4 \ln 2) \left(\frac{\omega - \omega_0}{\Delta \omega_p} \right)^2} \quad (2.261)$$

where the pulse spectral bandwidth, $\Delta \omega_p$ and Δf_p , are determined by the spectral parameter, a , and the chirp parameter, b ,

$$\Delta \omega_p = 2\sqrt{2 \ln 2} \sqrt{a [1 + (b/a)^2]} \quad (2.262)$$

$$\Delta f_p = \frac{\Delta \omega_p}{2\pi} = \frac{\sqrt{2 \ln 2}}{\pi} \sqrt{a [1 + (b/a)^2]} \quad (2.263)$$

The pulse-duration and spectral-bandwidth product is governed by the chirping parameter,

$$\Delta f_p \tau_p = \left(\frac{2 \ln 2}{\pi} \right) \sqrt{1 + (b/a)^2} \quad (2.264)$$

where a transform-limited pulse is defined by zero chirp ($b = 0$).

Ultrafast Gaussian pulse propagation through dispersive matter leads to group velocity dispersion and dispersive pulse broadening. In our lab, we can tune the initial ultrafast Gaussian pulse by varying the compression inside our compressor/amplifier Legend system. Consider a fixed spectral bandwidth at the output of the experimental laser system. We begin with a Gaussian spectrum,

$$E(\omega) = E_0 e^{-\alpha(\omega-\omega_0)^2} e^{-i\beta(\omega-\omega_0)^2} \quad (2.265)$$

The temporal form of this spectrum can be deduced by Fourier transform:

$$E(t) = \int_{-\infty}^{\infty} E(\omega) e^{i\omega t} d\omega \quad (2.266)$$

$$= E_0 \int_{-\infty}^{\infty} e^{-\gamma(\omega-\omega_0)^2 + i\omega t} d\omega \quad (2.267)$$

where $\gamma = \alpha + i\beta$,

$$E(t) = E_0 \int_{-\infty}^{\infty} e^{-(\gamma\omega^2 - (it + 2\gamma\omega_0)\omega + \gamma\omega_0^2)} d\omega \quad (2.268)$$

$$= E_0 \sqrt{\frac{\pi}{\gamma}} e^{-\frac{t^2}{4\gamma}} e^{i\omega_0 t} \quad (2.269)$$

$$= \frac{E_0 \sqrt{\pi}}{(\alpha^2 + \beta^2)^{\frac{1}{4}}} e^{-\frac{\alpha}{4(\alpha^2 + \beta^2)} t^2} e^{i\frac{\beta}{4(\alpha^2 + \beta^2)} t^2} e^{i\frac{1}{2} \tan^{-1}\left(\frac{\beta}{\alpha}\right) e^{i\omega_0 t}} \quad (2.270)$$

The pulse duration depends on the Gaussian pulse envelope,

$$\tau_p = \sqrt{4 \ln 2} \sqrt{\frac{\alpha^2 + \beta^2}{\alpha}} \quad (2.271)$$

which changes based on the initial chirp parameter, β .

Thus far, we have neglected pulse propagation. To begin, we must consider a Gaussian pulse propagating through a uniform, lossless, and dispersive medium, such that $\frac{dn}{d\omega} \neq \text{Const.}$ and $\text{Im}[\tilde{n}]$ are satisfied. We will also suppose that the dielectric response of the medium is slowly varying over the bandwidth of your Gaussian spectrum such that we can use a Taylor expansion of the wave vector, $k(\omega) = \frac{\omega}{c}n(\omega)$, about the center frequency of the Gaussian spectrum, ω_0 ,

$$k(\omega) \cong k(\omega_0) + \left. \frac{dk}{d\omega} \right|_{\omega=\omega_0} (\omega - \omega_0) + \frac{1}{2} \left. \frac{d^2k}{d\omega^2} \right|_{\omega=\omega_0} (\omega - \omega_0)^2 \quad (2.272)$$

$$k \cong k + k'(\omega - \omega_0) + \frac{1}{2}k''(\omega - \omega_0)^2 \quad (2.273)$$

If we consider the initial non-dispersed Gaussian wave packet to be located at $z = 0$, then a Gaussian pulse propagating through a dispersive medium will pick up a phase factor after propagating a distance, z ,

$$E(z, \omega) = E(\omega) e^{-ik(\omega)z} \quad (2.274)$$

Notice, however, that in the far field, the power spectrum remains the same,

$$|E(z, \omega)|^2 = |E(\omega)|^2 \quad (2.275)$$

If we substitute our original chirped Gaussian pulse (originally in its temporal form, then Fourier transformed) from Eq. 2.258 into Eq. 2.274, we can determine the spectral and temporal shape of the Gaussian pulse as it propagates and disperses through space,

$$E(z, \omega) = E_0 \sqrt{\frac{\pi}{\Gamma_0}} e^{-ik(\omega_0)z - ik'z(\omega - \omega_0) - \left(\frac{1}{4\Gamma_0} + \frac{ik''z}{2}\right)(\omega - \omega_0)^2} \quad (2.276)$$

where Γ_0 is substituted for Γ from Eq. 2.258.

To determine the temporal form of the electric field at any position, you can simply Fourier transform the electric field spectrum:

$$E(z, t) = \int_{-\infty}^{\infty} E(z, \omega) e^{i\omega t} d\omega \quad (2.277)$$

$$= E_0 \sqrt{\frac{\pi}{\Gamma_0}} \int_{-\infty}^{\infty} e^{i\omega t - ik(\omega_0)z - ik'z(\omega - \omega_0) - \left(\frac{1}{4\Gamma_0} + \frac{ik''z}{2}\right)(\omega - \omega_0)^2} d\omega \quad (2.278)$$

$$= 2\pi E_0 \sqrt{\frac{\Gamma(z)}{\Gamma_0}} e^{-\Gamma(z)(t - k'z)^2} e^{i(\omega_0 t - k(\omega_0)z)} \quad (2.279)$$

where $\frac{1}{\Gamma(z)} = \frac{1}{\Gamma_0} + 2ik''z$. If we use the definitions for group velocity and phase

velocity (Eqs. 2.44 and 2.45), we can re-write Eq. 2.279,

$$E(z, t) = 2\pi E_0 \sqrt{\frac{\Gamma(z)}{\Gamma_0}} e^{-\Gamma(z) \left[t - \frac{z}{v_g(\omega_0)} \right]^2} e^{i \left[t - \frac{z}{v_g(\omega_0)} \right]} \quad (2.280)$$

This representation of the chirped Gaussian profile contains the new Gaussian parameter, $\Gamma(z)$, which contains the group velocity dispersion (GVD) parameter, k'' , and the chirping parameters contained within the complex Gaussian parameter, $\Gamma_0 = a - ib$.

To begin on a discussion on the spectral bandwidth and pulse duration become dependent on GVD, it is important to understand how the $\Gamma(z)$ term behaves in both field representations.

In the frequency domain, the field is proportional to $e^{-\Gamma(z)}$:

$$\frac{1}{\Gamma(z)} = \frac{1}{a_0 - ib_0} + 2ik''z \quad (2.281)$$

$$= \frac{a_0}{a_0^2 + b_0^2} + i \left(\frac{b_0}{a_0^2 + b_0^2} + 2k''z \right) \quad (2.282)$$

The propagation distance, z , and the GVD parameter, k'' , are contained only in the imaginary component of the Gaussian parameter, $\text{Im} \left[\frac{1}{\Gamma(z)} \right]$. This means that the spectral bandwidth is not dependent on propagation distance, z , or the GVD parameter, k'' ,

$$\Delta\omega_p = 2\sqrt{2 \ln 2} \sqrt{\frac{a_0^2 + b_0^2}{a_0}} \quad (2.283)$$

however, the spectral bandwidth is dependent on the initial chirp of the pulse, b_0 .

In the time domain, the field is proportional to e^Γ :

$$\Gamma(z) = \frac{a_0 - ib_0}{1 + 2b_0k''z + 2ia_0k''z} = a(z) - ib(z) \quad (2.284)$$

The propagation distance, z , and the GVD parameter, k'' , are contained in the real component of the Gaussian parameter, $\text{Re}[\Gamma(z)]$. This means that the spectral bandwidth is indeed dependent on propagation distance, z , and the GVD parameter, k'' . We clarify the spatial dependence on the spectral parameter, $a(z)$, and chirp parameter, $b(z)$,

$$a(z) = \frac{a_0}{(1 + 2b_0k''z)^2 + (2a_0k''z)^2} \quad (2.285)$$

$$b(z) = \frac{b_0(1 + 2b_0k''z) + 2a_0^2k''z}{(1 + 2b_0k''z)^2 + (2a_0k''z)^2} \quad (2.286)$$

This means that the pulse duration is indeed dependent on propagation distance, z , and the GVD parameter, k'' :

$$\tau_p = \sqrt{\frac{2 \ln 2}{a(z)}} = \sqrt{\frac{2 \ln 2}{a_0} [(1 + 2b_0k''z)^2 + (2a_0k''z)^2]} \quad (2.287)$$

and as the Gaussian pulse propagates and broadens through the dispersive medium, the chirp parameter, $b(z)$, continuously draws out and perpetuates more dramatic linear chirping.

Even when we consider the special scenario where the initial pulse is diffraction-

limited, or, zero chirp, $b_0 = 0$,

$$a(z, b_0 = 0) = \frac{a_0}{1 + 4a_0^2 k''^2 z^2} \quad (2.288)$$

$$b(z, b_0 = 0) = \frac{2a_0^2 k'' z}{1 + 4a_0^2 k''^2 z^2} \quad (2.289)$$

we see that the pulse broadens in the time domain ($a(z) > a_0$) and in fact, the chirp parameter becomes non-zero ($b(z) > 0$ for normal dispersion and $b(z) < 0$ for anomalous dispersion). Thus, negative chirped pulses, and self-compression of positive chirped pulses, can be a natural consequence of dispersion.

Even in this simplified case ($b_0 = 0$), the pulse duration broadens by the propagation distance and GVD:

$$\tau_p = \sqrt{\frac{2 \ln 2}{a_0} (1 + 4a_0^2 k''^2 z^2)} = \tau_p(z = 0) \sqrt{1 + 4a_0^2 k''^2 z^2} \quad (2.290)$$

We can re-write the dispersive pulse broadening in terms of dispersion length, z_D ,

$$\tau_p = \tau_p(z = 0) \sqrt{1 + \left(\frac{z}{z_D}\right)^2} \quad (2.291)$$

where,

$$z_D = \frac{1}{2a_0 k''} = \frac{\tau_p^2(z = 0)}{(4 \ln 2) k''} \quad (2.292)$$

Specifically, these conditions only occur over distances comparable to the dispersion length. In most cases, aside from near resonance conditions (See Figure

2.2), GVD is relatively low and can be represented in the following way,

$$k''(\omega_0) = \frac{d}{d\omega} \left(\frac{1}{v_g} \right)_{\omega=\omega_0} = -\frac{1}{v_g^2} \left(\frac{dv_g}{d\omega} \right)_{\omega=\omega_0} \quad (2.293)$$

where GVD is dependent on group velocity, v_g . If v_g is constant near the vicinity of the experimental spectral bandwidth, then GVD is zero.

2.13 Determining Beam Shape

Determination of a THz beam shape can be a complex task. Imaging techniques are typically limited to raster imaging or two-dimensional scanning, which takes several minutes. There exist room-temperature micro-bolometer arrays for imaging purposes, but these THz products are quite expensive, on the order of \$50k in price. Based on the price of a THz camera, taking an extra 3 – 30 minutes to generate a beam profile becomes a bit more reasonable.

The most accurate beam profiling method would be the use of a pin hole. The beam profile can be mapped out by Raster scanning the pin hole across the Gaussian pulse. This method usually takes around 30 minutes.

The quickest and least accurate beam profiling method would be the use of an iris. By aligning the iris to the central maximum of the beam, one can close down the iris to a specific radius and measure the total transmitted power. Under the approximation that the Gaussian pulse is circular (which can be an extreme approximation when the quality of THz alignment is in question), one can determine

the beam radius.

A moderately quick and a relatively accurate method in determining beam shape is by scanning a razor blade edge in two orthogonal directions across the Gaussian beam. This gives us a two dimensional, beam profile that is capable of determining ellipticity. The razor blade edge method is called performing a “knife edge” and usually takes around 5 – 10 minutes. This is the process we most commonly use in our lab.

Regardless of which method is used, there is a bit of math to calculate the beam shape. This section is dedicated to discussing the methodology and the mathematics behind each task.

To begin, lets point out the shape of a Gaussian beam and the total power of said shape for both a circular and an elliptical profile,

$$P_{\text{circular}}(t, \tau, \omega_0) = I_0 e^{-t^2/\tau^2} \int_0^{2\pi} d\phi \int_0^{\infty} r e^{-2r^2/\omega_0^2} dr \quad (2.294)$$

$$P_{\text{ellipse}}(t, \tau, \omega_{x0}, \omega_{y0}) = I_0 e^{-t^2/\tau^2} \int_{-\infty}^{+\infty} e^{-2x^2/\omega_{x0}^2} dx \int_{-\infty}^{+\infty} e^{-2y^2/\omega_{y0}^2} dy \quad (2.295)$$

By assuming a constant peak power which contains an arbitrary temporal form,

$$P_0 = I_0 e^{-t^2/\tau^2} \quad (2.296)$$

the functional dependence becomes solely on the Gaussian spatial distribution which is dependent on the beam profile in one (two) direction(s), r (x and y), for

a circular (elliptical) beam shape. Using the following identity,

$$\int_0^{\infty} x^n e^{-ax^2} dx = \frac{\Gamma\left(\frac{n+1}{2}\right)}{2a^{(n+1)/2}} \quad (2.297)$$

one can confirm that the total integrated power for both of these representations are the same ($P_{\text{tot}} = P_0 \frac{\text{Area}}{2}$). Starting with Eq. 2.295, a knife edge allows the whole region from $-\infty$ to $+\infty$ in one direction, but only passes a partial region from $-\infty$ to the knife position, y_{lim} , in the other direction. By tuning various knife positions and measuring the resulting power, one can derive the beam waist:

$$P_{\text{ellipse}}(\omega_{x0}, \omega_{y0}, y_{\text{lim}}) = P_0 \int_{-\infty}^{+\infty} e^{-2x^2/\omega_{x0}^2} dx \int_{-\infty}^{y_{\text{lim}}} e^{-2y^2/\omega_{y0}^2} dy \quad (2.298)$$

$$= P_0 \frac{\pi}{2} \omega_{x0} \omega_{y0} \left[\frac{1}{2} \operatorname{erf} \left(\frac{\sqrt{2}y}{\omega_{y0}} \right) \right]_{-\infty}^{y_{\text{lim}}} \quad (2.299)$$

$$P_{\text{ellipse}}(\omega_{y0}, y_{\text{lim}}) = \frac{1}{2} P_{\text{tot}} \left[\operatorname{erf} \left(\frac{\sqrt{2}y_{\text{lim}}}{\omega_{y0}} \right) + 1 \right] \quad (2.300)$$

Our power meter measures the power that is unblocked by the knife. An error function is drawn when the knife is scanned across the Gaussian beam. Refer to Table 2.6 for a list of some notable knife positions to estimate the beam waist of your Gaussian beam.

$\frac{P_{ellipse}}{P_{max}}$	$\frac{y_{lim}}{\omega_{y0}}$	$\frac{P_{circular}}{P_{max}}$	$\frac{r_{lim}}{\omega_0}$
0.5	0	0.86466	1
0.33	0.21536	0.8	0.89706
0.25	0.33724	0.5	0.58871
0.2	0.42081	0.25	0.37926
0	∞	0.1	0.22952

Table 2.6: Expected relative power transmission for various knife-edge positions and iris radii.

For the iris method, an iris is centered at the maximum of the Gaussian profile and closed down at the beam waist. Through Eq. 2.294, we can derive the measured power as a function of the iris radius, r_{lim} by changing the upper integration limit from $-\infty$ to r_{lim} ,

$$\int_0^{r_{lim}} r e^{-2r^2/\omega_0^2} dr = \frac{1}{4} \omega_0^2 \left(1 - e^{-2r_{lim}^2/\omega_0^2} \right) \quad (2.301)$$

$$P_{circular}(\omega_0, r_{lim}) = \left(P_0 \frac{2\pi}{4} \omega_0^2 \right) \left(1 - e^{-2r_{lim}^2/\omega_0^2} \right) \quad (2.302)$$

$$= P_{tot} \left(1 - e^{-2r_{lim}^2/\omega_0^2} \right) \quad (2.303)$$

The ratio of the iris radius relative to the beam waist can be calculated,

$$\frac{r_{lim}}{\omega_0} = \sqrt{-\frac{1}{2} \ln \left(1 - \frac{P_{circular}}{P_0} \right)} \quad (2.304)$$

The amount of power that is unblocked by the iris is measured by our power meter. Refer to Table 2.6 for a list of some notable iris diameters to estimate the beam waist of your Gaussian beam profile.

2.14 Picosecond Pulse Detection with a Millisecond THz Detector

The most common sensitive THz detector is a liquid helium cooled silicon bolometer, a thermal detector. Incident radiation heats a material with a temperature dependent electrical resistance. The difference in operation of a semiconductor at cryogenic temperatures versus a room temperature absorber is sensitivity. Our silicon bolometer can measure nanojoules of heat. Another common, less sensitive, THz detector is a room-temperature pyroelectric, another thermal detector. Incident radiation heats a material which generates a temporary voltage. The atomic arrangement is skewed such that the polarization of the material changes, this polarization change gives rise to a voltage across the pyroelectric crystal.

In this section, we will consider our detector to be a perfect detector with negligible circuit rise time. If we consider the detector to be a photon counter, we expect the voltage response to correspond directly to the total energy of our Gaussian pulse of photons,

$$V_{\text{pk-pk}} = \alpha_p U_{\text{tot}} = \alpha_p N h \nu \quad (2.305)$$

where $V_{\text{pk-pk}}$ is the peak-to-peak voltage, α_p is the pulsed responsivity of the THz

detector (units: Volts/Joule), U_{tot} is the total energy per pulse, N is the number of photons, and $h\nu$ is the energy per photon. If we consider the photon packet to contain a Gaussian temporal distribution, we can calculate the rising voltage response by integrating the wave packet,

$$V_{\text{rise}} = \int_{-\infty}^t \alpha_p N_{\text{photons}}(t') dt' = \frac{1}{2} \alpha_p N h \nu \left(1 + \text{erf} \left(\frac{2\sqrt{\ln 2}}{\tau_{\text{pulse}}} t \right) \right) \quad (2.306)$$

which results in an error function and is displayed in Figure 2.20a. To be clear, V_{rise} is merely the rising detector voltage and is the electronic response to the packet of photons where the detector is simply a photon counter. N_{photons} is the energy of the photons per unit time corresponding to the functional response in Figure 2.20a.

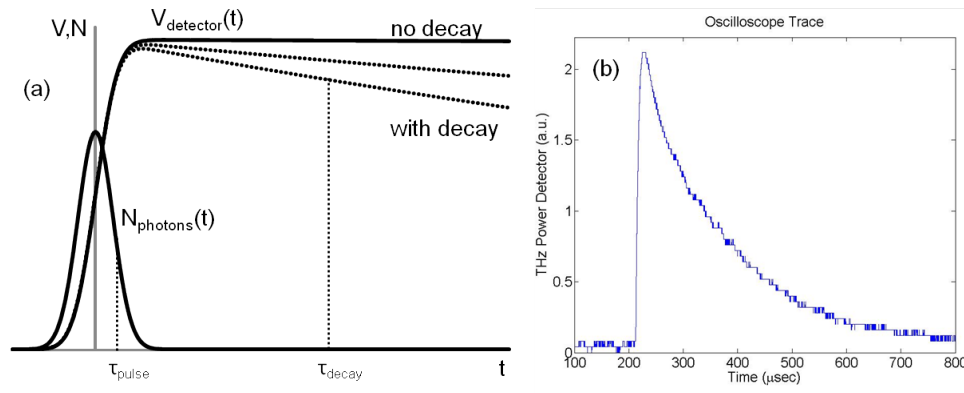


Figure 2.20: Material rise time and decay time in response to a wave-packet of photons. Electron detection schemes are slow responders to photon packets. They are capable of measuring the total number of photons by utilizing the peak-to-peak amplitude and the decay time of the voltage signal. (a) Theoretical example of rise and decay from a photon packet. (b) An oscilloscope trace from our pyroelectric THz detector.

We can consider the total detector voltage, V_{detector} to be dependent on the rising voltage from the incident photon packet (solid error function). If we incorporate dependence on the decaying behavior of the detector (dashed lines), the resulting voltage function form looks like that of Figure 2.20b. The rising and decaying voltage functions can be considered independent of one another,

$$V_{\text{detector}}(t) = V_{\text{rise}}(t) V_{\text{decay}}(t) \quad (2.307)$$

if the detector decay time is much longer than the pulse duration,

$$\tau_{\text{decay}} \gg \tau_{\text{pulse}} \quad (2.308)$$

The total detector voltage can be described as,

$$V_{\text{detector}}(t) = \frac{1}{2} V_{\text{pk-pk}} \left(1 + \operatorname{erf} \left(\frac{2\sqrt{\ln 2}}{\tau_{\text{pulse}}} t \right) \right) e^{-t/\tau_{\text{decay}}} \quad (2.309)$$

This is what is displayed in Figure 2.20. The important feature contained in this function is the $1/e$ voltage detector decay time. The laser repetition rate must be much longer than the decay time such that the pulsed signal gets a chance to decay to zero before the next incident pulse hits the detector,

$$\tau_{\text{rep. rate}} \gg \tau_{\text{decay}} \quad (2.310)$$

If your laser system repetition rate is too slow, you will either need to chop the

pulses to slow the rate, or you will need a faster detector.

For a continuous wave (CW) laser, there is a direct relationship between the voltage signal, $V_{\text{pk-pk}}$, and laser power, P_{CW} , by a constant that is called the responsivity, S (units: Volt/Watt),

$$V_{\text{pk-pk}} = SP_{\text{CW}} \quad (2.311)$$

In order to detect a voltage, the detector must decay and the CW laser must be chopped, alternating off and on at a rate, τ_{chopper} , such that the voltage signal has enough time to saturate to $V_{\text{pk-pk}}$ when the laser is passed by the chopper or decay to zero when the laser is blocked,

$$\tau_{\text{chopper}} \gg \tau_{\text{decay}} \quad (2.312)$$

The way the signal builds in CW detection is slightly different than pulsed laser detection. First, CW is a continuous stream of photons. If a photon counter had an infinite decay time, then the detector voltage would increase linearly forever (see Figure 2.21).

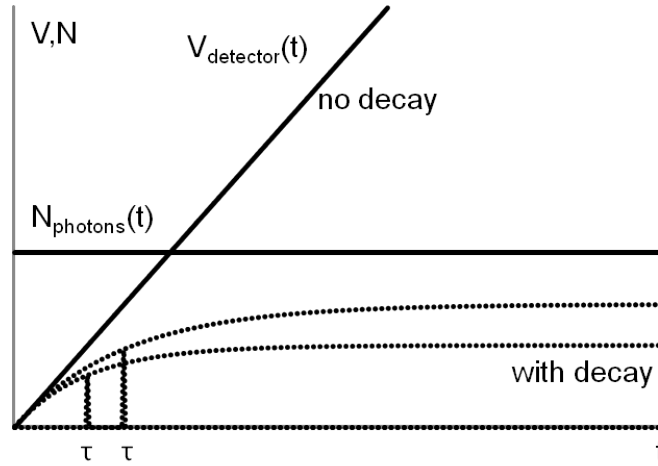


Figure 2.21: Theoretical example of rise and decay from a continuous wave laser. Material rise time and decay time in response to a continuous wave laser, or, a continuous stream of photons. Without detector decay, the voltage signal would continuously increase. However, due to detector signal decay, after some rise time, the voltage signal levels out. The peak-to-peak signal corresponds to the energy density of the continuous stream of photons.

If we introduce a non-infinite decay time, then the earlier detected photons which have already been counted by the detector voltage, V_{detector} , will eventually decay. The detector voltage will, as a result, saturate by leveling off at a maximum value, $V_{\text{pk-pk}}$ (dashed lines of Figure 2.21). The detector voltage as a function of time can be described in the following integral,

$$V_{\text{detector}}(t) = \int_0^t \alpha_p P_{\text{CW}} e^{-t'/\tau_{\text{decay}}} dt' = \alpha_p \tau_{\text{decay}} P_{\text{CW}} (1 - e^{-t/\tau_{\text{decay}}}) \quad (2.313)$$

where the maximum detector voltage corresponds to the measurable quantity,

$V_{\text{pk-pk}}$, and the CW responsivity is related to the pulsed responsivity as follows,

$$S = \alpha_p \tau_{\text{decay}} \quad (2.314)$$

This means that higher sensitivity CW detection can be obtained by increasing the detector decay time. However, this usually must be compensated by chopping your CW laser at a slower repetition rate.

2.15 THz Field Strength

Determination of THz energy and maximum field strength is a complex matter. The Si:Bolometer is a liquid-Helium cooled detector of extremely high sensitivity. The voltage signal is easily measurable on an oscilloscope and the spectral response in the THz regime is relatively flat. A room temperature pyroelectric detector is less sensitive and the voltage signal can still be measurable on an oscilloscope, but the signal is much smaller and the signal-to-noise ratio (SNR) is lower. Also, the layers in the pyroelectric can create interference fringes and absorption features in the THz spectrum (Figure 2.22). In the past, our bolometer has been calibrated with a blackbody radiation source. However, this value may change over time due to wear and tear. Our best bet is to use an approximate range for our THz energy and field strength. In this section, I will describe how to go about approximating the THz field strength.

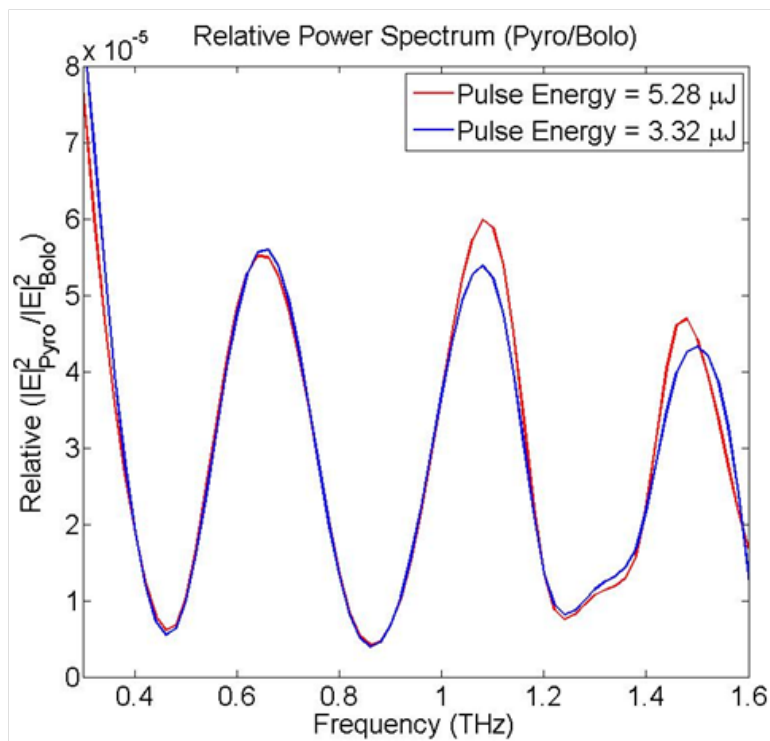


Figure 2.22: Theoretical example of rise and decay from a continuous wave laser. Material rise time and decay time in response to a continuous wave laser, or, a continuous stream of photons. Without detector decay, the voltage signal would continuously increase. However, due to detector signal decay, after some rise time, the voltage signal levels out. The peak-to-peak signal corresponds to the energy density of the continuous stream of photons.

To start, we must represent our THz field, intensity, and total pulse energy:

$$\mathbf{E}(x, y, t) = \mathbf{E}_{\max} e^{-x^2/\omega_x^2} e^{-y^2/\omega_y^2} e^{-t^2/\tau^2} \quad (2.315)$$

$$I(x, y, t) = I_0 e^{-2(x^2/\omega_x^2 + y^2/\omega_y^2 + t^2/\tau^2)} \quad (2.316)$$

$$U = \iiint_{-\infty}^{+\infty} I(x, y, t) dx dy dt \quad (2.317)$$

where ω_x and ω_y are represent the beam radius in the x- and y- directions (recall paraxial approximation Gaussian optics, Eq. 2.248) and τ is the time in which the electric field Gaussian envelope decays to $1/e$ times the maximum field. With pulsed laser systems, we commonly refer to pulse duration, τ_p , which refers to the time in which the Gaussian field envelope decays to half the maximum, the full-width half-maximum (FWHM). For a Gaussian shaped pulse, the ratio between these two time constants is,

$$\tau = \frac{1}{\sqrt{2 \ln 2}} \tau_p \quad (2.318)$$

which leads to the FWHM bandwidth,

$$\Delta\nu_p = \frac{2 \ln 2}{\pi} \frac{1}{\tau_p} \quad (2.319)$$

If we include the following identity,

$$\int_{-\infty}^{+\infty} e^{-ax^2} dx = \sqrt{\frac{\pi}{a}} \quad (2.320)$$

we can derive the total THz pulse energy,

$$U_{\text{THz}} = I_0 \left(\frac{\pi}{4} \sqrt{\frac{\pi}{\ln 2}} \right) \omega_x \omega_y \tau_p \quad (2.321)$$

We can determine the maximum THz field strength by way of the total THz pulse energy, U_{THz} (Eq. 2.317), and the relationship between intensity and maximum field strength, E_{max} (Eq. 2.35),

$$|E_{\text{max}}| = 2 \sqrt{\frac{1}{\pi}} \left(\frac{\ln 2}{\pi} \right)^{\frac{1}{4}} \sqrt{\frac{U_{\text{THz}}}{c \epsilon_0 \omega_x \omega_y \tau_p}} = 2 \left(\frac{\ln 2}{\pi} \right)^{\frac{1}{4}} \sqrt{\frac{U_{\text{THz}}}{c \epsilon_0 A \tau_p}} \quad (2.322)$$

where A is the cross-sectional area at the particular beam radius. Recall the detector voltage to pulsed energy relationship (Eq. 2.305) and the pulsed responsivity to the detector CW responsivity relationship (Eq. 2.314). Utilizing these relationships, we can determine the maximum THz field strength by measuring the THz detector peak-to-peak voltage, $V_{\text{pk-pk}}$, the pulse duration, τ_p , and the beam profile, $\{\omega_x, \omega_y\}$ or $\{A\}$,

$$U_{\text{THz}} = \frac{V_{\text{pk-pk}} \tau_{\text{decay}}}{S \gamma} \quad (2.323)$$

where γ represents the gain factor of the pre-amplifier. For the bolometer, there is a built in pre-amplifier with a switch, $\gamma = \{200, 1000\}$. With further amplification, however, noise is also amplified.

This leads to the ultimate relation between maximum THz field strength and

THz pulse energy,

$$|E_{\max}| = \sqrt{\frac{2}{\pi}} \left(\frac{\pi}{\ln 2} \right)^{\frac{1}{4}} \sqrt{\frac{V_{\text{pk-pk}} \tau_{\text{decay}} \Delta \nu_p}{S \gamma c \epsilon_0 \omega_x \omega_y}} = \sqrt{2} \left(\frac{\pi}{\ln 2} \right)^{\frac{1}{4}} \sqrt{\frac{V_{\text{pk-pk}} \tau_{\text{decay}} \Delta \nu_p}{S \gamma c \epsilon_0 A}} \quad (2.324)$$

In a typical ZnTe experiment, one would expect the following maximum THz field strength when measuring the pulse energy with a bolometer ($S \sim 2.7\text{--}3.3 \times 10^2 \frac{\text{V}}{\text{W}}$, $\gamma = 200$):

$$|E_{\max}| = \sqrt{2} \left(\frac{\pi}{\ln 2} \right)^{\frac{1}{4}} \sqrt{\frac{(12\text{V})(230\mu\text{s})(1\text{THz})}{(300\frac{\text{V}}{\text{W}})(200)c\epsilon_0(0.4\text{mm}^2)}} \times 10^{-5} \approx 100 \frac{\text{kV}}{\text{cm}} \quad (2.325)$$

How large this field strength is depends on experimental needs. If the desire is to ionize a Hydrogen atom, then a field strength comparable to the ionization energy (13.6 eV) over a distance of the Bohr radius ($a_0 = 0.529 \text{ \AA}$).

$$|E_{\text{ion, H}}| = \frac{13.6\text{V}}{5.29 \times 10^{-11}\text{m}} = 2.57 \frac{\text{GV}}{\text{cm}} \quad (2.326)$$

The ionization energy, and consequently the ionization field strength of various materials will only be less than that for the Hydrogen atom.

3 High Power THz Generation via Lithium Niobate

3.1 Overview

Lithium Niobate (LiNbO_3 - LN) has a large second-order nonlinear susceptibility coefficient ($d_{\text{eff}} = 31 \text{ pm/V}$) [6, 11, 12] making it a novel nonlinear optical crystal and a great candidate for THz generation via optical rectification (OR). [13] Not only does d_{eff} exceed our expectations for THz generation, minimal parasitic optical and THz effects are sufficient for high power THz generation [11, 14–17], as such, the conversion efficiency from optical pulse energy to THz pulse energy is on the order of a few percent [18–25]. The conversion efficiency is strongly dependent on optical wavelength and pulse duration [22] and the LN THz properties are strongly dependent on absorption and group velocity dispersion [8, 11, 26].

A host of material properties of LN that are counterproductive to THz generation exist including parasitic nonlinear optical effects, strong THz absorption, and high photorefractivity [12, 15, 20, 27]. These notable issues have been addressed by experimenting with MgO doping; the most commonly used material is less than 2 mol% doped stoichiometric LN (sLN) [8, 12]. MgO-doped sLN suppresses parasitic optical and THz effects, allowing for more efficient use in the application of THz generation via OR. Doping also increases the optical damage threshold allowing for high power THz generation. [28]

3.2 Velocity Matching

Practicing OR with femtosecond laser pulses in ZnTe is done with collinear velocity matching as discussed in Sec. 2.3. In this special scenario, the THz and 800-nm optical index of refraction in ZnTe are nearly equal and, thus, THz radiation is generated via velocity matched OR. This conventional method cannot be applied to LN, as the optical index of refraction is dramatically lower than the THz index of refraction. The OR direction in LN is governed by the d_{33} contracted second-order susceptibility tensor element. The d_{33} element corresponds to the extraordinary optical group index of refraction of LN ($n_{\text{Opt}} = 2.25$ at 800-nm) [11] and a THz refractive index, $n_{\text{THz}} = 5.12$ at 1 THz [11] (Figure 3.1).

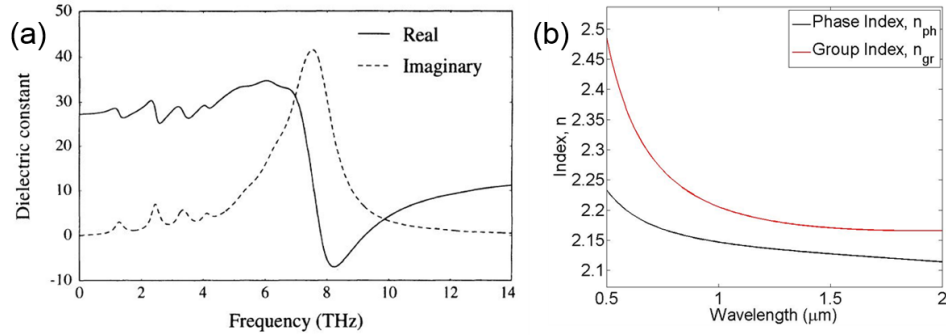


Figure 3.1: Index of refraction of Lithium Niobate in the (a) THz regime ($n_{\text{THz}} = 5.12$ at 1 THz) and (b) Optical Regime ($n_{\text{Opt}} = 2.25$ at 800-nm).

Due to this difference in refractive index, when an optical pulse propagates co-linear to a THz pulse, the THz pulse will retard the optical pulse by optical pulse duration, τ_p , after a walk-off length, ℓ_w (Eq. 2.109). As the optical pulse propagates through the medium, trailing THz pulses are generated with temporal

differences. The summation of temporally offset THz pulses causes destructive interference and thus no THz generation occurs.

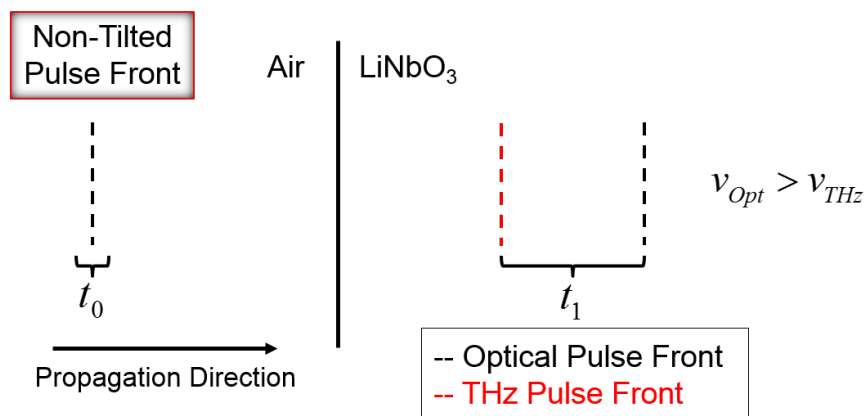


Figure 3.2: After time t_1 of propagating through the LN crystal, the optical and THz pulse fronts become separated by a distance of $\ell_w = \frac{ct_1}{n_{THz} - n_{Opt}}$

One way to alleviate the velocity mismatch constraint in LN is to tilt the optical pulse front. As a tilted optical pulse propagates through the LN crystal, the optical pulse generates constructive interference along the Cherenkov cone (Figure 3.3).

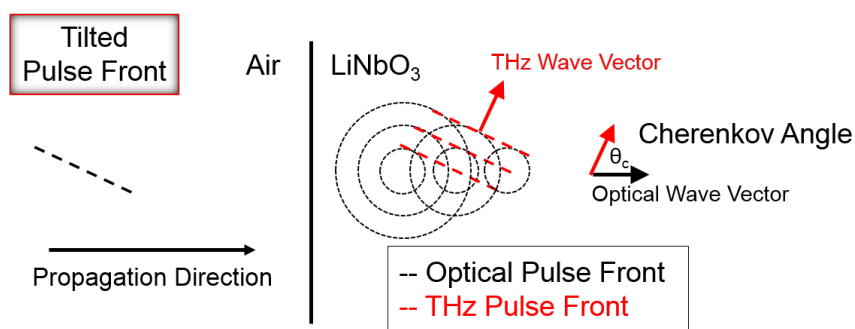


Figure 3.3: When the optical pulse front is tilted, the constructive interference creates a pseudo-velocity of the optical group velocity such that it is capable of matching the THz phase velocity.

The speed of the optical pulse as it propagates through the LN crystal is $v_{\text{Opt}} = c/n_{\text{Opt}}$, however the component of the speed orthogonal to the Cherenkov cone is $v_C = \cos \theta_C v_{\text{Opt}}$. If the optical pulse tilt angle, θ , is just right, $\theta = \theta_C$, then the speed of the Cherenkov cone will match the speed of THz radiation in the LN crystal, $v_C = v_{\text{THz}}$. At this point, THz radiation is constructively generated via velocity matched OR and the THz propagation direction is orthogonal to the Cherenkov cone and contains zero pulse front tilt. The Cherenkov angle is defined when the velocity matching condition is met,

$$\theta_C = \cos^{-1} \left(\frac{v_{\text{THz}}^{\text{ph}}}{v_{\text{Opt}}^{\text{gr}}} \right) = \cos^{-1} \left(\frac{n_{\text{Opt}}^{\text{gr}}}{n_{\text{THz}}^{\text{ph}}} \right) \approx 63.0^\circ \quad (3.1)$$

So long as the optical index of refraction is less than the THz index of refraction, we can utilize Cherenkov radiation for any material capable of OR.

It is critical to couple the THz radiation output at the LN crystal surface. As such, the LN crystal cut angle, γ , must be matched with the Cherenkov angle, θ_C ($\gamma = \theta_C \approx 63.0^\circ$). The desired optical pulse tilt angle inside the LN crystal is refracted at the LN surface, so the tilt angle outside the LN crystal must be scaled accordingly. The relationship between the tilt angle in air vs the tilt angle in LN follows,

$$\theta_{\text{Air}} = \tan^{-1} \left(\frac{n_{\text{LN}}}{n_{\text{Air}}} \tan \theta_{\text{LN}} \right) \approx 77.2^\circ \quad (3.2)$$

where it is important to correspond the internal (inside the LN crystal) tilt angle, θ_{LN} , with the Cherenkov angle, θ_C , to satisfy velocity matching ($\theta_{\text{LN}} = \theta_C$). This can be seen in Figure 3.4.

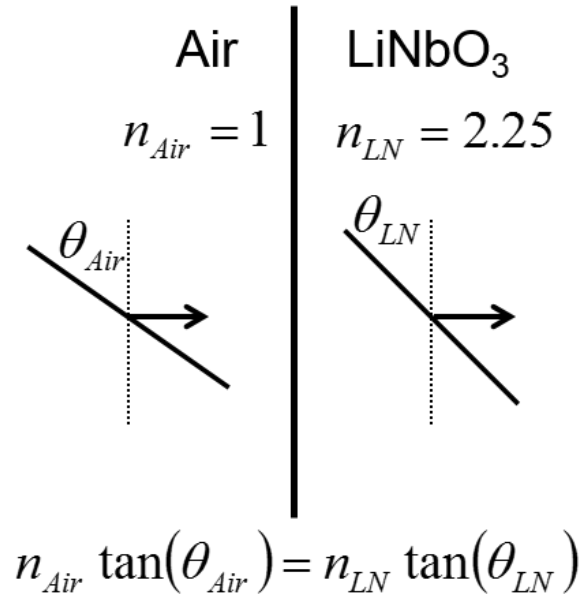


Figure 3.4: Illustration of how a tilted pulse front angle changes based on the index of refraction.

3.3 Diffraction Grating

A typical method of attaining a tilted optical pulse front is the use of diffraction gratings. The best type of diffraction grating is a blazed reflection grating, which typically demonstrates the highest optical efficiency. Consider a collimated beam with an incidence angle, θ_i , upon the diffraction grating. The optimal conversion efficiency occurs at the Littrow angle,

$$\theta_B = \alpha = \theta_{\text{Littrow}} = \theta_i = \theta_d \quad (3.3)$$

when the incident angle, θ_i , is equal to the diffraction angle, θ_d .

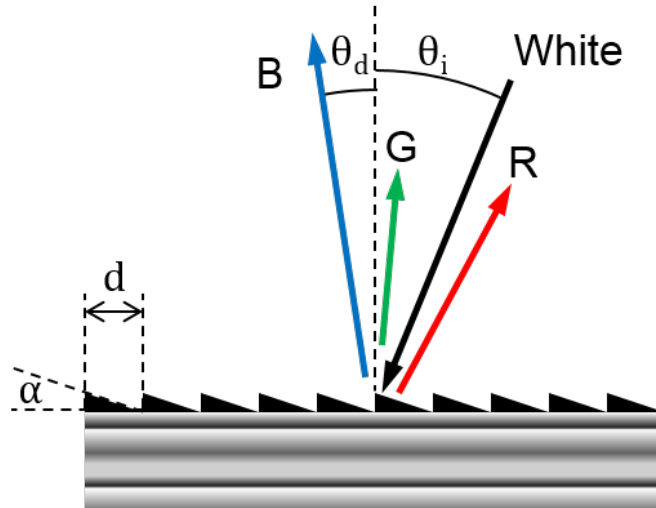


Figure 3.5: White light incident on a Blazed diffraction grating with incidence angle, θ_i , relative to normal angle diffracts its broad electromagnetic spectrum in all directions. Specific modes exit at the diffraction angle, θ_d , depending on wavelength, λ , and groove spacing, d .

The Blaze angle, θ_B , is the tilt angle of the micro-reflectors as seen in Figure 3.5. A Blazed grating consists of a long chain of saw-tooth cut micro-reflectors. Each of the micro-reflectors is treated as an individual mirror. When looking at Figure 3.5, tilt your head and look at the surfaces of the micro-reflectors, they are consistently offset by a distance that is determined by the separation distance, d and the tilt angle, α , of the micro-reflectors:

$$d \sin \alpha = \text{Offset} \quad (3.4)$$

Each of the micro-reflectors can also be considered a slit. In this case, the reflected light off of each micro-reflector behaves as a spherical radiator. A single spherical radiator has its own optical properties, that of which this section does not

go into detail and can be looked up in an introductory optics book. [3] However, when a long chain of micro-reflectors are connected side-by-side, the spherical wave fronts begin to interfere with each other. For sequential micro-reflectors, constructive interference only occurs when the path length difference between the two spherically radiating paths is equal to an integer multiple of the wavelength of light,

$$d \sin \theta_d = n\lambda \quad (3.5)$$

where θ_d and n are the diffraction angle and the diffraction order integer, respectively. This is the special scenario for light incident normal on the diffraction grating. When we choose an arbitrary incidence angle, θ_i , we arrive at the grating equation for constructive interference:

$$d (\sin \theta_d + \sin \theta_i) = n\lambda \quad (3.6)$$

A broadband electromagnetic spectrum will diffract at various angles depending on the incident wavelength. When the divergence angle of the diffracted optical beam satisfies the small angle approximation ($\sin \theta \approx \theta$ for small θ), we can approximate the divergence of the diffracted beam for first order diffractions,

$$\frac{1}{2} (\sin \theta_d^{\max} - \sin \theta_d^{\min}) \approx \theta_{\text{divergence}} = \frac{\rho \Delta \lambda}{2} = \frac{\rho \lambda_0^2 \Delta f}{2c} \quad (3.7)$$

Collimated incident radiation will diffract as a diverging beam in the dimension of the grooves (typically oriented horizontally). The vertical beam width will

continue to remain constant.

Once reflected and diffracted off of the diffraction grating, the amount of tilt in the pulse front corresponds to the diffraction angle, θ_d , as shown in Figure 3.6.

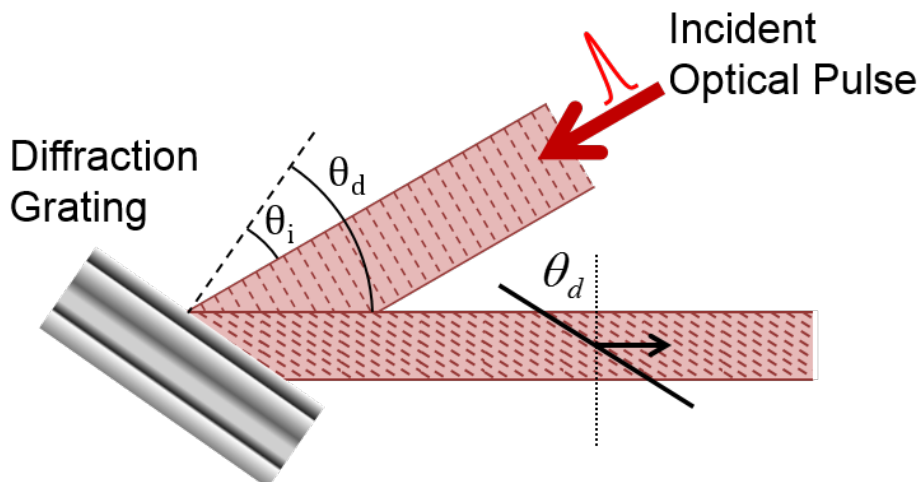


Figure 3.6: An optical pulse incident, θ_i , on a diffraction grating beginning with zero pulse front tilt acquires a tilt angle comparable to the reflected diffraction angle, θ_d .

Blazed gratings are the best external solution to tilting the pulse front. However, there are a couple of drawbacks to an external diffraction grating. Generally speaking, diffraction gratings will have a relatively low optical power conversion efficiency, certainly never unity. A diffraction grating will diffract a broadband spectrum at relatively extreme diffraction angles. Due to the spatial orientation of the diffraction grating, when placing the LN crystal immediately (or as early as spatially possible) after the diffraction grating the rapidly expanding beam becomes too large, which reduces the energy density of the optical beam and consequentially the energy density of the THz generation,

$$I_{\text{THz}} \propto I_{\text{Opt}}^2 \quad (3.8)$$

The spatially diverging beam must be recombined by a lens. Lenses typically contain wave front aberrations. It becomes immediately apparent that using an external diffraction grating concatenates issues with the use of more optics in order to resolve THz generation problems.

A more simple, straight forward approach would be to place a diffraction grating directly onto the incident surface of the LN crystal as shown in Figure 3.7. Fabrication of said device may be complex, yet attainable.

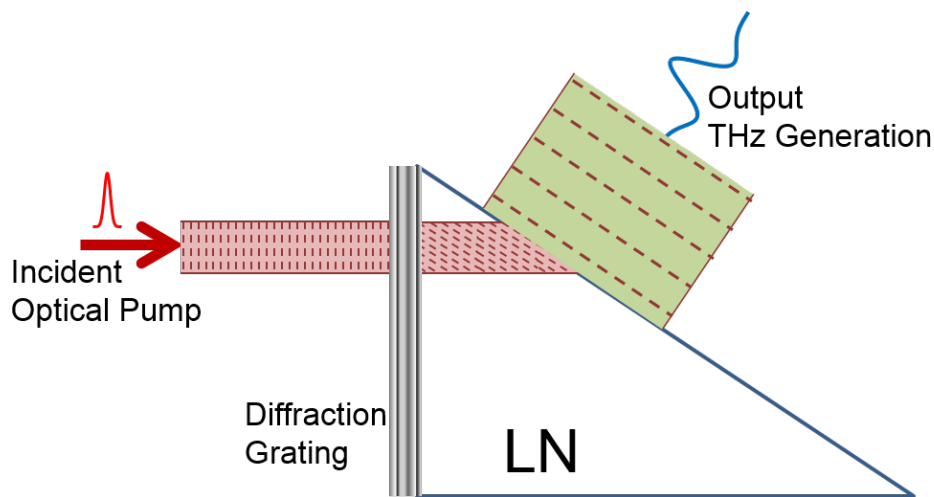


Figure 3.7: Incident and diffraction angles not to scale. A diffraction grating placed on the optical incidence surface will tilt the pulse front in order to satisfy velocity matching conditions.

For now, we will forget our dream LN system and focus on the external Blazed grating with a lens approach. This results in the necessary use of a lens. A

recombining lens will skew the optical pulse tilt angle. In addition to matching the Cherenkov angle as the pulse refracts into the LN crystal, the effect of the lens must be accounted for as well.

3.4 Single Lens

The external diffraction grating creates a diverging beam. Considering that the optically rectified THz intensity follows the square of the optical intensity (Eq. 3.8), a more concentrated optical beam will produce a larger THz intensity. Thus, the diffracted beam must be recombined with a lens such that the diffraction grating image is located at the cut surface of the LN crystal as shown in Figure 3.8.

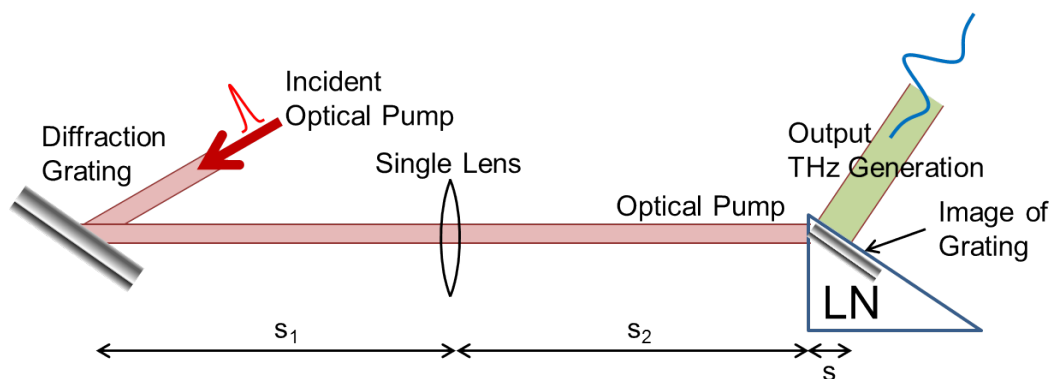


Figure 3.8: Diffracted beam coming off of diffraction grating initially diverges. The optical energy is then recombined such that the grating image is on the cut surface of the LN crystal.

The incidence angle, θ_i , the lens distance from the diffraction grating, s_1 , the lens distance to the LN input surface, s_2 , and the propagation distance inside the

LN crystal, s , are all related by the following formulas (Relationships come from Ref. [22]):

$$\sin \theta_d = \frac{\lambda_0 \rho}{n(\lambda_0) n_g(\lambda_0)} a \quad (3.9)$$

$$\sin \theta_i = \lambda_0 \rho - \sin \theta_d (\text{grating equation}) \quad (3.10)$$

$$s_1 = f (\sqrt{a} + 1) \quad (3.11)$$

$$s_2 = \frac{f s_1}{s_1 - f} - \frac{s}{n(\lambda_0)} \quad (3.12)$$

$$a = \frac{n^2(\lambda_0) n_g(\lambda_0)}{2 \lambda_0 \rho} \sqrt{\frac{\lambda_0^2 \rho^2}{n_g^2(\lambda_0) \tan^4 \gamma} + \frac{4}{n^2(\lambda_0)}} - \frac{n^2(\lambda_0)}{2 \tan^2 \gamma} \quad (3.13)$$

where $\rho = 1/d$, λ_0 , n , n_g , γ , and f represent the groove density, optical wavelength, optical phase index of refraction, optical group index of refraction, LN cut angle, and focal length respectively. Eq. 3.13 is different from Ref. [22] due to an error in the paper.

These formulas describe an optimal optical diffraction angle, θ_d , corresponding optical incidence angle, θ_i , lens position relative to the diffraction grating, s_1 , corresponding distance to the LN crystal, s_2 , and lens focal length, f , all based on the optical wavelength, λ_0 , and groove density, ρ . These variable selections are discrete based on available optics from vendors for groove density and focal length. It is important to keep in mind that the longer the distance between the diffraction grating and lens, s_1 , the wider the beam will be (Eq. 3.7) and consequentially a larger diameter lens may be necessary. The discrete solutions are graphed and

listed in Figure 3.9.

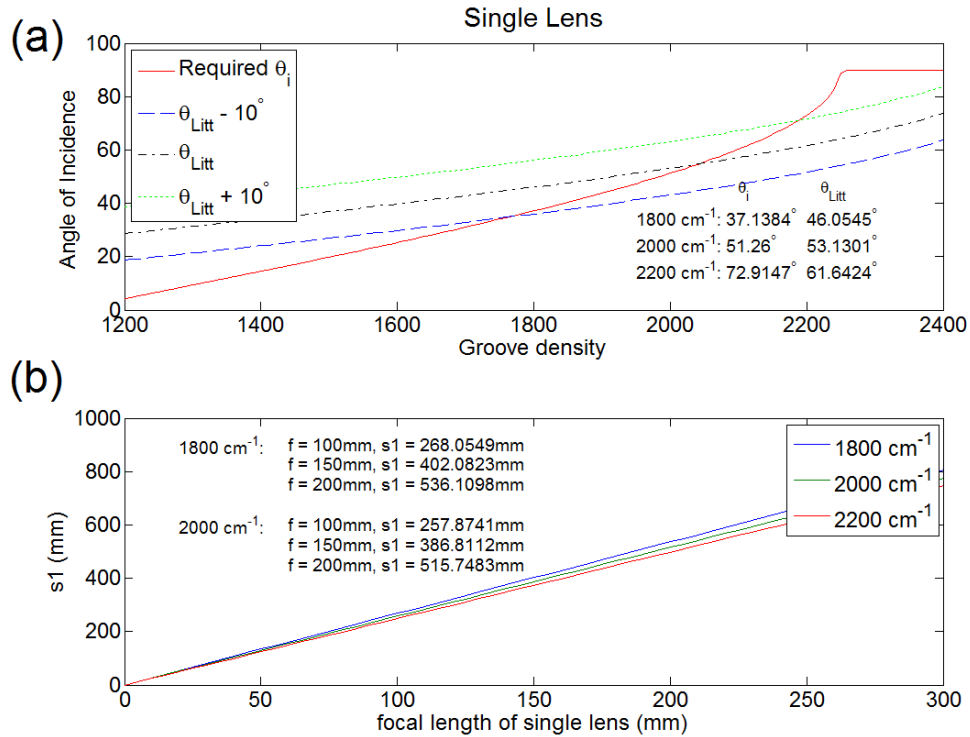


Figure 3.9: Using the equations for a single lens: (a) The angle of incidence, θ_i , can be determined as a function of diffraction grating groove density, ρ (red curve). The Littrow angle, θ_{Litt} , represents the angle in which the optical power conversion efficiency is maximized and the diffraction angle, θ_d , is equal to the incidence angle, θ_i . A beam that is reflected at the Littrow angle may not be usable due to clipping. Thus, selecting an angle that is near the Littrow angle, $\theta_{Litt} \pm 10^\circ$, is optimal. (b) The distance between the diffraction grating and the lens, s_1 , can be determined as a function of focal length, f , and groove density, ρ .

There are a couple of details to deduce from a single lens optimization. First, the optimal incidence angle for diffraction grating efficiency is the Littrow angle, θ_{Litt} , where the incidence angle, θ_i , is equal to the diffraction angle, θ_d . Con-

sequentially, the diffracted beam is unusable without clipping the incident beam under Littrow conditions. So, in order to optimize the optical conversion efficiency, one must choose an incidence angle that is slightly off of the Littrow angle, but outside the divergence angle (Eq. 3.7), or at least still near the Littrow angle, $\theta_{\text{Litt}} \pm 10^\circ$. The Littrow angle, θ_{Litt} , black dashed line of Figure 3.9a, and the corresponding optimal incidence angles, $\theta_{\text{Litt}} \pm 10^\circ$, green (+) and blue (−) dashed lines of Figure 3.9a, depend on the diffraction grating groove density, ρ . There is an optimal incidence angle for THz generation in the LN crystal based on a particular groove density, red line of Figure 3.9a. Where the red line intersects the dashed green or dashed blue lines represents the groove density that is optimal for our single lens system. Since diffraction gratings are typically available with groove densities that are discrete to the 200 mm^{-1} , we must choose the groove densities listed in Figure 3.9a. Obviously, 2000 mm^{-1} would be the most efficient choice for optical conversion efficiency. However, the incidence angle is very close to the Littrow angle ($\theta_{\text{Litt}} - \theta_i = 1.87^\circ$), resulting in clipping. Groove densities 1800 mm^{-1} ($\theta_{\text{Litt}} - \theta_i = 8.92^\circ$) and 2200 mm^{-1} ($\theta_{\text{Litt}} - \theta_i = 11.27^\circ$) would be better choices based on the divergence angle of the beam (Eq. 3.7).

Figure 3.9b shows the distance between the diffraction grating and lens, s_1 , for focal length, f , lenses listed 10, 15, and 20-cm and for groove densities, ρ , listed 1800, 2000, and 2200 mm^{-1} . Once s_1 has been chosen appropriately, s_2 and s can be calculated in preparation for an “ideal” LN alignment. One must begin with an ideal alignment, then adjust to optimize.

All focal length lenses are valid in Figure 3.9b, however drawbacks occur as

longer or shorter focal lengths are chosen. An appropriately placed short focal length lens recombines the optical energy to the smallest possible beam size; thus, the highest THz intensity is generated. The unintended consequence of said system are spherical aberrations. As it turns out, short focal length lenses create large wave front distortion. Large wave front distortion dramatically reduced THz conversion efficiency so much that the total THz intensity generated from a short focal length lens is reduced compared to the use of a longer focal length lens. In the use of a long focal length lens, an unintended consequence is extended beam propagation which forces the use of larger optics and more tabletop space. Thus, there is a sweet spot of focal length to optimize table space and pulse front distortion.

3.5 Wave Front Distortion

A single lens is capable of focusing down the optical pulse energy density such that the generated THz radiation energy density is optimized. However, there are a few things to consider before making a choice on the appropriate lens. Spherical lenses contain aberrations including wave front distortion and pulse front distortion. In a ray trace of a focusing spherical lens, the outside of the spherical lens contains a different focus location than the center of the lens, the pulse front is then distorted at the image (located at the diffraction grating image in the LN crystal). This can be seen in Figure 6 of Ref. [22]. The center of the pulse front tilts at the appropriate angle to velocity match and generate THz radiation. However, the outside of the pulse front is skewed from alignment; thus reducing the THz

generation due to partial velocity mismatch.

One would begin to believe that regardless of the focal length used, the tighter the focus, the higher the optical energy density and the higher the THz energy density. And, tight focuses can only be achieved through small focal length lenses. However, as it turns out, smaller focal length lenses create more wave front distortion. This can be seen in Figure 8 of Ref. [22]. The smaller focal length lens strongly distorts the pulse front, and dramatically reduces the THz conversion efficiency. The resulting generated THz energy is even less than that with a longer focal length lens with a smaller initial optical energy density. Similarly, long focal length lenses can reduce wave front distortion but the extension in beam propagation requires larger optics and more tabletop space. One must choose a focal length wisely to compromise the draw-backs.

3.6 Two Lens System

A method of reducing wave front distortion is the use of a second spherical lens. The second spherical lens restores a portion of the spherical aberration through an inverted effect caused by a secondary plano-convex lens [29]. As a result, the world's highest field-strength, broadband THz source was produced (as of 2011, $E_{\text{THz}} = 1.2 \text{ MV/cm}$) [29].

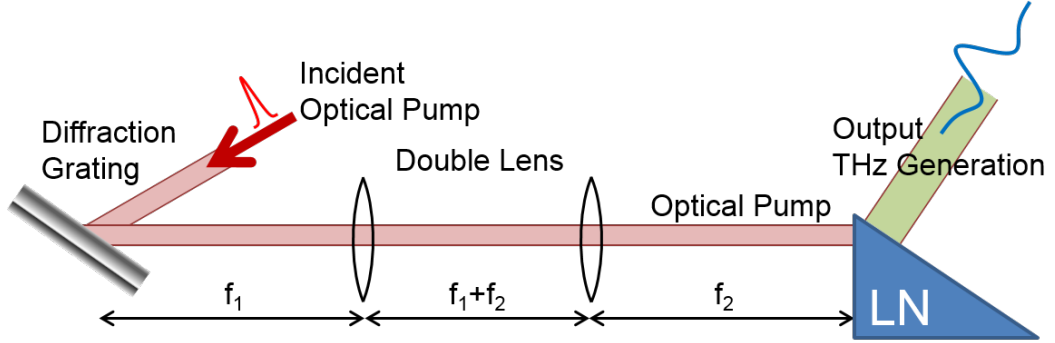


Figure 3.10: Incident optical pulse front is tilted with a diffraction grating. The diffracted beam is recombined with a two lens system in order to reduce wave front distortion. The spacing of the lenses must be near-ideal. The recombined radiation is focused onto the LN crystal for THz generation.

This arrangement contains a specific set of parameters that optimizes THz generation. Due to the second lens and the separation distances, there exists a magnification in the horizontal direction. This magnification skews the optical pulse tilt at the grating image position and must be accounted. The optimization formula can be seen below (from Ref. [29]),

$$\tan \gamma = \frac{\lambda_{\text{Opt}} \rho}{n_{\text{Opt}}^{\text{gr}} \beta_1 \cos \theta_d} \quad (3.14)$$

$$\tan \theta = \tan \gamma = n_{\text{Opt}}^{\text{ph}} \beta_2 \tan \theta_d \quad (3.15)$$

where γ , θ , λ_{Opt} , ρ , $n_{\text{Opt}}^{\text{gr}}$, $n_{\text{Opt}}^{\text{ph}}$, β_1 and β_2 , θ_d represent the LN cut angle, the pulse front tilt angle inside the LN crystal (must be matched with the Cherenkov angle and cut angle), the optical wavelength, the diffraction grating groove density, the optical group index of refraction of LN, the optical phase index of refraction

of LN, the horizontal magnification factor of the lenses, and the diffraction angle, respectively. Optimally, we plot the two functions and match where $\beta_1 = \beta_2$. The magnification parameters are optimized depending on the groove density and diffraction angle as shown in Figure 3.11:

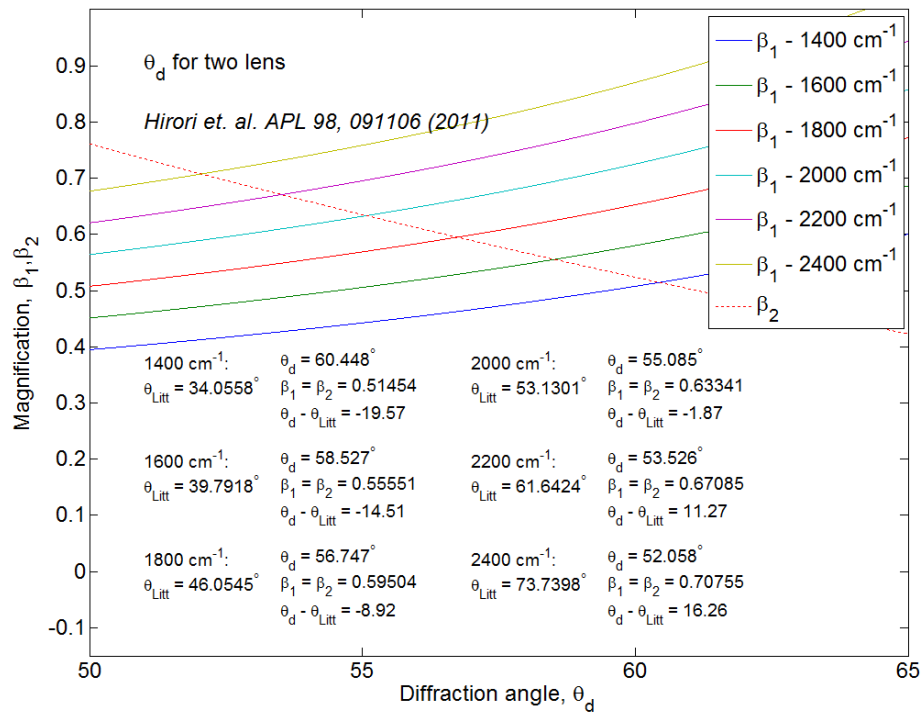


Figure 3.11: The optimized diffraction grating groove density is 1800 mm^{-1} . This creates a horizontal magnification that is allowable by vendors, $\beta \approx 0.6$ and minimizes the optical diffraction grating efficiency, $\theta_d - \theta_{\text{Litt}} < 10^\circ$.

From here, we can choose the appropriate diffraction grating groove density (by vendor) to optimize the lens pair magnification (based on vendor availability) and optical diffraction grating efficiency (minimize difference between diffraction angle

and Littrow angle, $\theta_d - \theta_{\text{Litt}}$) and, thus, optimize the theoretical THz generation.

For our LN crystal ($\gamma = 63^\circ$), the optimal diffraction grating groove density is 1800 mm^{-1} . This is because the lens magnification is close to vendor compatibility ($\beta = 0.595 \cong 0.6$). Coincidentally, the incidence angle is near the Littrow angle ($\theta_d - \theta_{\text{Litt}} = -8.92^\circ$). A groove density of 2200 mm^{-1} would have also been appropriate since $\beta = 0.671 \cong 0.667$ and $\theta_d - \theta_{\text{Litt}} = 11.27^\circ$, however the optical conversion efficiency would be slightly lower. From the diffraction angle, θ_d , we can calculate the incidence angle through the diffraction grating equation (Eq. 3.6)

Another method of reducing wave front distortion is the use of cylindrical lenses in substitute for spherical lenses. [29] The external diffraction grating only diffracts the optical spectrum in the horizontal direction and not the vertical direction. A cylindrical lens can be used to recombine the horizontal radiation. The resulting horizontal aberrations would be similar to the spherical aberrations, but only in the horizontal direction. Meanwhile, the vertical beam would be left untouched as a collimated beam through the one or two cylindrical lenses, leaving zero aberrations behind. The resulting THz generation would be more efficient with a consistent, flat optical wave front in the vertical direction. In fact, it has been shown by the use of cylindrical lenses that the generated THz radiation output propagates collimated in the vertical direction, but diverging in the horizontal direction. [29]

3.7 THz Output

Based on the divergence of the THz output in both horizontal and vertical directions, output alignment can be quite tricky resulting in a breakdown of a diffraction limited focus. In the condition that the THz beam is diverging horizontally and collimated vertically, alignment can be performed in two ways. One method is to send the output radiation into a 0° on-axis spherical mirror with an incidence angle. [17] By varying the incidence angle, the divergence of the vertical and horizontal beams can be matched allowing for standard beam alignment. This consequentially results in the use of more table space, which in the THz regime allows for more THz absorption by water vapor.

A second method would be to immediately send the THz output into a large magnification parabolic arrangement. [29] The THz alignment will be simpler to manage and less table space is used, but the diffraction limited focus will be slightly off-centered horizontally and vertically and the magnification (10x) can cause excessive clipping of the THz beam. Both methods can also be a bit tricky with day-to-day alignment of the invisible THz beam.

The best method I have discovered is the technique we currently use in the lab. The use of spherical lenses instead of cylindrical lenses for optical input to the LN crystal makes it so that the optical beam size is smaller in the vertical direction (smaller than the use of cylindrical lenses). The smaller input beam is still collimated, however the THz output is no longer collimated vertically. This results because the optical beam size in the vertical direction makes the THz

generation volume within the LN crystal small; not smaller than the wavelength, but small enough to make the Gaussian profile of the THz output diverge in the vertical direction (Figure 3.12).

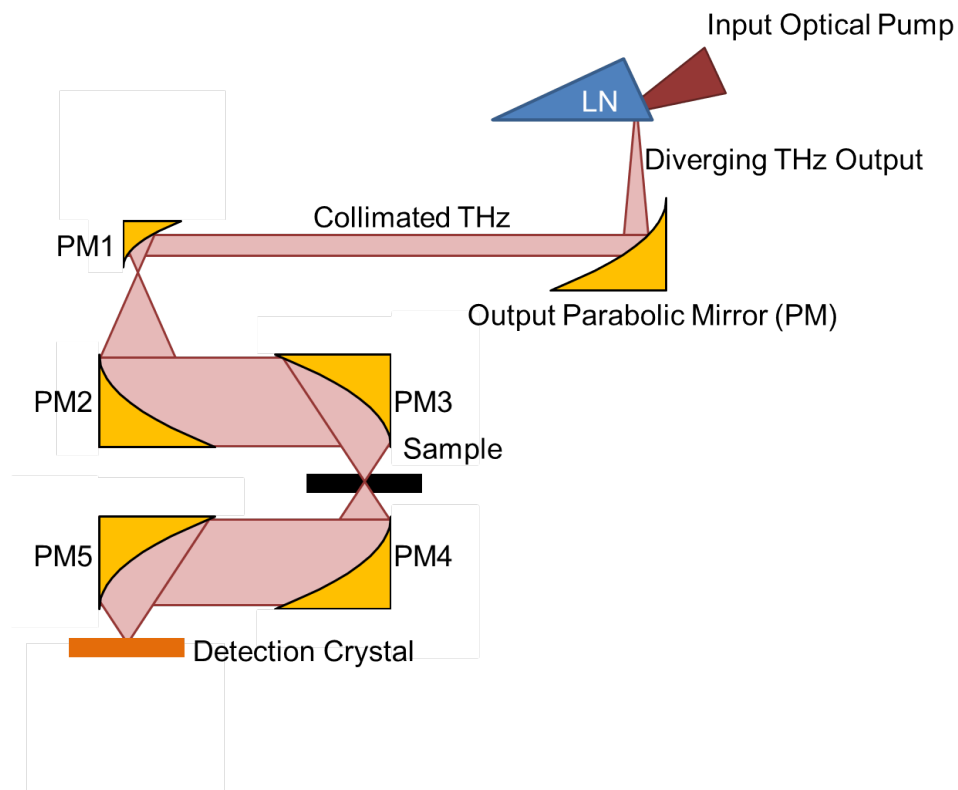


Figure 3.12: THz output direction and divergence from the LN surface and the resulting propagation path seen in typical THz experiments.

This resulting THz output that diverges in both horizontal and vertical directions is simple to work with. By placing a 90° off-axis parabolic mirror a distance equal to the focal length away from the LN crystal output surface, the reflection off of the mirror becomes collimated. An ideal THz beam propagation is easily achieved. First, beam placement on the parabolic mirror should be centered. The

THz beam position can be measured by blocking half of the parabolic mirror with an aluminum plate and measuring the THz power to be half maximum. Second, the reflection off of the parabolic mirror can be measured 90° from the output THz radiation from the LN crystal on the optics table. The resulting beam can be aligned in the far field by use of a short focal length THz lens and two large iride. (Note: The beam will apparently diverge regardless of the parabolic mirror's distance from the LN crystal).

Once the invisible beam is aligned to the two large iride, a HeNe beam can be interjected and overlapped to become co-linear with the THz beam. This visible day-to-day HeNe alignment is much simpler. Once finished remove the HeNe interjecting mirror and Voila! You should be able to attain a diffraction limited focus. Be careful with your alignment though, it is extremely sensitive. If it is not perfect, one mistake can grow throughout the parabolic arrangement.

4 Terahertz Imaging of Inhomogeneous Electrodynamics in Single-Layer Graphene Embedded in Dielectrics

4.1 Introduction

Graphene is composed of a single-atom-thick layer of carbon atoms arranged in a two dimensional honeycomb lattice [30]. The unique electronic structure of graphene gives rise to massless charge carriers and ballistic transport on a sub-micron scale at room temperature [31, 32]. The exceptional electronic properties of graphene have sparked intensive research into futuristic applications ranging from nanometer-scale switches to single molecule detection [33–38]. In particular, the high electron mobility of graphene points to great potential for broadband communications and high-speed electronics operating at terahertz (THz) switching rates [39–41]. Practical device applications require large-area graphene films, therefore, there is great interest in optimizing the growth of high-quality graphene films [42–44] and probing the electronic properties of these films at ultrafast time scales. This interest motivates our current measurements of large-area graphene by THz imaging and time-domain spectroscopy.

Graphene has a unique band structure including a cone of linear dispersion with its apex at the Dirac point, which gives rise to the extraordinary transport properties of massless relativistic fermions. [45] Charge carriers in a high-quality

graphene layer exhibit ultrahigh mobilities, undergoing ballistic transport over a long distance. It has been reported that electron mobilities can exceed $200,000 \text{ cm}^2\text{V}^{-1}$ in a free-standing graphene device. [46] The electron mobility in a large-scale graphene sheet, however, suffers a significant reduction ranging from $1,000$ to $10,000 \text{ cm}^2 \text{ V}^{-1}$ [46–48] due to scattering with extrinsic sources such as charged impurities [48–50] and microscopic ripples. [47, 51–53] Dominant scatterers are largely determined by its growth procedure. Furthermore, when a graphene sheet is deposited on a substrate, the symmetry breaking at the interface induces an intrinsic modification of the electronic structure, opening up a band gap at the Dirac point. [54–58] Inelastic scattering by surface phonons is also considered an underlying mechanism limiting the electron mobility in graphene. [59–61] Most of the practical graphene devices are fabricated on a substrate providing a supporting structure; thus it is important to understand how the graphene/substrate interface influences the electron dynamics in graphene.

We investigate the spatial inhomogeneity of graphene conductivity and the effect of interfaces on conductivity in a graphene sheet embedded between dielectric media using terahertz (THz) imaging and spectroscopy. The THz method utilizes a non-contacting, non-destructive probe to measure the local carrier dynamics of graphene with a high absorption contrast. [62] We measured the transmission of spatially focused, broadband THz pulses through the graphene samples sandwiched by an intrinsic Si substrate and a thin dielectric film of polymethyl methacrylate (PMMA) and mapped out the local sheet conductivity using raster scanning across the samples. Strong THz absorption by graphene ($\sim 20\%$) indicates that intraband

transitions dominate the interactions of THz waves with graphene. Graphene samples grown by different recipes show markedly different spatial inhomogeneity of electric conductivity. The addition of a PMMA thin film results in a slight, yet noticeable decrease in the conductivity, while THz absorption by the 100-nm thick PMMA film alone (absorption coefficient, $< 5 \text{ cm}^{-1}$) is negligible. The change in conductivity may be caused by excessive scattering sites and doped carriers at the graphene/PMMA interface.

4.2 Experiment

We grew large-area graphene on copper foil by chemical vapor deposition (CVD). Two types of samples were produced. The first type comes from a standard growth recipe with grain size of $\sim 5\text{-}\mu\text{m}$. [44] The second type was produced using a novel growth technique known as the “pita-pocket method.” [63] The grain size of the second type ranges from $50\text{-}\mu\text{m}$ to $400\text{-}\mu\text{m}$. While the individual grain size is larger, the pita-pocket graphene is inhomogeneous in a macroscopic scale of the order of millimeters. An optical microscope image of the pita-pocket graphene on SiO_2 in Figure 4.1a shows the regions of bare SiO_2 , single-layer graphene, and double-layer graphene, confirmed by Raman spectroscopy (Figure 4.1c). After the growth, we deposited a 100-nm-thick PMMA film on graphene. The PMMA/graphene layer was subsequently transferred onto two types of substrates: (1) an intrinsic Si substrate and (2) an intrinsic Si substrate with a 300-nm layer SiO_2 (made for device applications) so that the graphene layer was sand-

wiched by the two dielectric media.

We employed THz imaging and spectroscopy to investigate the graphene samples. We generated broadband THz pulses (central frequency, 1 THz; bandwidth, 1.5 THz) by optical rectification of femtosecond laser pulses in a 1-mm ZnTe crystal. Our laser system is a 1 kHz Ti:sapphire amplifier (central wavelength, 800-nm; pulse energy, 1 mJ; pulse duration, 90 fs). THz pulses were spatially focused onto the graphene samples with a diffraction limited beam size of 0.5-mm. Figure 4.1d shows a THz transmission geometry used to create two-dimensional raster scan images and perform THz time-domain spectroscopy (THz-TDS). Integrated THz power spectra were measured by a L-He-cooled Si:Bolometer. THz waveforms were measured by electro-optic (EO) sampling with a 150- μm ZnTe crystal. [64]

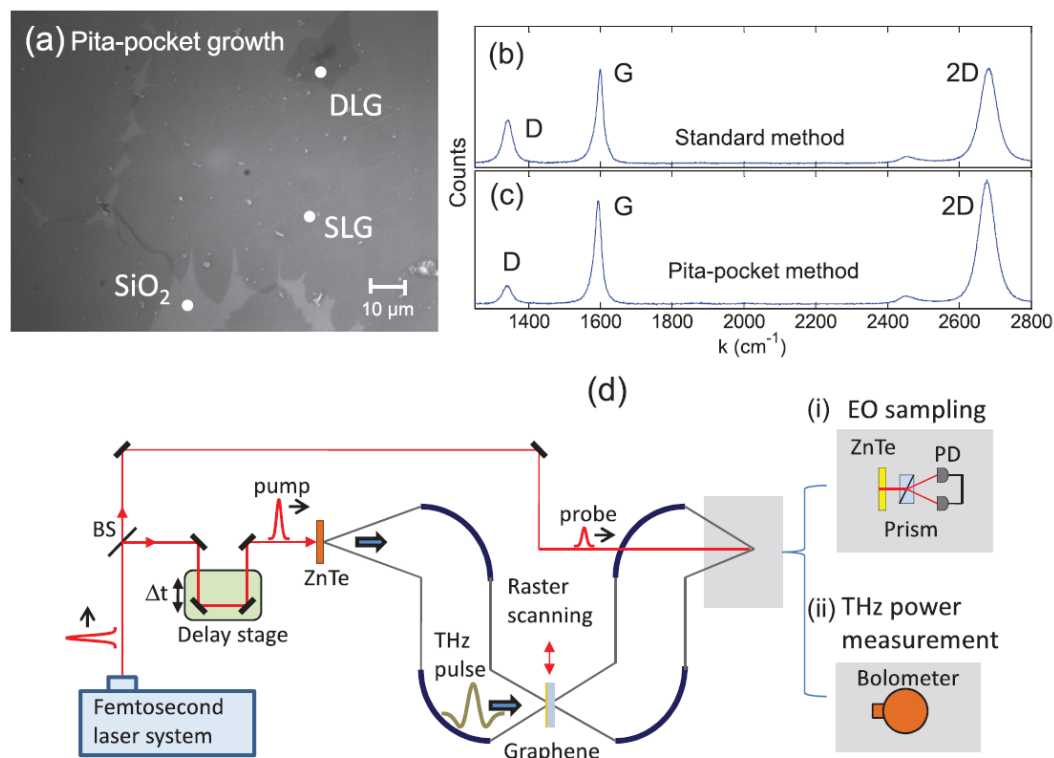


Figure 4.1: (a) Optical microscope image (100x) of pita-pocket graphene on SiO₂. (b) and (c) Raman spectra of graphene-on-Si with a 300-nm oxide layer: (b) Standard growth sample and (c) pita-pocket growth sample. (d) Schematics of (i) THz time-domain spectroscopy and (ii) raster scan THz imaging.

4.3 Power Transmission: Graphene Local Sheet Conductivity

Figures 4.2a and 4.2b show the THz transmission images of two graphene samples of standard growth and pita-pocket growth. The images cover a 20 x 20-mm² region and the pixel size is 0.25-mm. The graphene films shown in dark blue are clearly discernible against the background of the Si substrate (light-blue). The THz response of the standard-growth graphene film is nearly spatially uniform

while the pitapocket-growth film shows strong inhomogeneity. Using the Fresnel thin-film formula based on Drude conductivity, we obtain the local sheet conductivity of graphene (σ_S) via transmission measurements. [62] The transmission of the graphene/Si sample normalized by Si substrate transmission (Eq. 2.228) are transmission and reflection Fresnel coefficients for an air/Si (air/graphene/Si) interface where the thin film fresnel transmission and reflection coefficients are Eq. 2.210 and Eq. 2.219. Figures 4.2c and 4.2d show the images of the calculated local sheet-conductivity of the graphene/PMMA layer. The spatial inhomogeneity of the graphene samples is even more pronounced. The local sheet conductivity of the standard-growth graphene exhibits about 10% fluctuation across the sample, $\sigma_S = 1.3 \times 10^{-3}$ to $1.5 \times 10^{-3} \Omega^{-1}$ (sheet resistivity, $\rho_S = 710$ to $830 \Omega^{-1}/\text{sq}$), while that of the pita-pocket growth graphene widely varies from 0.6×10^{-3} to $1.5 \times 10^{-3} \Omega^{-1}$ (sheet resistivity, $\rho_S = 710$ to $1700 \Omega^{-1}/\text{sq}$).

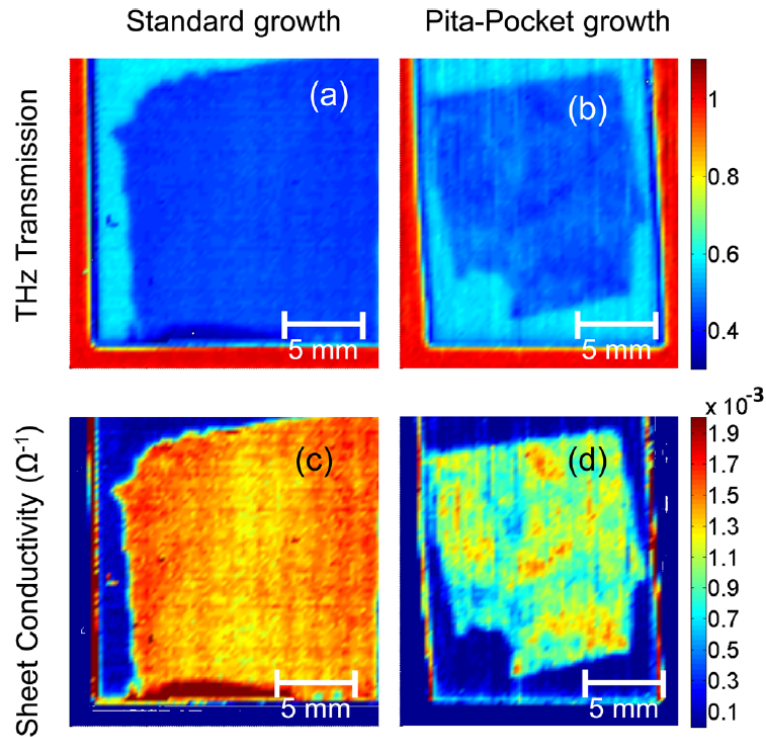


Figure 4.2: THz transmission images of the PMMA/graphene/Si samples over a $20 \times 20\text{-mm}^2$ region with a 0.25-mm pixel size: (a) standard and (b) pitapocket growth. The graphene films are shown in dark blue in the light-blue background of the Si substrate. The red regions correspond to air. (c) and (d) show calculated sheet-conductivity σ_S (Ω^{-1}) images over the graphene region.

4.4 Examining the PMMA-Graphene Interface via Power Transmission Imaging

We investigate the effects of a PMMA layer on the electron dynamics in graphene by performing THz measurements on both graphene samples, first removing the PMMA layer and then depositing a new PMMA film (thickness, 50-

nm). PMMA was removed by an ashing process at 400 °C to ensure an ultraclean surface. This process causes some thermal damage to the standard-growth sample, nearly doubling the D peak in the Raman spectrum. The average sheet conductivity lowers from 1.4×10^{-3} to $0.82 \times 10^{-3} \Omega^{-1}$. On the other hand, the PMMA removal process gives rise to a substantial increase in the average sheet conductivity of the pita-pocket sample from 0.99×10^{-3} to $1.3 \times 10^{-3} \Omega^{-1}$. Figures 4.3(a-d) show the sheet-conductivity images before and after the new PMMA layer deposition. The average sheet conductivity of the standard-growth (pita-pocket growth) graphene reduces from that of bare graphene-on-Si 0.82×10^{-3} (1.3×10^{-3}) to 0.71×10^{-3} (0.99×10^{-3}) Ω^{-1} . The reduction is uniform across the entire graphene surface.

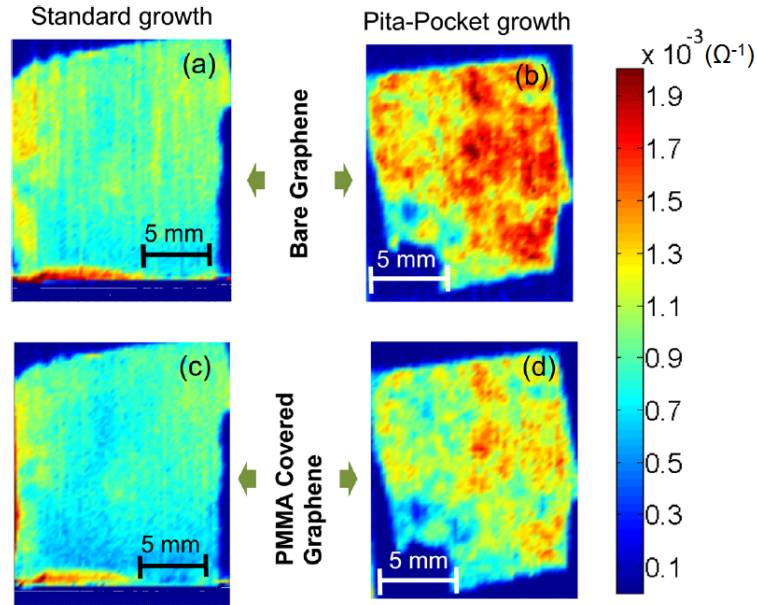


Figure 4.3: Sheet conductivity images of the bare and PMMA covered graphene layers. Standard growth: (a) bare and (c) PMMA covered. Pita-pocket growth: (b) bare and (d) PMMA covered.

4.5 Examining the PMMA-Graphene Interface via THz-TDS

In order to confirm our analysis based on Drude conductivity, we inspect frequency-dependent conductivity using THz-TDS. When a THz pulse transmitted through the graphene-on-Si sample, a portion of the pulse is directly transmitted, and the remaining portion undergoes multiple internal reflections within the Si substrate. The Si substrate is substantially thick so that the reflected pulses are temporally well separated from each other. [62]

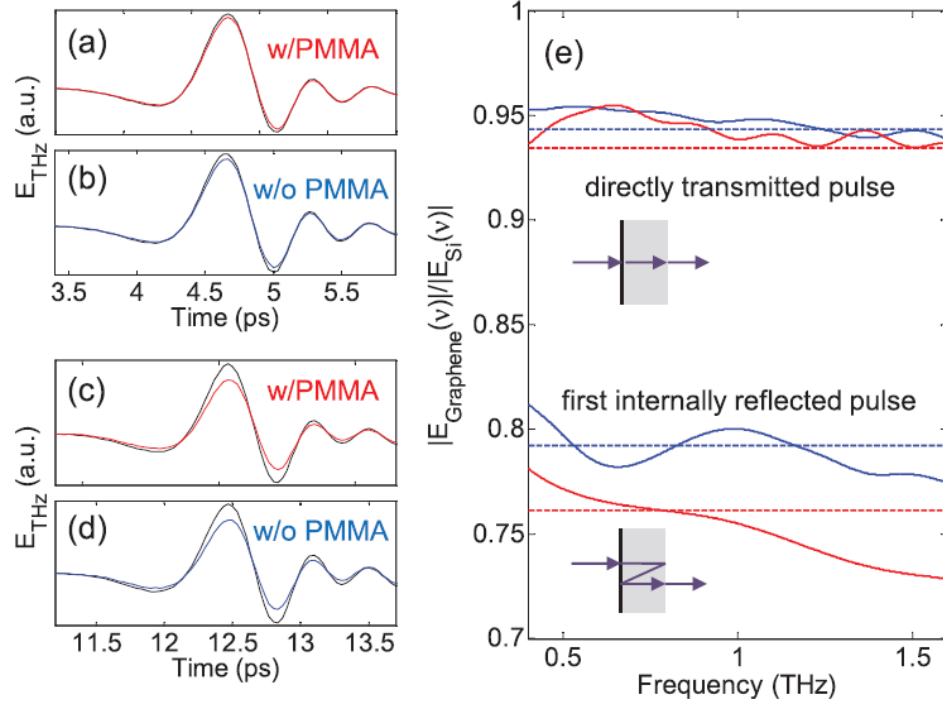


Figure 4.4: Transmitted THz waveforms through standard-growth graphene samples: directly transmitted through (a) bare and (c) PMMA covered graphene and first internally reflected through (b) bare and (d) PMMA covered graphene. The thin black lines indicate transmitted pulses through a bare Si substrate. (e) Relative transmission spectra of bare (solid red line) and PMMA covered graphene (solid blue line). The dashed lines at 0.934 (red) and 0.943 (blue) indicate the calculated relative amplitude for the directly transmitted pulse from the measured local sheet conductivity. The dashed lines at 0.761 (red) and 0.792 (blue) are for the first internally reflected pulse.

Figures 4.4a and 4.4b show directly transmitted THz waveforms through the sample before (red) and after (blue) PMMA deposition. Figures 4.4c and 4.4d show the first internally reflected THz waveform. The solid black line is the THz waveform transmitted through a bare Si substrate. Figure 4.4e shows the relative transmission spectra (the ratio of the electric field transmitted through graphene-

on-Si to that through bare Si) before (solid red line) and after (solid blue line) the PMMA deposition. The spectra are nearly flat, indicating the validity of the Drude picture. The THz-TDS results are compared with the calculated values based on the average sheet conductivity (dashed red and blue lines) for both the directly transmitted and first internally reflected pulse.

4.6 Conclusion

In conclusion, THz imaging enables non-contact probing of microscopic Drude conductivity in a large-area, single-layer graphene embedded in dielectric media. [65] Graphene samples grown by two different methods show largely different spatial inhomogeneity of the electrical conductivity. A thin PMMA film induces a slight reduction of conductivity in graphene, either through the introduction of additional scattering, a change in doping or a combination of these effects.

Understanding the response of graphene with interface effects is a key component to minimizing defects and scattering sites for THz electric properties. As we reduce these effects, we will later measure the electronic behavior under intense THz fields.

5 High-Field Terahertz Response of Single-Layer Graphene

5.1 Introduction

Graphene has attracted a great deal of attention from the scientific and industrial community since the initial demonstrations of isolated layers [30, 31, 45, 66]. Among various applications, graphene is considered a promising electronic material for high speed electronic devices because of its high carrier mobility at room temperature and its high Fermi velocity ($\sim 1/300$ of the speed of light). Experimentally, high speed graphene devices such as 300 GHz transistors and photodetectors have been demonstrated [67–70]. As the operating frequency of graphene devices goes beyond 100 GHz, it becomes crucial to understand how this material behaves in the terahertz (THz) regime. In addition, due to many unique optical properties, such as strong THz absorption of one atomic layer [62, 71] and plasmon resonances of patterned structures [72], graphene may play an important role in the so called THz gap (0.1-10 THz), where there is a need for improved sources and detectors. In a weak optical field where graphene behaves linearly, the optical properties have been studied extensively over a broad spectral range from visible to THz [73–75]. A universal optical conductivity of $\pi e^2/(2h)$ due to interband transitions is predicted and observed for photon energies less than ~ 1 eV and greater than twice the Fermi level E_F (Fermi level measured relative to the

charge neutrality point) [73]. The optical conductivity of graphene demonstrates a Drude-like frequency dependence in THz frequency range [62, 65, 75, 76].

Recent theoretical work on the high-field response of graphene indicates that the unique electronic properties of graphene lead to remarkably strong optical nonlinearities in the THz and IR regime [77–84]. The predicted strong nonlinear responses of graphene make it an attractive material for active photonic devices. Furthermore, as the internal electric field inside electronic devices could possibly reach 100 kV/cm, it is desirable to determine the maximum field at which graphene still behaves linearly. Transport in a strong field has also been studied theoretically, and nonlinear relationships between current and electric field are predicted [77–80]. Harmonic generation in graphene under a strong THz field has been predicted by several groups using different theoretical approaches [81–84]. For example, Mikhailov and Ziegler [81] analyzed the intraband contribution via the quasi-classical kinetic Boltzmann theory. In the limit of non-interaction quasiparticles, an electron gains a momentum $\mathbf{p}(t) = \frac{e\mathbf{E}_0}{\omega_0} \sin \omega_0 t$ in an oscillating electric field $\mathbf{E}(t) = \mathbf{E}_0 \cos \omega_0 t$. The electron moves in the same direction with $\mathbf{p}(t)$, yet its speed is constant, i.e. $v(t) = v_F \text{sgn}(\sin \omega_0 t)$. Accordingly, the sheet current density is expressed as $J(t) = en_{2d}v(t) = en_{2d}v_F \text{sgn}(\sin \omega_0 t)$, where n_{2d} is the sheet carrier density (see Figure 5.1). This means that a sinusoidal excitation can produce a square wave-like current, and therefore odd harmonics are generated efficiently [81]. Wright et al [82] calculated the three-photon process in intrinsic graphene from the Dirac equation, and predicted a strong frequency-tripled current. Ishikawa [83] analyzed the THz harmonic generation from the Dirac equation

by using a time domain approach. The threshold electric field to observe the nonlinear harmonic generation predicted by above works ranges approximately from 1 to 10 kV/cm [81–84], which is easily achievable in realistic devices, and in free-space THz spectroscopy.

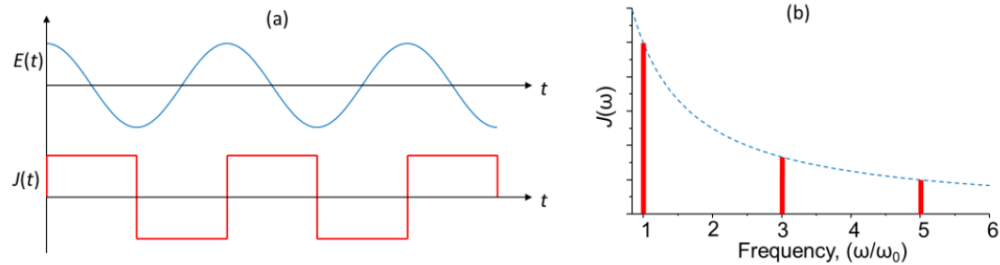


Figure 5.1: (a) Sheet current density in graphene induced by an oscillating electric field and (b) corresponding Fourier spectrum of the current density.

It is important to note that all scattering mechanisms in graphene are neglected in the theoretical works predicting harmonic generation [81–84]. In realistic graphene systems, nonlinear effects may be obscured by various scattering mechanisms. First of all, manybody Coulomb interactions in graphene are strong [85,86]. Carrier dynamics in graphene are also susceptible to defects, substrate interface interactions, and its own three-dimensional ripples [33]. Rigorous experimental studies are desirable to investigate how the intrinsic and extrinsic scatterings affect the nonlinear THz responses of graphene. Currently there are only few experiments on the high THz-field response of graphene [71, 87, 88]. Experimental observation of THz harmonic generation in graphene has not yet been reported. Dragoman et al [89] observed harmonic generation from graphene in the millimeter wave range, but the generation efficiency was extremely low. At present only a few

experiments on the high THz-field response of graphene have been reported: strong THz pulses enhance the transmission, [71, 87, 90–92] which has been attributed to increase of the electron temperature via carrier-carrier scattering. However, unlike THz-induced transparency in doped semiconductors which is caused by intervalley scattering, [93, 94] the underlying mechanisms of THz-induced transparency in graphene are largely unknown.

We present intensity dependent THz imaging and THz time-domain spectroscopy (THz-TDS) of two CVD-grown single-layer graphene samples. We demonstrate that strong THz pulses enhance transmission in graphene and the THz-induced transparency depends on spatial homogeneity of the graphene samples and the interface with its substrate. The experimental observations lead to a universal nonlinear THz property of graphene. Our study also investigates how the THz-induced transparency evolves in the time domain.

5.2 Experiment

We studied two types of CVD graphene samples, [63] one sample had uniform graphene coverage, and the other sample was inhomogeneous on the millimeter scale. We grew large-area, single-layer CVD graphene on Cu-foil via standard methods. The graphene sheets were covered with PMMA and subsequently transferred onto two types of sample mounts: PMMA/graphene-on-Si (100-nm PMMA layer; inhomogeneous graphene) Figure 5.3a and free-standing PMMA/graphene film (180-nm PMMA layer; homogeneous graphene) over 2-mm circular holes in

an aluminum plate (Figure 5.3b). Micro-Raman spectroscopy showed typical signatures of single-layer graphene [95]. The graphene layer had a p-type carrier concentration of $\cong 5 \times 10^{12} \text{ cm}^{-2}$. [96] PMMA is an uncharged polymer and contains fewer charge traps than SiO_2 , and hence the free-standing PMMA/graphene structure reduces parasitic substrate effects. THz absorption and interference in the PMMA thin films are negligible and the interface with PMMA induces little changes in the THz properties of graphene. [65]

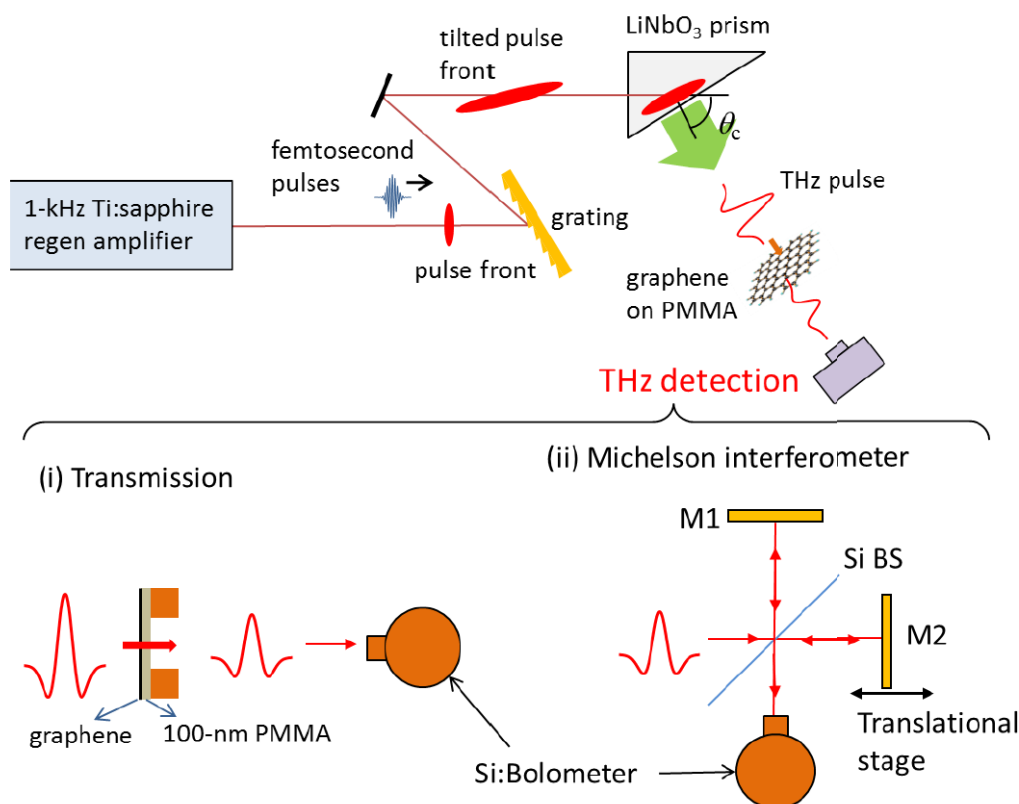


Figure 5.2: Schematic diagram of the nonlinear THz transmission measurements on CVD-grown single-layer graphene on a thin PMMA film. Strong broadband THz pulses are generated by tilted-pulse front optical rectification in LiNbO₃. Two THz detection schemes are employed: (i) spectrally integrated total THz transmitted power and (ii) transmission spectra via Michelson interferometry.

We measured THz transmission through the graphene samples using broadband THz pulses (central frequency, 1 THz; bandwidth, 1 THz), while controlling THz intensity, sample position, and delay time. The THz pulses were generated via optical rectification of femtosecond pulses with tilted pulse fronts in a MgO-doped LiNbO₃ prism (THz field amplitude reaches 1.2 MV/cm at an optical pulse energy of 0.6 mJ). [16,21,29,90,91,97] The light source was a 1-kHz regenerative amplifier

(wavelength, 800-nm; pulse energy, 1 mJ; pulse duration, 100 fs). THz pulses were focused to near diffraction limit onto the samples with parabolic mirrors (beam waist, 0.3-mm). We detected the transmitted THz pulses using a liquid-He cooled Si:Bolometer to acquire (i) spectrally integrated total THz transmitted power, (ii) transmission spectra via Michelson interferometry as shown in Figure 5.2, and (iii) THz waveforms were determined by electro-optic sampling with a 150- μm ZnTe crystal. [64]

5.3 Intrinsic Local Carrier Dynamics

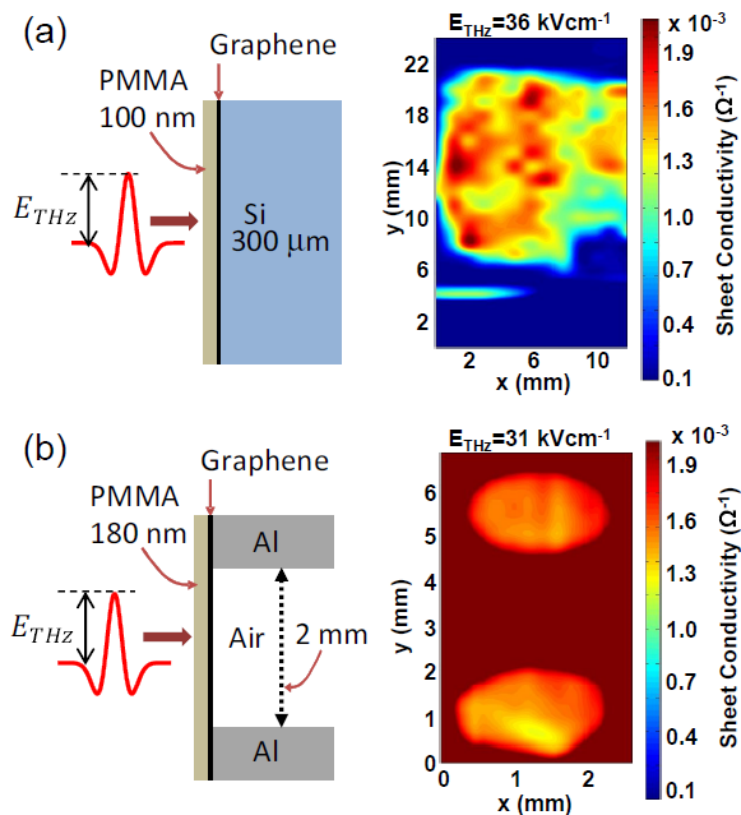


Figure 5.3: Sheet conductivity images of (a) PMMA/graphene-on-Si (inhomogeneous) and (b) freestanding PMMA/graphene (homogeneous) samples at low THz intensity ($E_{\text{THz}} \sim 30$ kV/cm). Raster images were taken over (a) 25×13 -mm² rectangle and (b) two 2-mm diameter holes with (a) 1-mm and (b) 0.2-mm pixel size. In the images, (a) the rectangular area of graphene is colored with light blue, yellow and red, and (b) the circles of graphene are colored with yellow and light red.

Figure 5.3 shows sheet conductivity (σ_S) images of the two graphene samples calculated from the THz transmission at low intensity ($E_{\text{THz}} \sim 30$ kV/cm) using the thin-film transmission coefficient for graphene on a substrate of refrac-

tive index n (Eq. 2.210) or for graphene suspended over air (Eq. 2.211). [65, 90] In Figure 5.3a, the rectangular area of light blue, yellow and red indicates the graphene-on-Si, while Si and air are colored with dark blue. In Figure 5.3b, the circular regions of yellow and light red indicate the suspended graphene. The THz absorption reaches 20% in the graphene-on-Si sample and 40% in the suspended graphene sample. This THz absorption is an order of magnitude larger than graphene's optical absorption ($\pi\alpha \cong 2.3\%$, where α is the fine structure constant), which implies that intraband transitions dominate the interactions of THz waves with graphene. [62, 65] As shown in Figure 5.3a, inhomogeneity is observed in the Si-on-graphene sample on the millimeter length scale. The sheet conductivity widely varies from 0.8 to $2.0 \times 10^3 \Omega^{-1}$. The relatively small inhomogeneity for the suspended graphene sample mainly comes from nonuniform distribution of defects over the sample. At low THz intensity, THz transmission through graphene is spectrally flat validating the simple Drude model on which the graphene sheet conductivity is based. [62]

5.4 Terahertz Induced Transparency and Normalized Conductivity

We have observed that intense THz pulses (the peak THz field E_{THz} exceeds 1 MV/cm) give rise to strong nonlinear transmission through the graphene samples. Figure 5.4a shows the spatially and temporally averaged THz transmission through the suspended graphene sample (black and red lines for bottom and top holes, respectively) versus incident peak field amplitude. The field induced effects exhibit

a threshold behavior: the transmission changes little in the low intensity region and shows an abrupt increase above 50 kV/cm. The transmission through the top hole is slightly higher than that through the bottom hole in the entire intensity range, while the differential transmission, $\Delta T/T_0 = (T - T_0)/T_0$, where T_0 is the transmission at low THz intensity, is nearly identical for both of holes (Figure 5.4b).

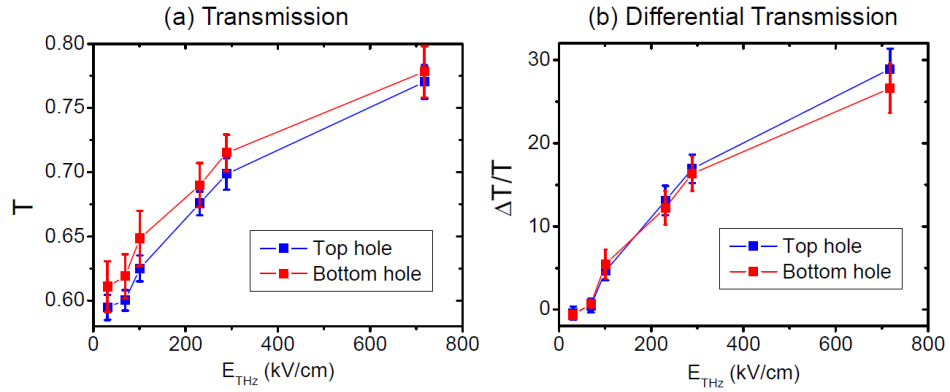


Figure 5.4: (a) Spatially and temporally averaged transmission and (b) normalized differential transmission through the top (red) and bottom (black) holes of the suspended graphene sample.

To better understand the nonlinear THz effect we compare the magnitude of THz-induced transparency to the local sheet conductivity. Figure 5.5 shows the differential transmission ($\Delta T/T_0$) images of (a) the PMMA/graphene-on-Si and (b) free-standing PMMA/graphene film. By increasing the incident THz field strength from 30 kV/cm to 800 kV/cm, we observed large enhancement in transmission ($< 15\%$ in Figure 5.5a and $\cong 30\%$ in Figure 5.5b). The image of THz-induced transparency in the graphene-on-Si sample (Figure 5.5a.iii) matches well with that

of the sheet conductivity shown in Figure 5.3a, indicating that the nonlinear THz signal is larger where the graphene growth coverage is more complete (Spot #1: completely covered; #2: almost covered; #3: partially covered). The nonlinear THz transmission of the suspended graphene sample is largely uniform and no clear spatial correlation is found between the linear and nonlinear responses. Overall the differential transmission in the suspended graphene sample ($\Delta T/T_0 \cong 30\%$ at 800 kV/cm) is significantly higher than that in the graphene-on-Si sample ($\Delta T/T_0 < 15\%$ at 800 kV/cm). This result demonstrates that suspended graphene is superior to graphene on a dielectric substrate for a device to manipulate THz signals.

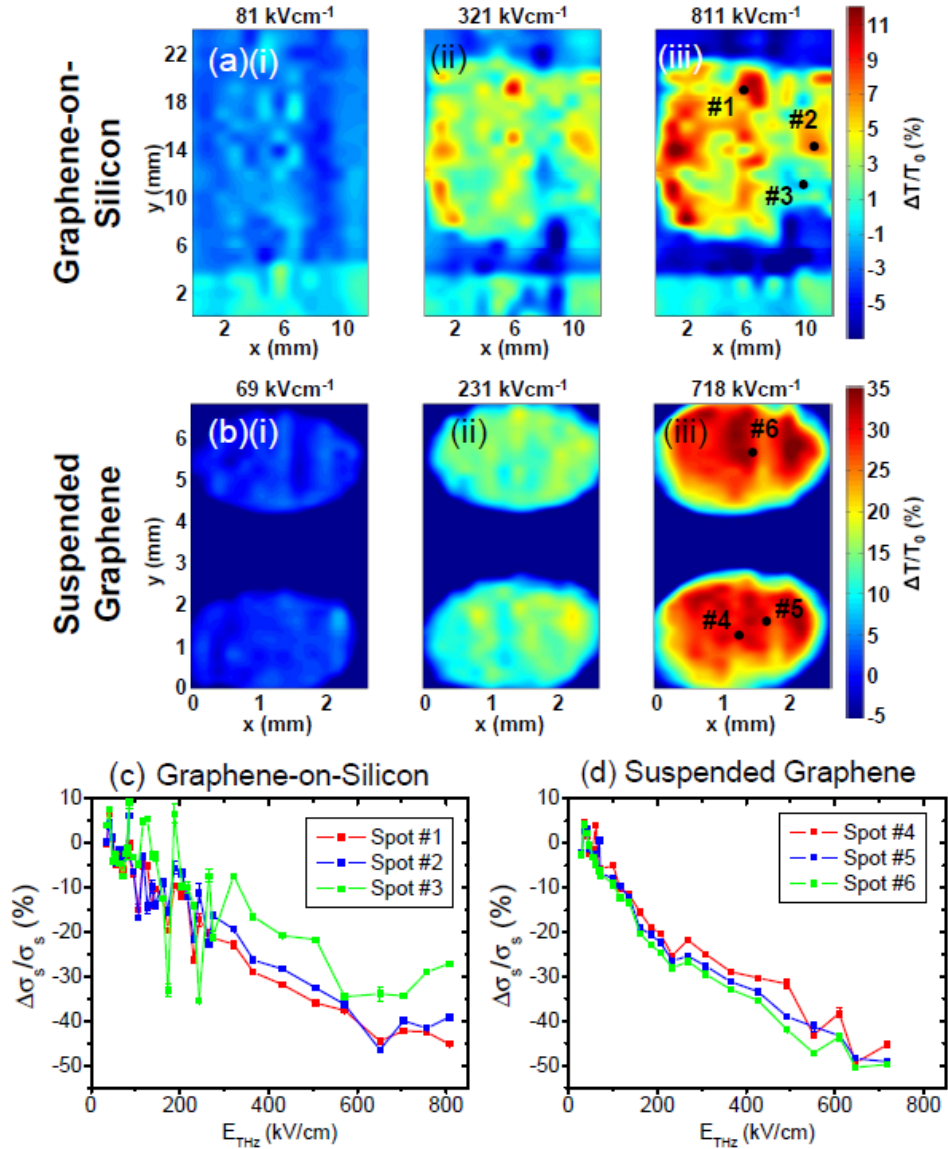


Figure 5.5: Differential transmission ($\Delta T/T_0$) images taken at $E_{\text{THz}} \cong 80, 300, 800$ kV/cm for (a) PMMA/graphene-on-Si and (b) free-standing PMMA/graphene. (c,d) Time-averaged differential sheet conductivity ($\Delta\sigma_s/\sigma_s$) at three spots on each sample. The spot locations are marked in a.iii and b.iii.

We first discuss the apparent differences between the suspended graphene and

the graphene-on-Si sample. The refractive index of the substrate affects the relationship between $t(\sigma_S)$ and σ_S (see Eq. 2.210). The transmission through the suspended graphene is more sensitive to σ_S than is the transmission through the graphene on silicon. To account for this effect, we use Eq. 2.210 and the differential transmission data to calculate changes in sheet conductivity ($\Delta\sigma_S$). The normalized change in sheet conductivity ($\Delta\sigma_S/\sigma_S$) at different spots on the samples (Spots #1 – 6 in Figures 5.5a.iii and 5.5b.iii) is plotted in Figures 5.5c and 5.5d. It is striking that this normalized nonlinear conductivity is independent of location and consistently reaches $\sim 50\%$.

Since the THz excitations should make little change in the carrier density ($\sim 5 \times 10^{12} \text{ cm}^{-2}$) for the relatively large Fermi energy ($E_F \sim 250 \text{ meV}$), the Drude model leads to

$$\frac{\Delta\sigma_S}{\sigma_S} \approx \frac{\Delta\mu}{\mu} \approx \frac{\Delta\tau}{\tau} \quad (5.1)$$

where μ is the carrier mobility and τ is the scattering time. Eq. 5.1 implies that the quantity, $\Delta\sigma_S/\sigma_S$, reveals the intrinsic nonlinear THz dynamics of individual carriers in graphene, and explains the common features shown in Figures 5.5c and 5.5d. Intense THz fields drive electrons into high momentum states far from equilibrium, and the subsequent electron-electron scattering redistribute the occupied states in the momentum space. The redistribution of the occupied states opens up more phase space for scattering with phonons and defects, and eventually reduces the conductivity. During this process, the differential scattering time ($\Delta\tau/\tau$) due to the THz excitations is solely determined by the THz field strength.

5.5 Transient Non-Equilibrium Electron Distributions

The THz-induced transparency is dynamic, and hence the Drude picture needs some corrections in the high-field regime. We obtained the temporal evolution of the transmission enhancement measuring THz waveforms transmitted through the graphene samples. Figure 5.6a shows the transmitted waveforms at different incident THz field strengths at $E_{\text{THz}} = 220, 640, \text{ and } 1320 \text{ kV/cm}$ for the suspended graphene sample. The thin gray lines indicate the incident pulse waveforms for comparison. Under low incident THz fields ($E_{\text{THz}} < 50 \text{ kV/cm}$), the graphene layers behave like a Drude metal showing flat temporal and spectral (0.5 – 1.5 THz) transmission. In the high-field regime, however, the transmission gradually rises throughout the pulse duration: the transmission is relatively low in the first peak at 1.5 ps, moderate in the main peak at 2 ps, and high in the trailing peak at 2.4 ps. As the field strength increases, the dynamical behavior becomes more pronounced. It is notable that the transient transmission of the trailing peak at 2.4 ps is close to unity at the highest THz intensity, i.e., the graphene layers become almost transparent in the high-field regime. Using these data, we acquired transient sheet conductivity at the three peaks of the waveforms. Figure 5.6b shows the temporal evolution of the sheet conductivity, monotonically decreasing as the delay time increases. At the highest intensity, the sheet conductivity reduces to $0.13 \times 10^{-3} \Omega^{-1}$ ($\Delta\sigma_S/\sigma_S \cong 90\%$) at the trailing peak. The dynamic changes in transmission give rise to the modulations in the Fourier spectra, shown in Figure 5.6c. The spectra exhibit slight blue shifts and broadening in the high field regime

due to the dynamic nonlinear THz transmission.

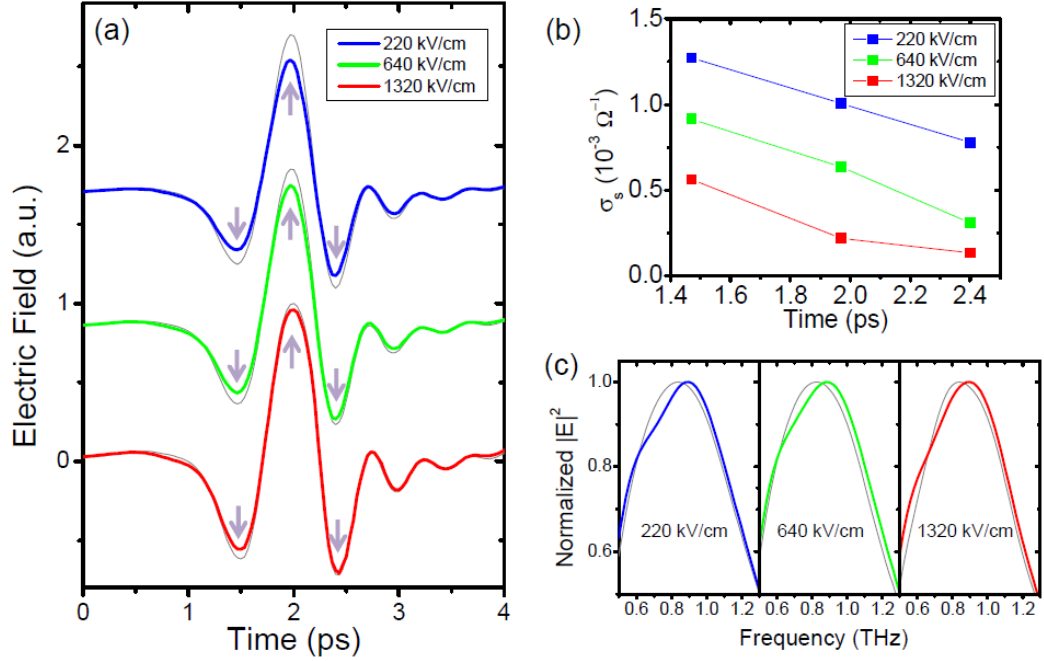


Figure 5.6: (a) THz waveforms transmitted through the suspended graphene sample. The solid colored lines represent the transmission at $E_{\text{THz}} = 220, 640,$ and 1320 kV/cm. The thin gray lines indicate incident pulse waveforms. (b) Transient sheet conductivity at the three peak positions, 1.5, 2.0, and 2.4 ps. (c) THz transmission spectra of the graphene sample (colored lines) in the high field regime obtained by Fourier transform of the transmitted THz waveforms. Reference spectra of the incident pulses are shown in gray lines. The spectra are normalized at the highest value.

5.6 Conclusion

In conclusion, intense THz fields induce transparency in graphene, transiently decreasing its conductivity. [90, 91] The nonlinear THz transmission maps out the macroscopic inhomogeneity in large-area single-layer graphene of two differ-

ent growth recipes and two different substrates. The THz-induced transparency is significantly higher in suspended graphene/PMMA membrane ($\Delta T/T_0 = 30\%$ at $E_{\text{THz}} = 800$ kV/cm) than in graphene-on-Si ($\Delta T/T_0 = 10\%$ at $E_{\text{THz}} = 800$ kV/cm). This result demonstrates that a THz device consisting of suspended graphene should be more efficient to manipulate THz signals than one with graphene on a dielectric substrate. On the other hand, the intrinsic THz nonlinearity characterized by normalized nonlinear conductivity is independent of the extrinsic sample parameters such as spatial inhomogeneity and substrate material. The nonlinear conductivity consistently reduces to 50% at $E_{\text{THz}} = 800$ kV/cm at different locations on the two different samples. Spectral measurements reveal that no harmonic generation takes place, rather, a spectral blue shift ($\delta\nu = 0.07$ THz) occurs implying sub-picosecond electron thermalization followed by subsequent carrier-carrier scattering. Time-resolved measurements show that the THz-induced transparency is a dynamic process, gradually rising throughout the pulse duration. The intense THz fields induce transparency in graphene, transiently decreasing its conductivity. At the highest intensity and at the trailing peak of the THz pulse, the sheet conductivity reduces to $\sim 10\%$ of the original conductivity. This implies that fast electron thermalization through a thermal redistribution of occupied states induces transient quasi-equilibrium modulation of the electrical and optical properties of single-layer graphene.

Our high-field measurements on suspended graphene are confined within the band structure to a discrete Fermi energy. In order to explore the high-field THz response to the graphene linear dispersion, we must conduct experiments with a

gate, thus varying the Fermi energy through the charge neutrality point. Optical excitation could lead to further band exploration and better temporal resolutions. These experiments are left to the next generation.

6 Terahertz Transmission Ellipsometry of Vertically-Aligned Multi-Walled Carbon Nanotubes

6.1 Introduction

Carbon nanotubes (CNTs) have exceptional electrical and optical properties which have inspired unique applications in nano-scale optoelectronics. [98–100] In particular, the electrodynamics of CNTs at terahertz (THz) frequencies are of great interest not only for fundamental materials research but also for practical applications such as high-speed electronics and biomedical sensing. [101–104] A CNT can behave as a semiconductor, semi-metal, or metal depending on its structure, yet in the THz band the optical responses are dominated by metallic CNTs while those from semiconducting CNTs are negligible. THz studies of CNT thin-films have shown strong responses to broadband THz radiation demonstrating their metallic nature. [105–107] Furthermore, the one-dimensional character of single-walled CNTs (SWCNTs) leads to strongly anisotropic THz absorption in aligned SWCNT films. [108, 109] Exploiting the THz anisotropy, aligned SWCNT thin-films are shown to be excellent broadband THz polarizers. [110–112]

We present a detailed study of the anisotropic electrodynamics in multi-walled CNTs (MWCNTs), utilizing free-space THz transmission ellipsometry. The anisotropic nature of MWCNTs is shown to be markedly different from that of SWCNTs be-

cause of electron transport between neighboring shells.

6.2 Experiment

We performed angle-resolved THz transmission measurements on vertically aligned MWCNTs (V-MWCNTs), simultaneously showing the THz responses along the CNT axis (z -axis) and the horizontal direction (xy -plane). A forest of vertically aligned CNTs is an ideal black material in the visible and infrared bands, absorbing light perfectly at all angles. [113, 114] Our V-MWCNT samples also show near perfect blackness by visual inspection. The perfect blackness, however, disappears in the THz region because the spacing between adjacent CNTs ($\sim 100 - nm$) is negligible compared with the wavelength of THz radiation. The V-MWCNT film responds to the THz wave like a homogeneous medium. In fact, THz absorption in the V-MWCNTs is substantial, but not perfect. The most surprising result of our observation is that the THz response perpendicular to the CNT axis is considerably strong, indicating electron transport between neighboring shells. Several theoretical studies calculating intershell conduction have produced a wide variety of results depending on the detailed conditions and assumptions of the models. [115–120] An indirect experimental observation implies weak inter-shell conductance, yet the result is inconclusive. [121] Our direct THz conductivity measurements with a non-contact THz probe clearly resolve the strong electrical conduction perpendicular to the CNT axis.

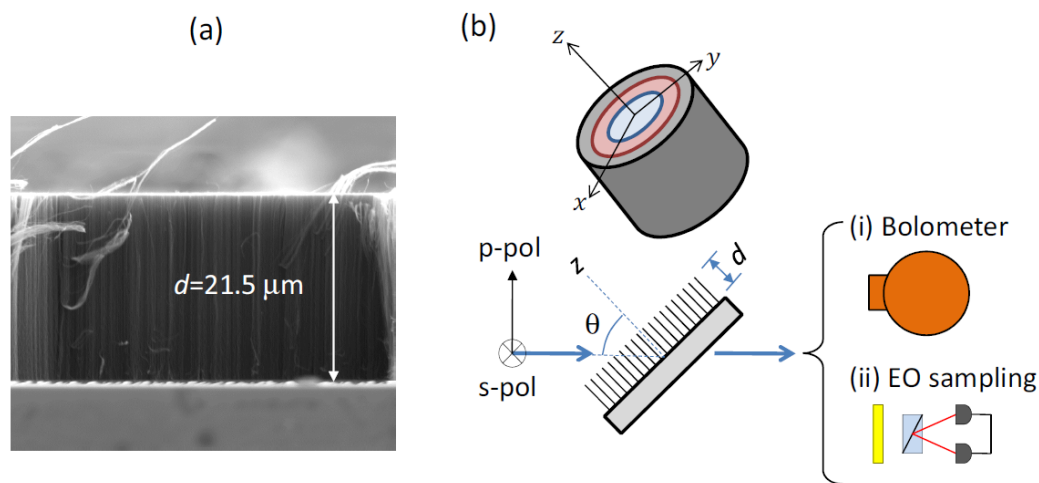


Figure 6.1: (a) SEM image of the CNT-on-Si sample for the film thickness, $d = 21.5\text{-}\mu\text{m}$. (b) Ellipsometry schematic for THz transmission measurements: linearly polarized (s-pol or p-pol), broadband pulses are incident (angle, θ) upon a V-MWCNT film on a Si substrate. THz detection schemes: (i) integrated power spectrum measured with a Si: Bolometer and (ii) THz-TDS measured with EO sampling.

The V-MWCNT samples were prepared by low-pressure chemical vapor deposition (Black Magic, AIXTRON) with 2-nm Fe on 10-nm Al_2O_3 catalyst on high-resistivity Si substrate. Individual CNTs are multi-walled, semi-metallic conductors. [39] Four samples were fabricated with varying thickness: 0- μm (no CNT deposition), 21.5- μm , 62.5- μm , and 132- μm . The CNT includes 5-15 nested cylinders, and the CNT diameter is 10-20-nm. The intershell spacing should be 0.34-0.36-nm. [122] The average spacing between neighboring CNTs is $\sim 100\text{-nm}$. Figure 6.1a shows an SEM image of the 21.5- μm thick V-MWCNT film on a Si substrate. The MWCNTs of uniform height are well-aligned in the vertical direction. We measured the angle-resolved transmission of broadband THz pulses

through the samples employing free-space THz time-domain spectroscopy (THz-TDS) which provides a non-destructive probe for local carrier dynamics of metallic thin films. [62,123] The THz pulses (central frequency, 1 THz; bandwidth, 1.5 THz) were generated via optical rectification in a 1-mm ZnTe crystal. Our femtosecond laser system is a 1-kHz Ti:sapphire amplifier (Legend, Coherent, Inc; wavelength, 800-nm; pulse energy, 1 mJ; pulse duration, 90 fs). The THz pulses were spatially-focused onto the CNT-on-Si samples with parabolic mirrors (beam size, 0.5-mm). Figure 6.1b illustrates a transmission ellipsometry schematic where the THz field is oriented parallel (perpendicular) to the plane of incidence for p-polarization (s-polarization). We measured (i) spectrally-integrated THz transmittance with a L-He cooled Si:Bolometer and (ii) time-resolved electric-field waveforms using THz-TDS under N_2 purge with the electro-optic (EO) sampling of a 150- μm ZnTe crystal. [64]

6.3 THz Power Transmission Ellipsometry

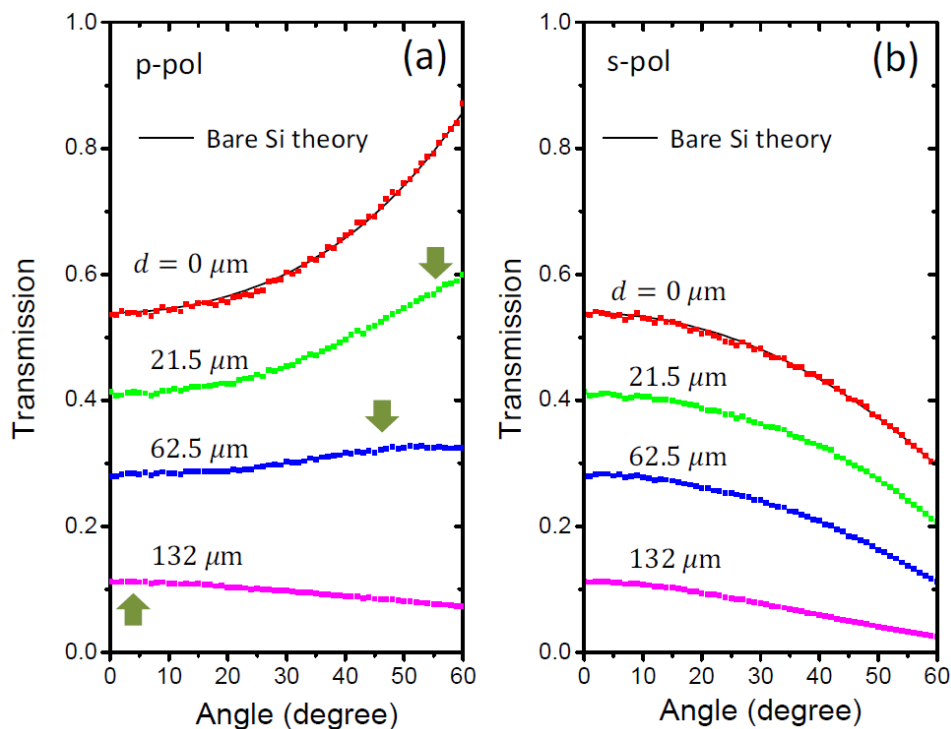


Figure 6.2: Spectrally integrated THz power transmitted through the CNT samples vs. incident angle θ for (a) p- and (b) s-polarizations. The solid black lines represent the theoretical transmission for a bare-Si substrate.

Figure 6.2 shows the spectrally-integrated THz transmission through the four samples with varying CNT length for s- and p-polarization as a function of incident angle (θ_i). Transmission through the Si substrate with a catalyst layer ($d = 0\text{-}\mu\text{m}$, red dots) is consistent with the calculation for a bare Si substrate ($n_{\text{Si}} = 3.42$, black solid lines), indicating the THz response to the catalyst layer is negligible. The s-pol transmission, depending only on the xy-conductivity, diminishes with increased thickness (skin depth $\sim 100\text{-}\mu\text{m}$) and follows the typical

trend of monotonic decrease with θ_i . The most notable feature in Figure 6.2 is that the p-pol transmission undergoes pronounced changes in curvature, depending on the film thickness. It is nearly flat, yet s-shaped for $d = 62.5\text{-}\mu\text{m}$, and monotonically decreasing for $d = 132\text{-}\mu\text{m}$ as θ_i increases. This peculiar angle dependence of the p-pol transmission implies that the V-MWCNTs anisotropically respond to the THz radiation, because p-pol transmission of multi-layer structures consisting of isotropic dielectric media monotonically increases until a large angle (typically $> 70^\circ \sim$ Brewster angle). A detailed spectral analysis utilizing THz transmission ellipsometry will confirm that the angle-dependent trends are caused by anisotropy.

6.4 Time-Resolved THz Transmission Ellipsometry

To gain more insight into the vertical and horizontal carrier dynamics of the V-MWCNT films, we performed time-resolved THz ellipsometry to obtain a time-dependent transmission function for both s- and p-polarization, $t_{s,p}(t, \theta_i)$. Figures 6.3(a-d) and 6.4(a-d) show the directly transmitted waveforms with p- and s-polarization through each CNT sample at $\theta_i = 0^\circ, 10^\circ, 20^\circ, 30^\circ, 40^\circ, 50^\circ, 60^\circ$, measured by THz-TDS. The incident-angle dependence of each transmitted waveform has been normalized to the relative power transmission to remain consistent with the power transmission measurements shown in Figure 6.2. A Fourier transform of the THz-TDS data yields the transmission spectrum, $t_{s,p}(\nu, \theta_i)$, which is compared to a uniaxial Drude-Lorentz model.

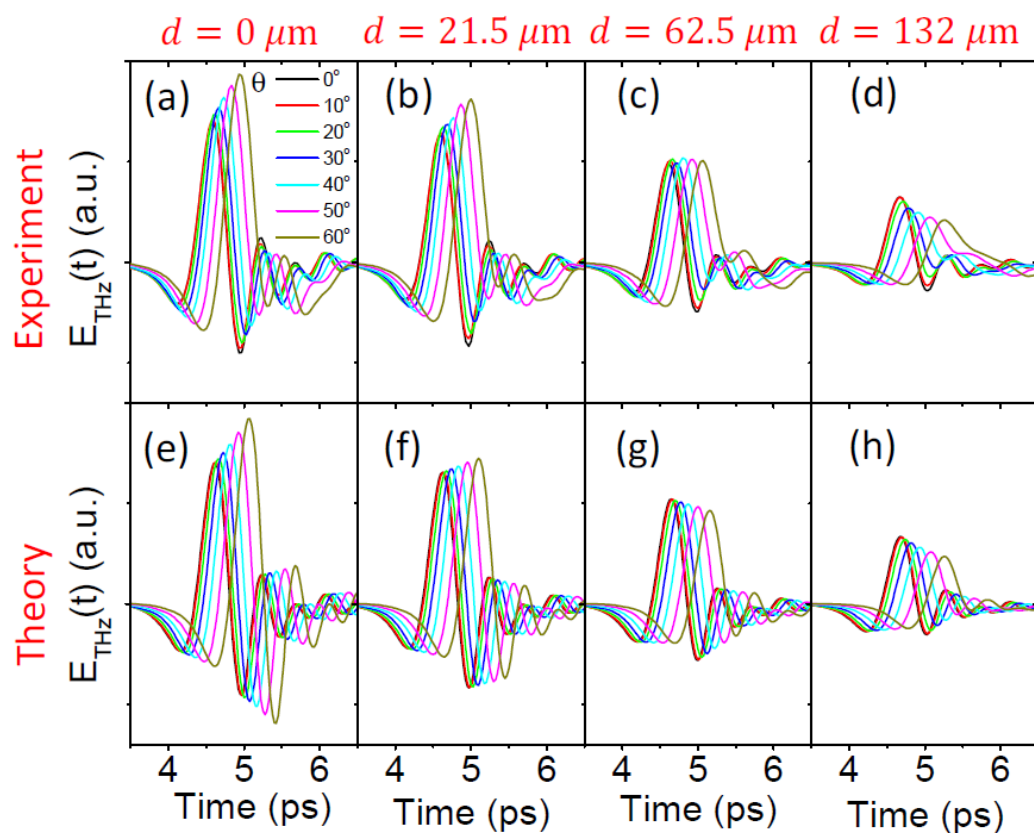


Figure 6.3: P-polarization THz waveforms transmitted through the CNT samples for incident angles between 0° and 60° (a-d) experiment and (e-h) theory.

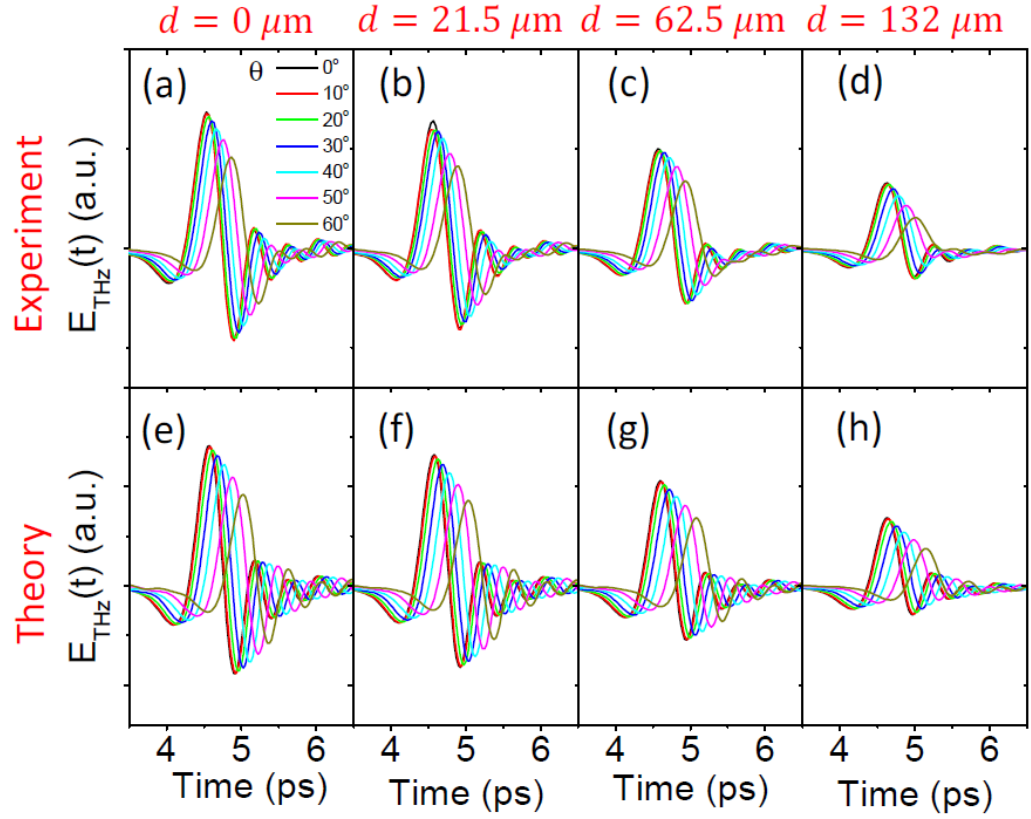


Figure 6.4: S-polarization THz waveforms transmitted through the CNT samples for incident angles between 0° and 60° (a-d) experiment and (e-h) theory.

6.5 V-MWCNT Analysis

To model the polarization dependent transmission through uniaxial anisotropic layers, we use Maxwells equations along with the continuity of electric and magnetic fields parallel to interface boundaries to obtain a transfer matrix for the amplitude coefficients $E_j^{(\pm)}$ representing the total electric-field amplitudes for forward

(+) and backward (−) moving monochromatic waves in the j^{th} material region: [124]

$$\begin{pmatrix} E_{j+1}^{(-)} \\ E_{j+1}^{(+)} \end{pmatrix} = \beta \begin{pmatrix} (1 + \kappa_j)\phi_j^- & (1 - \kappa_j)\phi_j^+ \\ (1 - \kappa_j)/\phi_j^+ & (1 + \kappa_j)/\phi_j^- \end{pmatrix} \begin{pmatrix} E_j^{(-)} \\ E_j^{(+)} \end{pmatrix} \quad (6.1)$$

where the polarization dependent parameters are

$$\beta_s = \frac{1}{2}, \beta_p = \frac{1}{2} \sec \theta_{j+1} \cos \theta_j \quad (6.2)$$

$$\kappa_j^s = \frac{k_z^{(j)}}{k_z^{(j+1)}}, \kappa_j^p = \frac{\epsilon_{xy}^{(j)} k_z^{(j+1)}}{\epsilon_{xy}^{(j+1)} k_z^{(j)}} \quad (6.3)$$

$$\phi_{j,s}^{\pm} = \exp\left\{i \frac{\omega}{c} (k_{z,s}^{(j+1)} \pm k_{z,s}^{(j)}) z_j\right\} \quad (6.4)$$

$$\phi_{j,p}^{\pm} = \exp\left\{i \frac{\omega}{c} (k_{z,p}^{(j+1)} \pm k_{z,p}^{(j)}) z_j\right\} \quad (6.5)$$

with the dispersion relations

$$\text{(p-pol)} \quad \frac{k_x^2}{\epsilon_z} + \frac{k_z^2}{\epsilon_{xy}} = \frac{\omega^2}{c^2} \quad (6.6)$$

$$\text{(s-pol)} \quad k_x^2 + k_z^2 = \epsilon_{xy} \frac{\omega^2}{c^2} \quad (6.7)$$

The transfer matrix describes the coupling between fields in the j and $j + 1$ material regions, which meet at interface position z_j . Although there are multiple transmitted exit pulses due to the internal reflections within the Si substrates, they are temporally separated and do not interfere. Only the Fourier spectrum of the

first transmitted pulse is used to model numerically the THz response, measured in experiments. Using Eq. 6.1 above, the transmission coefficient for the first exit pulse is $t = t_{\text{AirCNTSi}}t_{\text{SiAir}}$.

The vertical CNT film is modeled as a planar uniaxial dielectric material with polarization that is governed by independent damped-driven oscillator dynamics,

$$\epsilon_{\alpha} = \epsilon_{\alpha}^{\infty} - \frac{b_{\alpha}^2}{\omega^2 + i\omega\Gamma_{\alpha} - \omega_{\alpha}^2}, \alpha = xy, z \quad (6.8)$$

where $\epsilon_{\alpha}^{\infty}$ is the high frequency permittivity limit, b_{α} is proportional to the oscillator strength (or plasma frequency for metals), $\omega = 2\pi\nu$ is the applied angular frequency, $\omega_{\alpha} = 2\pi\nu_{\alpha}$ is the resonant angular frequency, and damping parameter Γ_{α} dictates the electron scattering rate.

6.6 Results

ϵ_{xy}^{∞}	Γ_{xy} (THz)	b_{xy} (THz)	ν_{xy} (THz)
1.20 ± 0.003	339 ± 106	40 ± 6	2.2 ± 0.4
ϵ_z^{∞}	Γ_z (THz)	b_z (THz)	ν_z (THz)
1.2 ± 0.2	229 ± 149	51 ± 20	0.0 ± 0.01

Table 6.1: CNT uniaxial dielectric function parameters. Averaged results from 2000 independent Nelder-Mead search algorithm starting locations and their corresponding standard deviation.

The oscillator parameters were extracted by minimizing the difference between the measured and modeled blank-normalized transmitted intensity spectrum using a Nelder-Mead nonlinear least squares algorithm. [125–127] All CNT lengths were fit simultaneously. First, s-polarized data was used to extract ϵ_{xy} parameters, then ϵ_z parameters were extracted using both p-polarized experimental data and the ϵ_{xy} result. This process was performed over the FWHM of the incident electric-field spectrum (0.4-1.6 THz). The results for the oscillator parameters are listed in Table 1. The z-axis parameter $\nu_z = 0$ indicates that CNT-axis conduction is purely due to free charge carriers, while the non-vanishing xy-plane resonant frequency ($\nu_{xy} = 2.2$ THz) implies that intershell conduction is not Drude-like, but undergoes shallow potential barriers. Using the oscillator parameters, and assuming a Fermi-velocity along the MWCNT-axis, $v_F = 8 \times 10^5$ m/s, [128] we estimate the average electron scattering mean free path in the z-direction to be 3.5 ± 1.4 nm, comparable to typical scattering lengths in metals at room temperature. The Fermi-velocity in the xy-direction is not known, but should be less than 8×10^5 m/s due to the weaker coupling between electron orbitals in different shells of the MWCNT. Using this upper bound on radial velocity, we predict that the average electron scattering mean free path in the xy-direction is less than 2.4 ± 0.6 nm, much less than the typical MWCNT diameter (1020-nm). These estimates indicate that Drude-like conduction (with anisotropic scattering parameters) can be expected, which is consistent with the parameters in Table 6.1.

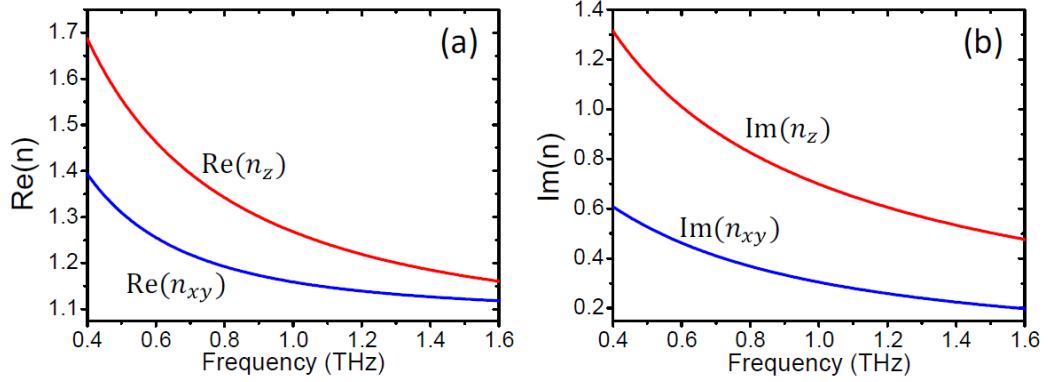


Figure 6.5: (a) Real and (b) imaginary parts of the refractive index for all CNT films at THz frequencies.

Figure 6.5 shows the real and imaginary components of n_{xy} and n_z spectra. The anisotropic nature of the THz properties of the V-MWCNTs is evident, yet the ratio of the z-axis conductivity to the xy-plane conductivity ($\sigma_z/\sigma_{xy} \cong 2.3$, which is nearly constant over the broad spectral range, 0.4-1.6 THz) is significantly smaller than that of a SWCNT. The ratio of the V-MWCNTs is even smaller than that of graphite, $\sigma_z/\sigma_{xy} \cong 4.2$. [129] The relatively weak anisotropy of the V-MWCNT samples indicates that THz fields can readily induce electron transport between neighboring shells.

The theoretical transmission spectra, $t_{\text{tot}}(\nu, \theta_i)$, is used along with the incident THz electric-field spectrum in air, $a(\nu)$, to perform an inverse Fourier transform to model the time-domain THz pulses,

$$\tilde{E}(t, \theta_i) = \text{Re} \left[\sum_{\omega} a(\omega) t_{\text{tot}}(\omega, \theta_i) e^{i(kz_0 - \omega t)} \right] \quad (6.9)$$

where $t_{\text{tot}}(\omega, \theta_i)$ contains all the optical path length phase information for the Air-

CNT-Si-Air system, and z_0 is the measurement position. Theory results are shown in Figures 6.3(e-h) and 6.4(e-h) and are consistent with experimental data [Figures 6.3(a-d) and 6.4(a-d)].

The experiment and theory results show that (i) the THz response along the z-axis is stronger than that of the xy-plane, yet the anisotropy is much weaker compared with that of an isolated, metallic SWCNT, (ii) strong absorption in the horizontal direction indicates that charge carriers transport between adjacent shells, and (iii) the z-axis THz response of MWCNTs is not overwhelmingly metallic in contrast to that of SWCNTs. Intershell charge transports instigate scattering sites within the multi-shell structure, reducing the effective scattering length dramatically along the z-direction and introducing a significant decrease in absorption.

6.7 Conclusion

In conclusion, time-resolved THz transmission ellipsometry reveals the anisotropic carrier dynamics in vertically aligned MWCNTs. [130] The conductivity along the z-axis is larger than the xy-plane, but they are the same order of magnitude. The considerably strong THz response along the xy-plane indicates that charge carrier transport occurs between neighboring shells in MWCNTs, also creating a non-negligible reduction in absorption along the length of the nanotubes. The THz ellipsometry method will also be useful to understand carrier dynamics in other nanomaterials consisting of novel two-dimensional conductors such as multilayer

graphene, where transport anisotropy is expected, yet is hard to measure with conventional electrode techniques.

The next generation of experiments is to control the CNTs with strong THz fields. Reel-wound suspended CNTs exhibit polarizer-like behavior to THz radiation. Under strong fields, however, their material properties change. Optical excitation will lead to band structure exploration in the THz regime as well as the potential for nonlinearities measurements on the sub-picosecond time scale.

7 Terahertz Field Enhancement and Terahertz Absorption in Intrinsic GaAs via Plasmonic Nano Antennas

7.1 Introduction

Terahertz (THz) spectroscopy of carrier dynamics in semiconductors is of great interest not only for understanding the fundamental physical processes such as many-body Coulomb interactions and carrier-phonon scattering but also for developing high-speed electronic devices. [131] In particular, recent technical advances in high-power THz pulse generation have opened up new opportunities to explore high-field electron transport and non-equilibrium carrier distribution in semiconductors. [132,133] The interaction of strong THz pulses with semiconductors results in pronounced nonlinear THz responses in that hot electrons driven by intense THz fields undergo scattering processes of different kinds such as intervalley scattering and impact ionization. [134–136] The nonlinear THz properties are governed by various physical parameters such as bandgap energy, temperature, carrier type, carrier density, and doping level.

GaAs, the material of interest in this study, is of great importance because of the fundamental interests in high-frequency carrier dynamics as well as the applications to ultra-high speed electronics. [137–140] The previous studies on n-type GaAs with the THz fields in the range of ~ 100 kV/cm show that the electrons driven into

high momentum states by the THz fields undergo distinctive intraband processes such as intervalley scattering, [93, 94] coherent ballistic transport, [141, 142] and effective mass anisotropy. [143] It is notable that the intervalley scattering from initial conduction band valley (Γ valley) to side valleys (L valley or X valley) is considered to be the dominant mechanism for the THz induced transparency in the n-type GaAs samples of the electron density around 10^{15} - 10^{17} cm^{-3} due to the lower electron mobility in the side valleys. In the higher field regime beyond 1 MV/cm, THz fields may produce extreme nonlinear effects involving interband transitions in GaAs, while the THz photon energy is several hundred times lower than the bandgap energy. [136, 144]

For example, it has been reported that THz excitations generated photoluminescence in GaAs quantum wells (QWs), which was associated with carrier multiplication through a series of impact ionizations. [136]

7.2 Experiment

We demonstrate that the field enhancement in plasmonic THz nano-antennas raises the near-field amplitude up to 20 MV/cm and hence gives rise to the onset of extraordinary nonlinear THz absorption in intrinsic GaAs associated with carrier generation by THz excitations. THz photon energy is orders-of-magnitude smaller than the bandgap energy, yet the THz electric fields are so strong that they create free carriers in the conduction band via interband transitions. We used the undoped samples to suppress intraband processes such as intervalley scattering.

Nonlinear optical processes in metal-semiconductor hybrid nanostructures hold potential for practical applications such as active switching devices, modulators, and frequency filters. [145–147] Especially, nanometer-width slot antenna structures, which are simple and easy to fabricate, can make huge field enhancement more than 100 times at the resonance frequency. [148–151] The field enhancement and consequent nonlinear optical effects in nano-slot antenna/semiconductor composites give rise to effective dielectric constant modulation. [147, 152] We exploit the field enhancement in THz nano-slot antennas to obtain intense THz fields up to 20 MV/cm and to investigate high-field transient carrier dynamics in intrinsic GaAs.

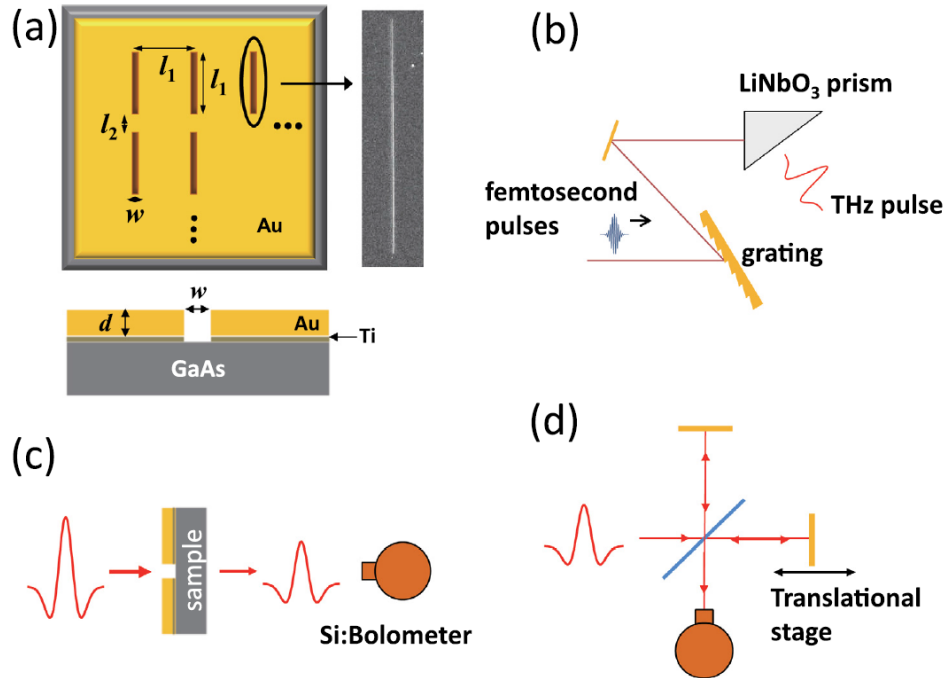


Figure 7.1: (a) Nano-slot-antenna-array patterned GaAs sample: the dimensions are $l_1 = 60\text{-}\mu\text{m}$, $l_2 = 10\text{-}\mu\text{m}$, and $w = 200\text{-nm}$. The thickness of the gold layer is $d = 100\text{-nm}$ and the adhesion titanium layer is 3-nm . A SEM image of a single nano-antenna is shown. (b) Schematic of the high-power THz pulse generation setup with a lithium niobate prism. (c) Total transmitted power measurement with a liquid-helium-cooled bolometer. (d) Michelson interferometer setup for frequency spectrum measurement.

We fabricated nano-slot-antenna arrays on a $500\text{-}\mu\text{m}$ -thick, single crystal intrinsic (100) GaAs wafer, using an electron beam lithography technique. The resistivity of GaAs wafer is $(1.0\text{-}2.9) \times 10^8 \text{ }\Omega\text{-cm}$, the mobility is $(5.5\text{-}6.2) \times 10^3 \text{ cm}^2/\text{V s}$, and the average carrier density is $\sim 7 \times 10^6 \text{ cm}^{-3}$ at room temperature. Figure 7.1a illustrates the nano-antenna/GaAs composite design: each antenna is $60\text{-}\mu\text{m}$ long (l_1) and 200-nm wide (w), which is resonant at 0.9 THz . The antenna

array is a negative structure in a 100-nm-thick-gold/3-nm-thick-Ti-adhesion layer on top of the GaAs wafer. In order to optimize the field enhancement at the resonance frequency and to avoid coupling effects among neighboring antennas, the periodicity of the antenna array in the length direction ($70\text{-}\mu\text{m}$) and width direction ($60\text{-}\mu\text{m}$) is the same scale with the antenna length (l_1). [153] The total array area, 2-mm by 2-mm, is substantially larger than the incident THz beam size at the focal plane ($400\text{-}\mu\text{m}$ diameter). We generate strong THz pulses via tilted-pulse-front optical rectification in a LiNbO₃ prism using femtosecond pulses (pulse duration, 120 fs; wavelength, 800-nm) from a 1-kHz Ti:Sapphire regenerative amplifier (Figure 7.1b). [29] The field amplitude of the broadband THz pulses (central frequency, 0.9 THz; bandwidth, 0.8 THz) reaches 500 kV/cm at an optical pulse energy of 0.8 mJ. We measured the transmitted THz pulses using a liquid-helium-cooled silicon-bolometer to obtain either spectrally integrated total transmitted power (Figure 7.1c) or transmission frequency spectra via Michelson interferometry (Figure 7.1d). We carried out the THz transmission measurements on the nano-antenna/GaAs composite as well as a bare GaAs wafer for comparison.

7.3 Field-Dependent THz Transmission through Bare High-Resistivity Intrinsic GaAs

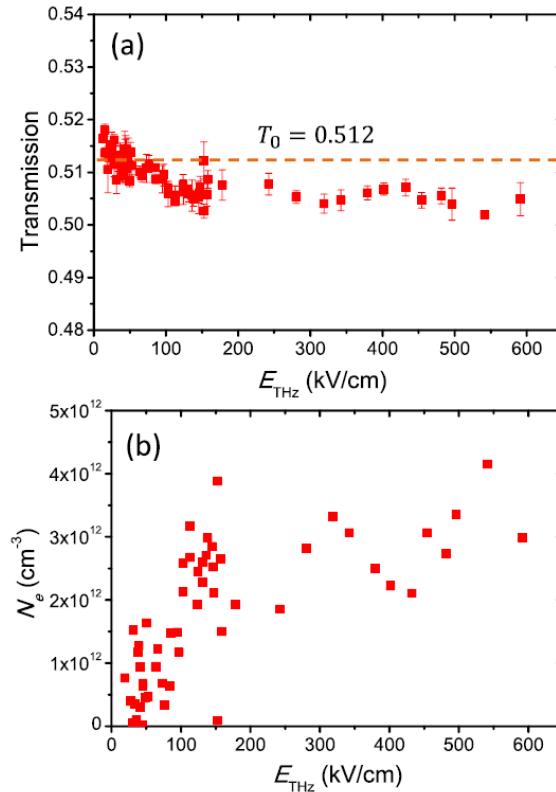


Figure 7.2: Bare GaAs wafer: (a) spectrally integrated THz transmission vs. field amplitude for the field aligned along (110) direction. The dashed line at 0.512 indicates the low-field transmission of the GaAs wafer ($n_G = 3.6$) including internal reflections. (b) Estimated free carrier density vs. THz field amplitude.

The experimental results for the bare GaAs sample are shown in Figure 7.2, where the THz transmission is the transmitted power through the sample divided by the transmitted power in the absence of a sample. Figure 7.2a shows the transmission as a function of the THz field amplitude, when the field is aligned

along (110) direction. We also obtained nearly identical results in (100) direction. The THz transmission undergoes only a small decrease up to 150 kV/cm and becomes flattened, which is independent of the field direction relative to the crystal axis. The normalized transmission decrease ($\Delta T/T_0$) is less than 1.5% in this field range of $E_{\text{THz}} < 600$ kV/cm. Though the increase in THz absorption implies free carrier generation by the THz excitation, it is hard to expect drastic carrier density changes in bare GaAs. Figure 7.2b shows the electron density N_e estimated from the free-carrier absorption coefficient,

$$\gamma(E_{\text{THz}}) = \frac{e\mu_e}{c\epsilon_0 n_G} N_e(E_{\text{THz}}) = \frac{1}{l_G} \ln \frac{T_0}{T(E_{\text{THz}})} \quad (7.1)$$

where T_0 ($= 0.512$) is the linear THz transmission of the GaAs wafer, l_G ($= 500$ - μm) is the wafer thickness, e is the electron charge, μ_e ($\cong 6 \times 10^3$ $\text{cm}^2/\text{V s}$) is the mobility, c is the speed of light, and n_G ($= 3.6$) is the GaAs refractive index in the THz region. The electron density gradually builds up to 3×10^{12} cm^{-3} and becomes saturate above 150 kV/cm. The THz field lower than 600 kV/cm is too weak to induce interband transitions either by Zener tunneling or by impact ionization. [136] We speculate that the THz excitations free up electrons trapped in shallow impurity states.

7.4 Field-Dependent THz Transmission through High-Resistivity Intrinsic GaAs with Plasmonic Nano-Antenna Array

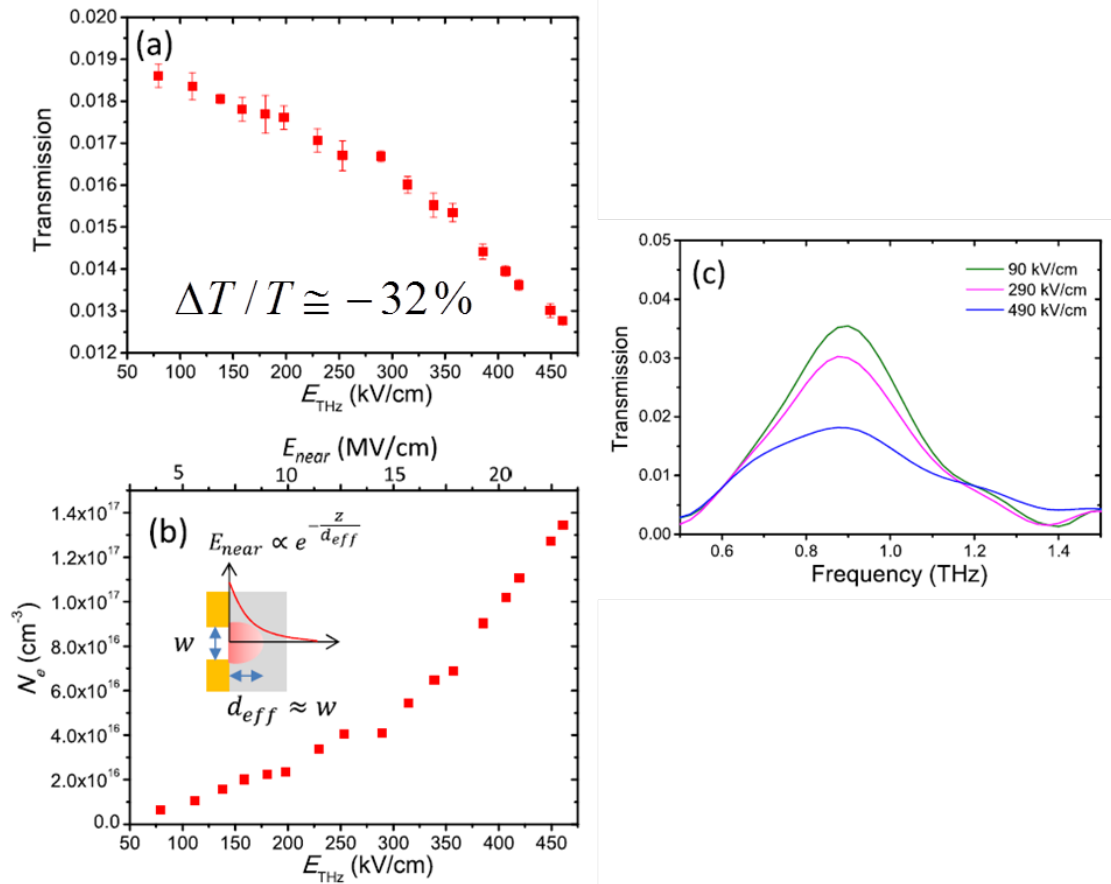


Figure 7.3: Nano-antenna/GaAs composite: (a) spectrally integrated THz transmission vs. field amplitude. (b) Free carrier density vs. THz field. (c) Transmission spectra at 90, 290, and 490 kV/cm.

Figure 7.3 shows the experimental results for the nanoantenna-array-patterned GaAs sample. For the transmitted power measurements as shown in Figure 7.3a, the transmission decreases by more than 35% over a factor-of-ten increase in the

field strength. The significant change in the THz transmission implies that the strong THz fields generate a substantially large number of free carriers via inter-band transitions. As depicted in Figure 7.3b, the carrier density is enhanced by a factor of $\sim 10^5$ compared to that in bare GaAs for the same input intensities. The transmission spectra shown in Figure 7.3c reveal the antenna resonance at 0.9 THz and also demonstrate large increase in absorption at high THz fields. The transmission reduction at 490 kV/cm at the resonance frequency compared to that at 90 kV/cm reaches 50%. Furthermore, the spectral broadening indicates the increase of conductivity and thus free-carrier generation by the THz fields.

7.5 Analysis

As the first step of a phenomenological analysis, we calibrate the THz field amplitude at the nano-slot (the near field amplitude, E_{near}) using the field enhancement factor of the nano-antenna structure. [148]

$$\alpha = \left| \frac{E_{\text{near}}}{E_{\text{THz}}} \right| = \frac{1}{\beta} \left| \frac{E_{\text{far}}}{E_{\text{THz}}} \right| \cong 50 \quad (7.2)$$

where the antenna coverage ratio β is 1/350 for this sample. The ratio of the far-field to the incident field amplitude ($E_{\text{far}}/E_{\text{THz}}$) is obtained from the observed THz transmission at low intensities (the transmission is 1.9% and the ratio of the pulse duration of transmitted radiation to that of incident radiation is 2.3). The near-field amplitude exponentially decays along the direction perpendicular

to the antenna/GaAs interface, i.e., $E_{\text{near}}(z) \approx E_{\text{near}}(0)e^{-z/w}$, which indicates that the large nonlinear THz absorption arises mostly in the confined region of the nanometer-scale layer, $d_{\text{eff}} \approx w = 200\text{-nm}$. [147]

The effective thickness is a mere 1/1500th of the wafer thickness, meaning that the nonlinear effects in the nanoantenna structure are several orders of magnitude stronger than those in bare GaAs. As a first-order approximation to analyze the nonlinear THz absorption, we treat the nanometerscale layer as a conducting thin film and apply the thin-film Fresnel formula to obtain the THz induced conductivity from the nonlinear transmission measurements. The THz-field induced conductivity is expressed as a function of the normalized nonlinear transmission, $T_{\text{rel}}(E_{\text{THz}}) = T(E_{\text{THz}})/T_0$:

$$\sigma(E_{\text{THz}}) = \frac{n_G + 1}{Z_0 d_{\text{eff}}} \left[\frac{1}{\sqrt{T_{\text{rel}}(E_{\text{THz}})}} - 1 \right] \quad (7.3)$$

where Z_0 ($= 376.7\Omega$) is the vacuum impedance. We estimate the free electron density from the conductivity, applying the mobility-conductivity relation: $N_e(E_{\text{THz}}) = \sigma(E_{\text{THz}})/e\mu_e$. The calculated electron density is shown in Figure 7.3b as a function of the incident THz field amplitude (the near field amplitude is scaled on the top axis). This simple approximation underestimates the carrier density because the electron mobility decreases as the carrier density increases in the high density regime. Nevertheless, the estimated carrier density exceeds 10^{17} cm^{-3} for $E_{\text{THz}} > 400 \text{ kV/cm}$. In this high field regime, the most probable carrier generation mechanism is the carrier multiplication by impact ionization. [136, 154, 155]

The initial electron density in the conduction band is $N_0 \sim 7 \times 10^6 \text{ cm}^{-3}$, and thus the number of impact ionizations, $n_I = \log_2 N_e/N_0$, is estimated as 33-37 for $E_{\text{near}} = 5 - 20 \text{ MV/cm}$. An alternative carrier generation mechanism is Zener tunneling, which would be appreciable above $\sim 10 \text{ MV/cm}$. [156] More detailed studies are desirable to unveil the microscopic origins of the THz excited carriers.

7.6 Conclusion

In summary, our experimental study demonstrates that strong THz pulses induce nonlinear THz absorption in intrinsic GaAs ($n \sim 7 \times 10^6 \text{ cm}^{-3}$). [97] The huge field enhancement in the nano-antenna array, $\alpha \cong 50$, produces THz fields exceeding 20 MV/cm adjacent to the antennas. The strong fields induce remarkably large THz absorption ($> 35\%$) by generating free carriers of high density ($> 10^{17} \text{ cm}^{-3}$) via interband excitations associated with impact ionizations ($n_I \sim 33 - 37$). The experimental scheme exploiting the nano-antenna field enhancement is versatile for nonlinear THz spectroscopy and can be applied to a variety of materials.

Plasmonic nano-antennas are limited to the fabrication resolution. As the nano-slit gets narrower, the field enhancement grows. Further field enhancement allows for the exciting exploration of extreme nonlinear dynamics. The future THz measurements with plasmonic nano-antennas are limited only to the threshold of destruction of measured devices.

8 Summary

In summary, we utilized low-field and high-field THz radiation to examine linear and nonlinear electronic properties in carbon nanomaterials and semiconductor nanostructures. Low-intensity THz pulses were used as a non-contacting, non-destructive probe for local carrier dynamics and macroscopic spatial homogeneity of single-layer graphene embedded in dielectrics. Graphene, even when embedded within protective dielectric layers, still exhibits large THz absorption ($\sim 20\%$) allowing THz transmission imaging to become a groundbreaking method to determine local carrier dynamics including local sheet conductivity of single-layer graphene on the sub-millimeter scale. THz transmission ellipsometry was used to characterize the THz electrodynamics of a uniaxial V-MWCNT forest. The V-MWCNT forest was shown to have a metallic response along the length of the CNT growth, which was expected, and a strong optical response orthogonal to the length of the CNT growth, which was unexpected. The nanotubes are only ~ 10 -nm in diameter and the calculated transverse scattering length was calculated to be within the diameter of the nanotubes (< 2.4 -nm). The strong transverse electrical conduction ($\sigma_z/\sigma_{xy} = 2.3$) indicates that THz fields induce electron transport through shallow potential wells between adjacent shells of the multi-walled CNT structure.

A method of generating high-intensity, broadband, single-cycle THz pulses was

developed by the use of optical rectification of femtosecond optical pulses with tilted pulse fronts in a lithium niobate prism. The strong fields were used to explore nonlinearities in graphene suspended with PMMA over 2-mm diameter holes. Utilizing a THz transmission geometry, intensity-dependent measurements revealed THz-induced transparency through the suspended graphene film with THz power transmission increasing monotonically with increased THz field strength ($\Delta T/T_0 \cong 30\%$). Theoretical models predict odd harmonic generation due to a square-wave current stemming from the linear dispersion relation of single-layer graphene. However, frequency dependent measurements reveal that no harmonic generation occurs, rather a spectral blue shift ($\delta\nu = 0.07$ THz). The spectral washing out of harmonic generation is attributed to sub-picosecond electron thermalization and subsequent carrier-carrier scattering. Further time-dependent measurements reveal a dynamic THz-induced transparency as the transparency grows throughout the duration of the transmitted THz pulse, transiently modulating the electrical properties of graphene. The intense THz fields induce transparency in graphene, transiently decreasing its conductivity. At the highest intensity, at the trailing peak of the THz pulse, the sheet conductivity reduces to $\sim 10\%$ of the original conductivity. Nonlinear THz imaging reveals that the nonlinear conductivity of two types of graphene samples consistently reduce to 50% across various locations of both large-area graphene samples.

Extreme nonlinear THz response in high-resistivity, intrinsic GaAs ($n \sim 7 \times 10^6 \text{ cm}^{-3}$) was measured through huge field enhancements utilizing a plasmonic nano-antenna array. The field enhancement reaches $\alpha \cong 50$ in the near field

($E_{\text{THz}} > 20$ MV/cm) which induces remarkably large THz absorption ($> 35\%$) by generating free carriers of high density ($> 10^{17}$ cm $^{-3}$) via interband excitations associated with impact ionizations ($n_I \sim 33 - 37$). Extremely large THz fields generate high-energy interband excitations and an enormous amount of free carriers in an intrinsically high-resistivity GaAs wafer; transitioning the intrinsically non-absorbing semiconductor into a strong absorber of THz radiation.

Bibliography

- [1] J. Jackson, *Classical Electrodynamics, 3rd Ed.* Wiley, 1998.
- [2] D. Griffiths, *Introduction to Electrodynamics, 3rd Ed.* Addison-Wesley, 1999.
- [3] E. Hecht, *Optics, 4th Ed.* Addison-Wesley, 2001.
- [4] R. Boyd, *Nonlinear Optics, 3rd Ed.* Academic Press, 2008.
- [5] Y.-S. Lee, *Principles of Terahertz Science and Technology, 3rd Ed.* Springer, 2009.
- [6] Q. Wu and X.-C. Zhang, “Ultrafast electro-optic field sensors,” *Applied Physics Letters*, vol. 68, no. 12, p. 1604, 1996.
- [7] J. R. Danielson, a. D. Jameson, J. L. Tomaino, H. Hui, J. D. Wetzel, Y.-S. Lee, and K. L. Vodopyanov, “Intense narrow band terahertz generation via type-II difference-frequency generation in ZnTe using chirped optical pulses,” *Journal of Applied Physics*, vol. 104, no. 3, p. 033111, 2008.
- [8] D. H. Jundt, “Temperature-dependent Sellmeier equation for the index of refraction, n_e, in congruent lithium niobate,” *Optics Letters*, vol. 22, p. 1553, Oct. 1997.
- [9] D. Grischkowsky, S. r. Keiding, M. V. Exter, and C. Fattinger, “Far-infrared time-domain spectroscopy with terahertz beams of dielectrics and semiconductors,” *Journal of the Optical Society of America B*, vol. 7, p. 2006, Oct. 1990.
- [10] J. Dai, J. Zhang, W. Zhang, and D. Grischkowsky, “Terahertz time-domain spectroscopy characterization of the far-infrared absorption and index of refraction of high-resistivity, float-zone silicon,” *Journal of the Optical Society of America B*, vol. 21, no. 7, p. 1379, 2004.
- [11] T. Feurer, N. S. Stoyanov, D. W. Ward, J. C. Vaughan, E. R. Statz, and K. A. Nelson, “Terahertz Polaritonics,” *Annual Review of Materials Research*, vol. 37, pp. 317–350, Aug. 2007.

- [12] M. Volk, Tatyana, Wöhlecke, *Lithium Niobate: Defects, Photorefraction and Ferroelectric Switching*. Springer, 2009.
- [13] B. B. Hu, X.-C. Zhang, D. H. Auston, and P. R. Smith, “Free-space radiation from electro-optic crystals,” *Applied Physics Letters*, vol. 56, no. 6, p. 506, 1990.
- [14] A. G. Stepanov, J. Hebling, and J. Kuhl, “Efficient generation of subpicosecond terahertz radiation by phase-matched optical rectification using ultrashort laser pulses with tilted pulse fronts,” *Applied Physics Letters*, vol. 83, no. 15, p. 3000, 2003.
- [15] A. G. Stepanov, J. Hebling, and J. Kuhl, “Generation, tuning, and shaping of narrow-band, picosecond THz pulses by two-beam excitation,” *Optics Express*, vol. 12, no. 19, p. 4650, 2004.
- [16] A. G. Stepanov, J. Kuhl, I. Z. Kozma, E. Riedle, G. Almási, and J. Hebling, “Scaling up the energy of THz pulses created by optical rectification,” *Optics Express*, vol. 13, p. 5762, Apr. 2005.
- [17] J. R. Danielson, N. Amer, and Y.-s. Lee, “Generation of arbitrary terahertz wave forms in fanned-out periodically poled lithium niobate,” *Applied Physics Letters*, vol. 89, no. 21, p. 211118, 2006.
- [18] K.-L. Yeh, M. C. Hoffmann, J. Hebling, and K. A. Nelson, “Generation of 10 μ J ultrashort terahertz pulses by optical rectification,” *Applied Physics Letters*, vol. 90, no. 17, p. 171121, 2007.
- [19] K.-l. Yeh, J. Hebling, M. C. Hoffmann, and K. A. Nelson, “Generation of high average power 1kHz shaped THz pulses via optical rectification,” *Optics Communications*, vol. 281, pp. 3567–3570, July 2008.
- [20] J. Hebling, K.-l. Yeh, M. C. Hoffmann, B. Bartal, and K. A. Nelson, “Generation of high-power terahertz pulses by tilted-pulse-front excitation and their application possibilities,” *Journal of the Optical Society of America B*, vol. 25, p. B6, Apr. 2008.
- [21] M. Jewariya, M. Nagai, and K. Tanaka, “Enhancement of terahertz wave generation by cascaded $\chi^{(2)}$ processes in LiNbO₃,” *Journal of the Optical Society of America B*, vol. 26, p. A101, July 2009.

- [22] J. A. Fülöp, L. Pálfalvi, G. Almási, and J. Hebling, “Design of high-energy terahertz sources based on optical rectification.,” *Optics express*, vol. 18, pp. 12311–27, June 2010.
- [23] Z. Chen, X. Zhou, C. A. Werley, and K. A. Nelson, “Generation of high power tunable multicycle terahertz pulses,” *Applied Physics Letters*, vol. 99, no. 7, p. 071102, 2011.
- [24] J. A. Fülöp, L. Pálfalvi, S. Klingebiel, G. Almási, F. Krausz, S. Karsch, and J. Hebling, “Generation of sub-mJ terahertz pulses by optical rectification.,” *Optics letters*, vol. 37, pp. 557–9, Feb. 2012.
- [25] S.-W. Huang, E. Granados, W. R. Huang, K.-h. Hong, L. E. Zapata, and F. X. Kärtner, “High conversion efficiency, high energy terahertz pulses by optical rectification in cryogenically cooled lithium niobate.,” *Optics letters*, vol. 38, pp. 796–8, Mar. 2013.
- [26] O. Gayer, Z. Sacks, E. Galun, and A. Arie, “Temperature and wavelength dependent refractive index equations for MgO-doped congruent and stoichiometric LiNbO₃,” *Applied Physics B*, vol. 91, pp. 343–348, Apr. 2008.
- [27] J. A. Fülöp, L. Pálfalvi, M. C. Hoffmann, and J. Hebling, “Towards generation of mJ-level ultrashort THz pulses by optical rectification.,” *Optics express*, vol. 19, pp. 15090–7, Aug. 2011.
- [28] L. Pálfalvi, “Nonlinear refraction and absorption of Mg doped stoichiometric and congruent LiNbO₃,” *Journal of Applied Physics*, vol. 95, no. 3, p. 902, 2004.
- [29] H. Hirori, A. Doi, F. Blanchard, and K. Tanaka, “Single-cycle terahertz pulses with amplitudes exceeding 1 MV/cm generated by optical rectification in LiNbO₃,” *Applied Physics Letters*, vol. 98, no. 9, p. 091106, 2011.
- [30] A. K. Geim and K. S. Novoselov, “The rise of graphene.,” *Nature materials*, vol. 6, pp. 183–91, Mar. 2007.
- [31] A. H. Castro Neto, N. M. R. Peres, K. S. Novoselov, and A. K. Geim, “The electronic properties of graphene,” *Reviews of Modern Physics*, vol. 81, pp. 109–162, Jan. 2009.

- [32] Y. Zhang, Y.-w. Tan, H. L. Stormer, and P. Kim, “Experimental observation of the quantum Hall effect and Berry’s phase in graphene.,” *Nature*, vol. 438, pp. 201–4, Nov. 2005.
- [33] A. K. Geim, “Graphene: status and prospects.,” *Science (New York, N.Y.)*, vol. 324, pp. 1530–4, June 2009.
- [34] G. Brumfiel, “Graphene gets ready for the big time.,” *Nature*, vol. 458, pp. 390–1, Mar. 2009.
- [35] M. Dragoman and D. Dragoman, “Graphene-based quantum electronics,” *Progress in Quantum Electronics*, vol. 33, pp. 165–214, Nov. 2009.
- [36] X. Li, X. Wang, L. Zhang, S. Lee, and H. Dai, “Chemically derived, ultra-smooth graphene nanoribbon semiconductors.,” *Science (New York, N.Y.)*, vol. 319, pp. 1229–32, Feb. 2008.
- [37] L. A. Ponomarenko, F. Schedin, M. I. Katsnelson, R. Yang, E. W. Hill, K. S. Novoselov, and A. K. Geim, “Chaotic Dirac billiard in graphene quantum dots.,” *Science (New York, N.Y.)*, vol. 320, pp. 356–8, Apr. 2008.
- [38] Y.-m. Lin, K. A. Jenkins, A. Valdes-Garcia, J. P. Small, D. B. Farmer, and P. Avouris, “Operation of graphene transistors at gigahertz frequencies.,” *Nano letters*, vol. 9, pp. 422–6, Jan. 2009.
- [39] T. Wang, K. Jeppson, N. Olofsson, E. E. B. Campbell, and J. Liu, “Through silicon vias filled with planarized carbon nanotube bundles.,” *Nanotechnology*, vol. 20, p. 485203, Dec. 2009.
- [40] N. L. Rangel and J. M. Seminario, “Graphene terahertz generators for molecular circuits and sensors.,” *The journal of physical chemistry. A*, vol. 112, pp. 13699–705, Dec. 2008.
- [41] V. Ryzhii, “Terahertz Plasma Waves in Gated Graphene Heterostructures,” *Japanese Journal of Applied Physics*, vol. 45, pp. L923–L925, Sept. 2006.
- [42] C. Berger, Z. Song, X. Li, X. Wu, N. Brown, C. Naud, D. Mayou, T. Li, J. Hass, A. N. Marchenkov, E. H. Conrad, P. N. First, and W. A. de Heer, “Electronic confinement and coherence in patterned epitaxial graphene.,” *Science (New York, N.Y.)*, vol. 312, pp. 1191–6, May 2006.

- [43] K. S. Kim, Y. Zhao, H. Jang, S. Y. Lee, J. M. Kim, K. S. Kim, J.-h. Ahn, P. Kim, J.-y. Choi, and B. H. Hong, “Large-scale pattern growth of graphene films for stretchable transparent electrodes,” *Nature*, vol. 457, pp. 706–10, Feb. 2009.
- [44] X. Li, W. Cai, J. An, S. Kim, J. Nah, D. Yang, R. Piner, A. Velamakanni, I. Jung, E. Tutuc, S. K. Banerjee, L. Colombo, and R. S. Ruoff, “Large-area synthesis of high-quality and uniform graphene films on copper foils,” *Science (New York, N.Y.)*, vol. 324, pp. 1312–4, June 2009.
- [45] K. S. Novoselov, A. K. Geim, S. V. Morozov, D. Jiang, M. I. Katsnelson, I. V. Grigorieva, S. V. Dubonos, and A. A. Firsov, “Two-dimensional gas of massless Dirac fermions in graphene,” *Nature*, vol. 438, pp. 197–200, Nov. 2005.
- [46] K. Bolotin, K. Sikes, Z. Jiang, M. Klima, G. Fudenberg, J. Hone, P. Kim, and H. Stormer, “Ultrahigh electron mobility in suspended graphene,” *Solid State Communications*, vol. 146, pp. 351–355, June 2008.
- [47] S. Morozov, K. Novoselov, M. Katsnelson, F. Schedin, D. Elias, J. Jaszczak, and A. Geim, “Giant Intrinsic Carrier Mobilities in Graphene and Its Bilayer,” *Physical Review Letters*, vol. 100, p. 016602, Jan. 2008.
- [48] S. Sonde, F. Giannazzo, C. Vecchio, R. Yakimova, E. Rimini, and V. Raineri, “Role of graphene/substrate interface on the local transport properties of the two-dimensional electron gas,” *Applied Physics Letters*, vol. 97, no. 13, p. 132101, 2010.
- [49] E. Hwang, S. Adam, and S. Sarma, “Carrier Transport in Two-Dimensional Graphene Layers,” *Physical Review Letters*, vol. 98, p. 186806, May 2007.
- [50] K. Nomura and A. H. MacDonald, “Quantum Hall Ferromagnetism in Graphene,” *Physical Review Letters*, vol. 96, p. 256602, June 2006.
- [51] M. Ishigami, J. H. Chen, W. G. Cullen, M. S. Fuhrer, and E. D. Williams, “Atomic structure of graphene on SiO₂,” *Nano letters*, vol. 7, pp. 1643–8, June 2007.
- [52] F. Schedin, A. K. Geim, S. V. Morozov, E. W. Hill, P. Blake, M. I. Katsnelson, and K. S. Novoselov, “Detection of individual gas molecules adsorbed on graphene,” *Nature materials*, vol. 6, pp. 652–5, Sept. 2007.

- [53] I. Calizo, W. Bao, F. Miao, C. N. Lau, and A. A. Balandin, “The effect of substrates on the Raman spectrum of graphene: Graphene- on-sapphire and graphene-on-glass,” *Applied Physics Letters*, vol. 91, no. 20, p. 201904, 2007.
- [54] S. Y. Zhou, G.-H. Gweon, A. V. Fedorov, P. N. First, W. A. de Heer, D.-H. Lee, F. Guinea, A. H. Castro Neto, and A. Lanzara, “Substrate-induced bandgap opening in epitaxial graphene.,” *Nature materials*, vol. 6, pp. 770–5, Oct. 2007.
- [55] F. Varchon, R. Feng, J. Hass, X. Li, B. Nguyen, C. Naud, P. Mallet, J.-Y. Veuillen, C. Berger, E. Conrad, and L. Magaud, “Electronic Structure of Epitaxial Graphene Layers on SiC: Effect of the Substrate,” *Physical Review Letters*, vol. 99, p. 126805, Sept. 2007.
- [56] G. Giovannetti, P. Khomyakov, G. Brocks, P. Kelly, and J. van den Brink, “Substrate-induced band gap in graphene on hexagonal boron nitride: Ab initio density functional calculations,” *Physical Review B*, vol. 76, p. 073103, Aug. 2007.
- [57] R. Balog, B. Jø rgensen, L. Nilsson, M. Andersen, E. Rienks, M. Bianchi, M. Fanetti, E. Laegsgaard, A. Baraldi, S. Lizzit, Z. Sljivancanin, F. Besenbacher, B. r. Hammer, T. G. Pedersen, P. Hofmann, and L. Hornekaer, “Bandgap opening in graphene induced by patterned hydrogen adsorption.,” *Nature materials*, vol. 9, pp. 315–9, Apr. 2010.
- [58] Y. Xu, K. T. He, S. W. Schmucker, Z. Guo, J. C. Koepke, J. D. Wood, J. W. Lyding, and N. R. Aluru, “Inducing electronic changes in graphene through silicon (100) substrate modification.,” *Nano letters*, vol. 11, pp. 2735–42, July 2011.
- [59] J.-H. Chen, C. Jang, S. Xiao, M. Ishigami, and M. S. Fuhrer, “Intrinsic and extrinsic performance limits of graphene devices on SiO₂.,” *Nature nanotechnology*, vol. 3, pp. 206–9, Apr. 2008.
- [60] S. Fratini and F. Guinea, “Substrate-limited electron dynamics in graphene,” *Physical Review B*, vol. 77, p. 195415, May 2008.
- [61] A. I. Volokitin and B. N. J. Persson, “Quantum Friction,” *Physical Review Letters*, vol. 106, p. 094502, Mar. 2011.

- [62] J. L. Tomaino, A. D. Jameson, J. W. Kevek, M. J. Paul, A. M. van der Zande, R. A. Barton, P. L. McEuen, E. D. Minot, and Y.-S. Lee, "Terahertz imaging and spectroscopy of large-area single-layer graphene.," *Optics express*, vol. 19, pp. 141–6, Jan. 2011.
- [63] X. Li, C. W. Magnuson, A. Venugopal, R. M. Tromp, J. B. Hannon, E. M. Vogel, L. Colombo, and R. S. Ruoff, "Large-area graphene single crystals grown by low-pressure chemical vapor deposition of methane on copper.," *Journal of the American Chemical Society*, vol. 133, pp. 2816–9, Mar. 2011.
- [64] A. Nahata, A. S. Weling, and T. F. Heinz, "A wideband coherent terahertz spectroscopy system using optical rectification and electro-optic sampling," *Applied Physics Letters*, vol. 69, no. 16, p. 2321, 1996.
- [65] M. J. Paul, J. L. Tomaino, J. W. Kevek, T. DeBorde, Z. J. Thompson, E. D. Minot, and Y.-S. Lee, "Terahertz imaging of inhomogeneous electrostatics in single-layer graphene embedded in dielectrics," *Applied Physics Letters*, vol. 101, no. 9, p. 091109, 2012.
- [66] K. S. Novoselov, A. K. Geim, S. V. Morozov, D. Jiang, Y. Zhang, S. V. Dubonos, I. V. Grigorieva, and A. A. Firsov, "Electric field effect in atomically thin carbon films.," *Science (New York, N.Y.)*, vol. 306, pp. 666–9, Oct. 2004.
- [67] Y.-M. Lin, C. Dimitrakopoulos, K. A. Jenkins, D. B. Farmer, H.-Y. Chiu, A. Grill, and P. Avouris, "100-GHz transistors from wafer-scale epitaxial graphene.," *Science (New York, N.Y.)*, vol. 327, p. 662, Feb. 2010.
- [68] F. Xia, T. Mueller, Y.-m. Lin, A. Valdes-Garcia, and P. Avouris, "Ultrafast graphene photodetector.," *Nature nanotechnology*, vol. 4, pp. 839–43, Dec. 2009.
- [69] L. Vicarelli, M. S. Vitiello, D. Coquillat, A. Lombardo, A. C. Ferrari, W. Knap, M. Polini, V. Pellegrini, and A. Tredicucci, "Graphene field-effect transistors as room-temperature terahertz detectors.," *Nature materials*, vol. 11, pp. 865–71, Oct. 2012.
- [70] J. Zheng, L. Wang, R. Quhe, Q. Liu, H. Li, D. Yu, W.-n. Mei, J. Shi, Z. Gao, and J. Lu, "Sub-10 nm gate length graphene transistors: operating at terahertz frequencies with current saturation.," *Scientific reports*, vol. 3, p. 1314, Jan. 2013.

- [71] H. Y. Hwang, N. C. Brandt, H. Farhat, A. L. Hsu, J. Kong, and K. a. Nelson, “Nonlinear THz Conductivity Dynamics in CVD-Grown Graphene,” *arXiv/1101.4985*, Jan. 2011.
- [72] L. Ju, B. Geng, J. Horng, C. Girit, M. Martin, Z. Hao, H. A. Bechtel, X. Liang, A. Zettl, Y. R. Shen, and F. Wang, “Graphene plasmonics for tunable terahertz metamaterials.,” *Nature nanotechnology*, vol. 6, pp. 630–4, Oct. 2011.
- [73] R. R. Nair, P. Blake, A. N. Grigorenko, K. S. Novoselov, T. J. Booth, T. Stauber, N. M. R. Peres, and A. K. Geim, “Fine structure constant defines visual transparency of graphene.,” *Science (New York, N.Y.)*, vol. 320, p. 1308, June 2008.
- [74] Z. Q. Li, E. A. Henriksen, Z. Jiang, Z. Hao, M. C. Martin, P. Kim, H. L. Stormer, and D. N. Basov, “Dirac charge dynamics in graphene by infrared spectroscopy,” *Nature Physics*, vol. 4, pp. 532–535, June 2008.
- [75] J. Horng, C.-f. Chen, B. Geng, C. Girit, Y. Zhang, Z. Hao, H. A. Bechtel, M. Martin, A. Zettl, M. F. Crommie, Y. R. Shen, and F. Wang, “Drude conductivity of Dirac fermions in graphene,” *Physical Review B*, vol. 83, p. 165113, Apr. 2011.
- [76] H. Choi, F. Borondics, D. A. Siegel, S. Y. Zhou, M. C. Martin, A. Lanzara, and R. A. Kaindl, “Broadband electromagnetic response and ultrafast dynamics of few-layer epitaxial graphene,” *Applied Physics Letters*, vol. 94, no. 17, p. 172102, 2009.
- [77] W. S. Bao, S. Y. Liu, X. L. Lei, and C. M. Wang, “Nonlinear dc transport in graphene.,” *Journal of physics. Condensed matter : an Institute of Physics journal*, vol. 21, p. 305302, July 2009.
- [78] B. Dóra and R. Moessner, “Nonlinear electric transport in graphene: Quantum quench dynamics and the Schwinger mechanism,” *Physical Review B*, vol. 81, p. 165431, Apr. 2010.
- [79] E. G. Mishchenko, “Dynamic Conductivity in Graphene beyond Linear Response,” *Physical Review Letters*, vol. 103, p. 246802, Dec. 2009.

- [80] R. S. Shishir, D. K. Ferry, and S. M. Goodnick, “Room temperature velocity saturation in intrinsic graphene,” *Journal of Physics: Conference Series*, vol. 193, p. 012118, Nov. 2009.
- [81] S. A. Mikhailov and K. Ziegler, “Nonlinear electromagnetic response of graphene: frequency multiplication and the self-consistent-field effects.,” *Journal of physics. Condensed matter : an Institute of Physics journal*, vol. 20, p. 384204, Sept. 2008.
- [82] A. R. Wright, X. G. Xu, J. C. Cao, and C. Zhang, “Strong nonlinear optical response of graphene in the terahertz regime,” *Applied Physics Letters*, vol. 95, no. 7, p. 072101, 2009.
- [83] K. L. Ishikawa, “Nonlinear optical response of graphene in time domain,” *Physical Review B*, vol. 82, p. 201402, Nov. 2010.
- [84] S. Shareef, Y. S. Ang, and C. Zhang, “Room-temperature strong terahertz photon mixing in graphene,” *Journal of the Optical Society of America B*, vol. 29, p. 274, Feb. 2012.
- [85] A. Bostwick, F. Speck, T. Seyller, K. Horn, M. Polini, R. Asgari, A. H. MacDonald, and E. Rotenberg, “Observation of plasmarons in quasi-freestanding doped graphene.,” *Science (New York, N.Y.)*, vol. 328, pp. 999–1002, May 2010.
- [86] J. Chae, S. Jung, A. F. Young, C. R. Dean, L. Wang, Y. Gao, K. Watanabe, T. Taniguchi, J. Hone, K. L. Shepard, P. Kim, N. B. Zhitenev, and J. A. Stroscio, “Renormalization of the Graphene Dispersion Velocity Determined from Scanning Tunneling Spectroscopy,” *Physical Review Letters*, vol. 109, p. 116802, Sept. 2012.
- [87] S. Tani, F. Blanchard, and K. Tanaka, “Ultrafast Carrier Dynamics in Graphene under a High Electric Field,” *Physical Review Letters*, vol. 109, p. 166603, Oct. 2012.
- [88] S. Winnerl, M. Orlita, P. Plochocka, P. Kossacki, M. Potemski, T. Winzer, E. Malic, A. Knorr, M. Sprinkle, C. Berger, W. A. de Heer, H. Schneider, and M. Helm, “Carrier Relaxation in Epitaxial Graphene Photoexcited Near the Dirac Point,” *Physical Review Letters*, vol. 107, p. 237401, Nov. 2011.

- [89] M. Dragoman, D. Neculoiu, G. Deligeorgis, G. Konstantinidis, D. Dragoman, A. Cismaru, A. A. Muller, and R. Plana, "Millimeter-wave generation via frequency multiplication in graphene," *Applied Physics Letters*, vol. 97, no. 9, p. 093101, 2010.
- [90] M. J. Paul, Y. C. Chang, Z. J. Thompson, A. Stickel, J. Wardini, H. Choi, E. D. Minot, T. B. Norris, and Y.-S. Lee, "High-field terahertz response of graphene," *New Journal of Physics*, vol. 15, p. 085019, Aug. 2013.
- [91] M. J. Paul, B. H. Lee, J. L. Wardini, Z. J. Thompson, A. Stickel, M. A. H. Choi, E. D. Minot, and Y.-S. Lee, "Terahertz Induced Transparency in Single-Layer Graphene," *submitted to Applied Physics Letters*, 2014.
- [92] H. Y. Hwang, N. C. Brandt, H. Farhat, A. L. Hsu, J. Kong, and K. A. Nelson, "Nonlinear THz conductivity dynamics in P-type CVD-grown graphene.," *The journal of physical chemistry. B*, vol. 117, pp. 15819–24, Dec. 2013.
- [93] J. Hebling, M. C. Hoffmann, H. Y. Hwang, K.-L. Yeh, and K. a. Nelson, "Observation of nonequilibrium carrier distribution in Ge, Si, and GaAs by terahertz pumapterahertz probe measurements," *Physical Review B*, vol. 81, p. 035201, Jan. 2010.
- [94] D. Turchinovich, J. r. M. Hvam, and M. C. Hoffmann, "Self-phase modulation of a single-cycle terahertz pulse by nonlinear free-carrier response in a semiconductor," *Physical Review B*, vol. 85, p. 201304, May 2012.
- [95] A. C. Ferrari, J. C. Meyer, V. Scardaci, C. Casiraghi, M. Lazzeri, F. Mauri, S. Piscanec, D. Jiang, K. S. Novoselov, S. Roth, and A. K. Geim, "Raman Spectrum of Graphene and Graphene Layers," *Physical Review Letters*, vol. 97, p. 187401, Oct. 2006.
- [96] S. Pisana, M. Lazzeri, C. Casiraghi, K. S. Novoselov, A. K. Geim, A. C. Ferrari, and F. Mauri, "Breakdown of the adiabatic Born-Oppenheimer approximation in graphene.," *Nature materials*, vol. 6, pp. 198–201, Mar. 2007.
- [97] Y.-G. Jeong, M. J. Paul, S.-H. Kim, K.-J. Yee, D.-S. Kim, and Y.-S. Lee, "Large enhancement of nonlinear terahertz absorption in intrinsic GaAs by plasmonic nano antennas," *Applied Physics Letters*, vol. 103, no. 17, p. 171109, 2013.

- [98] A. Star, Y. Lu, K. Bradley, and G. Grüner, “Nanotube Optoelectronic Memory Devices,” *Nano Letters*, vol. 4, pp. 1587–1591, Sept. 2004.
- [99] J. Chen, V. Perebeinos, M. Freitag, J. Tsang, Q. Fu, J. Liu, and P. Avouris, “Bright infrared emission from electrically induced excitons in carbon nanotubes,” *Science (New York, N.Y.)*, vol. 310, pp. 1171–4, Nov. 2005.
- [100] M. E. Itkis, F. Borondics, A. Yu, and R. C. Haddon, “Bolometric infrared photoresponse of suspended single-walled carbon nanotube films,” *Science (New York, N.Y.)*, vol. 312, pp. 413–6, Apr. 2006.
- [101] T. Fuse, Y. Kawano, T. Yamaguchi, Y. Aoyagi, and K. Ishibashi, “Quantum response of carbon nanotube quantum dots to terahertz wave irradiation,” *Nanotechnology*, vol. 18, p. 044001, Jan. 2007.
- [102] S. Watanabe, N. Minami, and R. Shimano, “Intense terahertz pulse induced exciton generation in carbon nanotubes,” *Optics express*, vol. 19, pp. 1528–38, Jan. 2011.
- [103] Z. Zhong, N. M. Gabor, J. E. Sharping, A. L. Gaeta, and P. L. McEuen, “Terahertz time-domain measurement of ballistic electron resonance in a single-walled carbon nanotube,” *Nature nanotechnology*, vol. 3, pp. 201–5, Apr. 2008.
- [104] D. Kienle and F. Léonard, “Terahertz Response of Carbon Nanotube Transistors,” *Physical Review Letters*, vol. 103, p. 026601, July 2009.
- [105] T.-I. Jeon, J. Zhang, and D. Grischkowsky, “THz Sommerfeld wave propagation on a single metal wire,” *Applied Physics Letters*, vol. 86, no. 16, p. 161904, 2005.
- [106] I. Maeng, C. Kang, S. J. Oh, J.-H. Son, K. H. An, and Y. H. Lee, “Terahertz electrical and optical characteristics of double-walled carbon nanotubes and their comparison with single-walled carbon nanotubes,” *Applied Physics Letters*, vol. 90, no. 5, p. 051914, 2007.
- [107] M. a. Seo, J. H. Yim, Y. H. Ahn, F. Rotermund, D. S. Kim, S. Lee, and H. Lim, “Terahertz electromagnetic interference shielding using single-walled carbon nanotube flexible films,” *Applied Physics Letters*, vol. 93, no. 23, p. 231905, 2008.

- [108] T.-I. Jeon, K.-J. Kim, C. Kang, S.-J. Oh, J.-H. Son, K. H. An, D. J. Bae, and Y. H. Lee, "Terahertz conductivity of anisotropic single walled carbon nanotube films," *Applied Physics Letters*, vol. 80, no. 18, p. 3403, 2002.
- [109] T.-I. Jeon, "Optical and electrical properties of preferentially anisotropic single-walled carbon-nanotube films in terahertz region," *Journal of Applied Physics*, vol. 95, no. 10, p. 5736, 2004.
- [110] L. Ren, C. L. Pint, L. G. Booshehri, W. D. Rice, X. Wang, D. J. Hilton, K. Takeya, I. Kawayama, M. Tonouchi, R. H. Hauge, and J. Kono, "Carbon nanotube terahertz polarizer.," *Nano letters*, vol. 9, pp. 2610–3, July 2009.
- [111] J. Kyoung, E. Y. Jang, M. D. Lima, H.-R. Park, R. O. Robles, X. Lepró, Y. H. Kim, R. H. Baughman, and D.-S. Kim, "A reel-wound carbon nanotube polarizer for terahertz frequencies.," *Nano letters*, vol. 11, pp. 4227–31, Oct. 2011.
- [112] L. Ren, C. L. Pint, T. Arikawa, K. Takeya, I. Kawayama, M. Tonouchi, R. H. Hauge, and J. Kono, "Broadband terahertz polarizers with ideal performance based on aligned carbon nanotube stacks.," *Nano letters*, vol. 12, pp. 787–90, Feb. 2012.
- [113] Z.-P. Yang, L. Ci, J. a. Bur, S.-Y. Lin, and P. M. Ajayan, "Experimental observation of an extremely dark material made by a low-density nanotube array.," *Nano letters*, vol. 8, pp. 446–51, Feb. 2008.
- [114] K. Mizuno, J. Ishii, H. Kishida, Y. Hayamizu, S. Yasuda, D. N. Futaba, M. Yumura, and K. Hata, "A black body absorber from vertically aligned single-walled carbon nanotubes.," *Proceedings of the National Academy of Sciences of the United States of America*, vol. 106, pp. 6044–7, Apr. 2009.
- [115] S. Sanvito, Y.-K. Kwon, D. Tománek, and C. Lambert, "Fractional Quantum Conductance in Carbon Nanotubes," *Physical Review Letters*, vol. 84, pp. 1974–1977, Feb. 2000.
- [116] S. Roche, F. Triozon, A. Rubio, and D. Mayou, "Conduction mechanisms and magnetotransport in multiwalled carbon nanotubes," *Physical Review B*, vol. 64, p. 121401, Sept. 2001.
- [117] Y.-G. Yoon, P. Delaney, and S. Louie, "Quantum conductance of multiwall carbon nanotubes," *Physical Review B*, vol. 66, p. 073407, Aug. 2002.

- [118] A. Hansson and S. Stafström, “Intershell conductance in multiwall carbon nanotubes,” *Physical Review B*, vol. 67, p. 075406, Feb. 2003.
- [119] K.-H. Ahn, Y.-H. Kim, J. Wiersig, and K. Chang, “Spectral Correlation in Incommensurate Multiwalled Carbon Nanotubes,” *Physical Review Letters*, vol. 90, p. 026601, Jan. 2003.
- [120] V. Zólyomi, J. Koltai, A. Rusznyák, J. Kúrti, A. Gali, F. Simon, H. Kuzmany, A. Szabados, and P. Surján, “Intershell interaction in double walled carbon nanotubes: Charge transfer and orbital mixing,” *Physical Review B*, vol. 77, p. 245403, June 2008.
- [121] B. Bourlon, C. Miko, L. Forró, D. Glatli, and A. Bachtold, “Determination of the Intershell Conductance in Multiwalled Carbon Nanotubes,” *Physical Review Letters*, vol. 93, p. 176806, Oct. 2004.
- [122] Y. Saito, T. Yoshikawa, S. Bandow, M. Tomita, and T. Hayashi, “Interlayer spacings in carbon nanotubes,” *Physical Review B*, vol. 48, pp. 1907–1909, July 1993.
- [123] A. D. Jameson, J. W. Kevek, J. L. Tomaino, M. Hemphill-Johnston, M. J. Paul, M. Koretsky, E. D. Minot, and Y.-S. Lee, “Terahertz spectroscopy of NiTi alloy thin films,” *Applied Physics Letters*, vol. 98, no. 22, p. 221111, 2011.
- [124] P. Yeh, A. Yariv, and C.-S. Hong, “Electromagnetic propagation in periodic stratified media I General theory,” *Journal of the Optical Society of America*, vol. 67, p. 423, Apr. 1977.
- [125] J. A. Nelder and R. Mead, “A Simplex Method for Function Minimization,” *The Computer Journal*, vol. 7, pp. 308–313, Jan. 1965.
- [126] D. M. Olsson and L. S. Nelson, “The Nelder-Mead Simplex Procedure for Function Minimization,” *Technometrics*, vol. 17, pp. 45–51, Feb. 1975.
- [127] C. T. Kelley, *Iterative Methods for Optimization*. Springer, 1999.
- [128] A. Javey and J. Kong, *Carbon Nanotube Electronics*. Springer, 2009.
- [129] R. L. Powell and G. E. Childs, *American Institute of Physics Handbook, 3rd Edition*. McGraw-Hill, 1972.

- [130] M. J. Paul, N. a. Kuhta, J. L. Tomaino, a. D. Jameson, L. P. Maizy, T. Sharf, N. L. Rupesinghe, K. B. K. Teo, S. Inampudi, V. a. Podolskiy, E. D. Minot, and Y.-S. Lee, "Terahertz transmission ellipsometry of vertically aligned multi-walled carbon nanotubes," *Applied Physics Letters*, vol. 101, p. 111107, Sept. 2012.
- [131] R. Ulbricht, E. Hendry, J. Shan, T. F. Heinz, and M. Bonn, "Carrier dynamics in semiconductors studied with time-resolved terahertz spectroscopy," *Reviews of Modern Physics*, vol. 83, pp. 543–586, June 2011.
- [132] K. Kawase, M. Sato, T. Taniuchi, and H. Ito, "Coherent tunable THz-wave generation from LiNbO₃ with monolithic grating coupler," *Applied Physics Letters*, vol. 68, no. 18, p. 2483, 1996.
- [133] J. Hebling, K.-l. Yeh, M. C. Hoffmann, and K. A. Nelson, "High-Power THz Generation, THz Nonlinear Optics, and THz Nonlinear Spectroscopy," *IEEE Journal of Selected Topics in Quantum Electronics*, vol. 14, no. 2, pp. 345–353, 2008.
- [134] I.-C. Ho and X.-C. Zhang, "Driving intervalley scattering and impact ionization in InAs with intense terahertz pulses," *Applied Physics Letters*, vol. 98, no. 24, p. 241908, 2011.
- [135] M. Hoffmann, J. Hebling, H. Hwang, K.-L. Yeh, and K. Nelson, "Impact ionization in InSb probed by terahertz pumapterahertz probe spectroscopy," *Physical Review B*, vol. 79, p. 161201, Apr. 2009.
- [136] H. Hirori, K. Shinokita, M. Shirai, S. Tani, Y. Kadoya, and K. Tanaka, "Extraordinary carrier multiplication gated by a picosecond electric field pulse.," *Nature communications*, vol. 2, p. 594, Jan. 2011.
- [137] P. Gaal, K. Reimann, M. Woerner, T. Elsaesser, R. Hey, and K. Ploog, "Nonlinear Terahertz Response of n-Type GaAs," *Physical Review Letters*, vol. 96, p. 187402, May 2006.
- [138] F. H. Su, F. Blanchard, G. Sharma, L. Razzari, A. Ayeshehim, T. L. Cocker, L. V. Titova, T. Ozaki, J.-C. Kieffer, R. Morandotti, M. Reid, and F. a. Hegmann, "Terahertz pulse induced intervalley scattering in photoexcited GaAs," *Optics Express*, vol. 17, p. 9620, May 2009.

- [139] G. Sharma, I. Al-Naib, H. Hafez, R. Morandotti, D. G. Cooke, and T. Ozaki, “Carrier density dependence of the nonlinear absorption of intense THz radiation in GaAs,” *Optics express*, vol. 20, pp. 18016–24, July 2012.
- [140] Y. Shi, Q.-l. Zhou, C. Zhang, and B. Jin, “Ultrafast high-field carrier transport in GaAs measured by femtosecond pump-terahertz probe spectroscopy,” *Applied Physics Letters*, vol. 93, no. 12, p. 121115, 2008.
- [141] W. Kuehn, P. Gaal, K. Reimann, M. Woerner, T. Elsaesser, and R. Hey, “Coherent Ballistic Motion of Electrons in a Periodic Potential,” *Physical Review Letters*, vol. 104, p. 146602, Apr. 2010.
- [142] P. Bowlan, W. Kuehn, K. Reimann, M. Woerner, T. Elsaesser, R. Hey, and C. Flytzanis, “High-Field Transport in an Electron-Hole Plasma: Transition from Ballistic to Drift Motion,” *Physical Review Letters*, vol. 107, p. 256602, Dec. 2011.
- [143] F. Blanchard, D. Golde, F. H. Su, L. Razzari, G. Sharma, R. Morandotti, T. Ozaki, M. Reid, M. Kira, S. W. Koch, and F. a. Hegmann, “Effective Mass Anisotropy of Hot Electrons in Nonparabolic Conduction Bands of n-Doped InGaAs Films Using Ultrafast Terahertz Pump-Probe Techniques,” *Physical Review Letters*, vol. 107, p. 107401, Aug. 2011.
- [144] K. Fan, H. Y. Hwang, M. Liu, A. C. Strikwerda, A. Sternbach, J. Zhang, X. Zhao, X. Zhang, K. a. Nelson, and R. D. Averitt, “Nonlinear Terahertz Metamaterials via Field-Enhanced Carrier Dynamics in GaAs,” *Physical Review Letters*, vol. 110, p. 217404, May 2013.
- [145] H.-T. Chen, W. J. Padilla, J. M. O. Zide, A. C. Gossard, A. J. Taylor, and R. D. Averitt, “Active terahertz metamaterial devices.,” *Nature*, vol. 444, pp. 597–600, Nov. 2006.
- [146] H.-T. Chen, W. J. Padilla, M. J. Cich, A. K. Azad, R. D. Averitt, and A. J. Taylor, “A metamaterial solid-state terahertz phase modulator,” *Nature Photonics*, vol. 3, pp. 148–151, Feb. 2009.
- [147] A. Degiron, J. J. Mock, and D. R. Smith, “Modulating and tuning the response of metamaterials at the unit cell level,” *Optics Express*, vol. 15, no. 3, p. 1115, 2007.

- [148] M. a. Seo, H. R. Park, S. M. Koo, D. J. Park, J. H. Kang, O. K. Suwal, S. S. Choi, P. C. M. Planken, G. S. Park, N. K. Park, Q. H. Park, and D. S. Kim, “Terahertz field enhancement by a metallic nano slit operating beyond the skin-depth limit,” *Nature Photonics*, vol. 3, pp. 152–156, Feb. 2009.
- [149] H. R. Park, Y. M. Park, H. S. Kim, J. S. Kyoung, M. a. Seo, D. J. Park, Y. H. Ahn, K. J. Ahn, and D. S. Kim, “Terahertz nanoresonators: Giant field enhancement and ultrabroadband performance,” *Applied Physics Letters*, vol. 96, no. 12, p. 121106, 2010.
- [150] M. Shalaby, H. Merbold, M. Peccianti, L. Razzari, G. Sharma, T. Ozaki, R. Morandotti, T. Feurer, A. Weber, L. Heyderman, B. Patterson, and H. Sigg, “Concurrent field enhancement and high transmission of THz radiation in nanoslit arrays,” *Applied Physics Letters*, vol. 99, no. 4, p. 041110, 2011.
- [151] H.-R. Park, K. J. Ahn, S. Han, Y.-M. Bahk, N. Park, and D.-S. Kim, “Colossal absorption of molecules inside single terahertz nanoantennas,” *Nano letters*, vol. 13, pp. 1782–6, Apr. 2013.
- [152] J. Kyoung, M. Seo, H. Park, S. Koo, H.-s. Kim, Y. Park, B.-J. Kim, K. Ahn, N. Park, H.-T. Kim, and D.-S. Kim, “Giant nonlinear response of terahertz nanoresonators on VO₂ thin film,” *Optics express*, vol. 18, pp. 16452–9, Aug. 2010.
- [153] Y. M. Bahk, H. R. Park, K. J. Ahn, H. S. Kim, Y. H. Ahn, D.-S. Kim, J. Bravo-Abad, L. Martin-Moreno, and F. J. Garcia-Vidal, “Anomalous Band Formation in Arrays of Terahertz Nanoresonators,” *Physical Review Letters*, vol. 106, p. 013902, Jan. 2011.
- [154] H. Shichijo and K. Hess, “Band-structure-dependent transport and impact ionization in GaAs,” *Physical Review B*, vol. 23, pp. 4197–4207, Apr. 1981.
- [155] M. Fischetti and S. Laux, “Monte carlo analysis of electron transport in small semiconductor devices including band-structure and space-charge effects,” *Physical Review B*, vol. 38, pp. 9721–9745, Nov. 1988.
- [156] A. Di Carlo, P. Vogl, and W. Pötz, “Theory of Zener tunneling and Wannier-Stark states in semiconductors,” *Physical Review B*, vol. 50, pp. 8358–8377, Sept. 1994.

